Advanced simulation and modeling of turbulent sprays

A DISSERTATION
SUBMITTED TO THE FACULTY OF THE GRADUATE SCHOOL
OF THE UNIVERSITY OF MINNESOTA
BY

Wanjiao Liu

IN PARTIAL FULFILLMENT OF THE REQUIREMENTS
FOR THE DEGREE OF
Doctor of Philosophy

Sean C. Garrick

March, 2014

Acknowledgements

I would like to thank my PhD advisor, Professor Sean Garrick for his help and guidance during my times in graduate school. I appreciate all the time and ideas he provided and the insightful discussions we had in research. This thesis will not be possible without his guidance. I would also like to thank for his effort and support during my job hunting.

I would like to thank my labmates Jun and Andrew. They have explain lots of technical details of the code to me when I first started working in the lab, helping me to learn the new things much faster. It would be much more difficult for me without their help and friendship. I would also like to thank the help from my labmates Nate, Grant, Everett, Sicong and Liz for their help and insightful discussions with me during research.

I would like to thank my PhD committee members: Professor Ellen Longmire, Professor Paul Strykowski, Professor Terry Simon. I appreciate all the time and effort they put in providing their valuable opinions.

This thesis was funded by The Dow Chemical Company, and I would like to thank their generous support for my research. I would like to thank Mike Cloeter, Santhosh Ramalingam, Christopher Jian from Fluid Mechanics & Mixing group in Dow Chemical for their support and countless useful discussions with me. They have provided a valuable internship experience for me in Dow Chemical which is greatly beneficial for my PhD research.

Most importantly, I would like to thank my family for their support and unconditional love. I would not have completed my graduate school if not for my parents, Zongli Liu and Rong Zhao. My husband Cao Zhang has been extremely supportive for my decisions in life and career, and always encourages me when I feel frustrated.

Last but not least, I would like to thank my friends Lin Lin, Yali Li, Dan Wu,

Bo Peng, Junfeng Zhu, Hui Wang, Xiaoqing He, Tian Wei for their companions and friendship during graduate school.

Dedication

To my parents Zongli Liu and Rong Zhao, who always support me for pursuing my dreams

Abstract

Sprays have wide applications in agriculture, pharmaceutical synthesis, engines, ink jet printing and so on. The successful spray applications and the control of spray parameters require a thorough understanding towards the physical mechanisms. Numerical tools have been developed in the past few years for simulating the multiphase turbulent flows like sprays. Several researchers have successfully carried out direct numerical simulations (DNS) to investigate the primary breakup in such flows. DNS is accurate but requires extensive computational resources. In comparison, large eddy simulation (LES) is more practical, resolving only the large-scale flow structures and modeling the small-scale effects. The major difficulty with LES of multiphase turbulent flows is the need to model the interfacial subgrid-scale terms. Subgrid surface tension force, for example, plays an important role in the small droplet formation process. Subgrid surface tension force is, however, a highly non-linear term and can be difficult to model. In this research, we propose a new approach that combines the filtered density function (FDF) approach with the large eddy simulation. The major advantage of FDF is that the non-linear surface tension force appears in a closed form and thus needs no subgrid modeling. The FDF transport equation is solved conveniently via a Lagrangian Monte-Carlo method. The Lagrangian approach is attractive in that it facilitates the transport of the liquid-gas interface without the diffusive or dispersive errors found in the Eulerian approaches. The surface tension source term in the momentum equation is closed using a Lagrangian volume of fluid (LVOF) approach. We utilize concepts from the smoothed particle hydrodynamics (SPH) in the LVOF approach to obtain the surface tension source term based on the Lagrangian particles. Several modifications have been made towards the original SPH formulation such that it is more suitable for the large-scale, turbulent multiphase flow simulations. Multiple particles are seeded in each Eulerian cell to achieve higher statistical accuracy, while the original SPH seeds one particle in each cell. What's more, a weighted SPH formula for the color function is adopted and is shown to be capable of handling variable particle number density. Performance assessment is via the rotation of Zalesak's disk and an oscillating elliptical droplet. Results show that the modified approach is able to handle the variable particle

number density case appropriately. The simulations of multiphase turbulent flows are then performed with the proposed FDF-VOF methodology. At the same time, results from the simulations are compared with the DNS approach for validation and comparison. Results show that the FDF-LES based approach can be a promising method, in that it models the flow with lower computational cost than DNS, yet maintaining accuracy in a model-free manor.

Contents

List of Tables

List of Figures

Chapter 1

Introduction

A spray is a collection of small, dispersed liquid droplets surrounded by gas, normally formed from atomization–the process where bulk liquid column disintegrate into fine droplets[1]. Sprays have broad applications in agriculture, pharmaceutical synthesis, engines, ink jet printing and so on[2, 3, 4, 5, 6, 7, 8, 9]. In the applications of sprays, people always seek for optimal flow and fluid parameters, such that certain characteristics of spray such as droplet size distribution and spray angle, can be controlled. For example, it is desirable in agriculture spraying that droplets with diameters less than 100 micron can be reduced in number, such that little or no spray drifting will occur[7, 10]. The successful spray application and control of spray parameters require a thorough understanding towards physical mechanism of sprays and atomization. Liquid jet breakup has been investigated for a long time, since Rayleigh first published a paper on capillary breakup of a round jet in 1879[11] . Round jet breakup is frequently studied due to its relative simplicity compared to an asymmetrically shaped nozzle. People have divided the liquid jet breakup process into four regimes, which are: Rayleigh regime, first wind induced regime, second wind induced regime and atomization regime[12, 1, 13]. In the Rayleigh regime and the first wind induced regime, flow is laminar and usually axially symmetric, forming droplets with diameters on the order of the nozzle outlet size. In the second wind induced regime and atomization regime, droplets formed have much smaller diameters than the nozzle outlet size. Linear stability theory works well for the Rayleigh regime and the first wind induced regime, being able to predict very well the breakup length–the length of coherent core in the liquid jet, agreeing with observations

from experiment[13]. The second wind induced regime and atomization regime, however, have few theoretical analyse due to their highly nonlinear behavior. The second wind induced regime and atomization regime are extremely sensitive to small disturbances and inflow conditions. Experimental techniques have difficulties in detecting such dense, 3D, highly turbulent region in spray under high velocity, high pressure conditions[14]. These make the atomization hardly predictable by theory. Thus, the atomization has always been investigated by developing correlations between the operation condition and some characteristics of spray, such as mean droplet diameter and spray angle[1]. Weber numbers, Reynolds number and Ohnesorge number have been successfully used by researchers to determine the onset of four regimes in round jet through empirical models[12, 13].

An alternative and promising way is to simulate spray and atomization numerically. Recent development of numerical methods provides ways to simulate atomization process by directly solving Navier-Stokes equations and resolving the interfacial geometries. The numerical methods for modeling interface flow are mainly divided into Lagrangian and Eulerian method[15, 14]. The method is called Lagrangian if the motion of individual fluid element is captured. The discretizing grid is often attached to fluid element, moving and deforming as fluid element does so. If instead, the change of properties in space is captured, then the method is Eulerian. Both Lagrangian and Eulerian methods have been extensively used in the past for modeling multiphase interfacial flows. Lagrangian approaches are attractive due to their accuracy in describing the spatio-temporal evolution of the liquid-gas interface. Enright *et al* proposed a methodology that combines a Lagrangian particle approach with an Eulerian level-set approach, and uses Lagrangian particles to rebuild and correct Eulerian level-set field ([16]). [17] presented a Lagrangian level-set approach, and solved the reinitialization problem by proposing a re-meshing procedure. Another Lagrangian method is front tracking method, developed by G. Tryggvason et al[18], which uses fixed grid to solve Navier-Stokes equation and moving grid to track the interface. The main advantage of this approach is that the interface remains sharp and will not suffer from numerical diffusion like many other methods, because interface is always explicitly represented by connection of moving grid points[14, 15]. The major disadvantage is also inherent within the method itself: as the interface undergoes deformation, the grid discretizing

the interface always needs to be remeshed. The remeshing procedure will be costly for flow undergoing large deformation and topological changes. Also, the merging and breaking of two interfaces cannot be dealt with automatically and need some extra numerical treatments.[18, 19] Thus, although works well for various categories of flow, it has hardly been used in modeling primary breakup and complex system of air-liquid jet.

Eulerian methods are much more popular in spray modeling than the Lagrangian methods mentioned above[14]. The representative two methods are level set (LS)[20, 21, 22, 23, 24] and volume of fluid (VOF) method[25, 15, 26, 27]. Volume of fluid (VOF) method and level set (LS) method are two popular methods that directly track the evolution of liquid-gas interface. Volume of fluid method was developed in 1980s and has recently been successfully used in simulating atomization and sprays[28, 29, 30]. A major advantage of volume of fluid method is that it is mass preserving[14]. Surface reconstruction is needed in volume of fluid method, in order to obtain information on interfacial geometry and surface tension force. However, the reconstruction steps can be complex and have limited order of accuracy[26]. What's more, the VOF methods suffer from broadening or smearing of the liquid-gas interfaces, due to the diffusive errors that occur when solving the transport equation. Another disadvantage is the appearance of artificial droplets with roughly the size of the grid spacing ([14, 31]).

Level set methods are another popular category of interface tracking techniques. It is advantageous in that it provides a convenient and accurate way of calculating surface tension force determined from interfacial curvature. In contrast to the Lagrangian way of tracking interface such as front tracking method, level set method does not solve for the explicit position of interface. The advantage of level set method is that the interfacial topological information can be easily gained from the level set function[32]. Thus, surface tension force due to curvature of interface can be directly calculated from level set. However, level set methods also suffer from accuracy associated with the lack of a conservation principle, reinitialization, and more practically lack of appropriate resolution. The disadvantage of level set method is that the interface will shrink and mass enclosed by it will be losing[32, 33]. Several methodologies have been proposed to solve this issue in the past. For example, coupled level set and volume of fluid method (CLSVOF) [32, 34] combines the mass conserving volume of fluid method with

level set method. However, the method still needs surface reconstruction and adds lots of complexity to the level set method, thus loses the advantage of the original method. Refined level set grid method[35, 36] has also obtained success in atomization modeling. However, the method uses refined grid near interface, thus only reduces the level set shrinking error, and adds more complexity in grid refining and requires more computational time. Accurate conservative level set method (ACLS) [37, 38, 39] is another modified form of level set method, which preserves the mass by using a new definition of level set function. Direct numerical simulations (DNS) have been performed by a number of researchers to successfully simulate atomization process using level set methods[34, 35, 39, 31].

Several researchers have utilized the above mentioned interface tracking techniques and been able to model the breakup of the multiphase turbulent jet[32, 34, 40, 31, 25, 15, 28, 29, 30, 41]. These works are all done through direct numerical simulation (DNS), where both the smallest scale of turbulent structure and smallest interfacial structure are resolved by the grid. Direct numerical simulation is an accurate way of modeling, but also too expensive to be utilized in application. Reynolds averaged Navier-Stokes (RANS) is not expensive, but can only give steady time averaged result. Large eddy simulation(LES) is a more promising way in terms of both saving computational cost and accuracy. Instead of resolving every scale in the flow, it uses sub-grid scale (SGS) models to provide information on the terms with scale below some cut-off size[42]. For single phase flow large eddy simulation is well developed and there are already lots of validated sub-grid models. For multiphase flow, however, there is no validated model yet.

One of the earliest attempts towards large eddy simulation of multiphase turbulent flow, is the work done by E. Labourasse[43], where phase separation occurs in a container filled with layers of oil and water. Sub-Grid terms are investigated and some different models are tried to compare with the SGS term from DNS data. They find out that the SGS surface tension force has the same order of magnitude as the traditional SGS shear stress, and that the classical eddy viscosity model failed in modeling SGS interfacial terms. Chesnel et al[44] have also performed a sub-grid analysis on the DNS data of a liquid jet, where they also show that for liquid jet the eddy viscosity model does not work well and suggested that this is because the SGS interfacial terms are not directly

related to turbulent motion. They show that mixed model including a scale similarity assumption works well comparing to the eddy viscosity model, but also point out there is no simple way to determine the constant needed in such model.

DNS resolves the smallest spatial and time scale and simulates flow in a model free manner. For atomization problem, the smallest scales need resolving are turbulent Komolgorov length, as well as the smallest interfacial scale. A primary issue is that interfacial scale can be infinitely small during pinch-off process, which is troublesome for performing DNS, and only quasi-DNS can be performed[14] . Even the quasi-DNS will require a large grid and significant amount of computational time in order to resolve smallest droplet and to capture the correct interfacial dynamics. Large eddy simulation (LES) resolves large scales and models small scale subgrid effects, and has achieved great success in single phase flows through years of development [45]. For multiphase interfacial flow, however, the situation is much more complex and involved. Some preliminary analysis towards large eddy simulation for atomization are performed in past several years[28, 29, 30, 46, 47, 44]. In some recent research[28, 29, 30, 46], LES is coupled with volume of fluid method to simulate atomization process of liquid jet. Due to the lack of model, subgrid surface tension force and subgrid scalar convection are both neglected in these research, from the reasoning that Weber number is large for their flow and the effect of these terms can be small comparing to inertia. However, as pointed out by Gorokhovski et al[14], these terms can play a significant role at the small scales, since curvature increases with decreasing length scale. Thus, at small scale, the subgrid interfacial forces can be as important as the resolved forces and should not be neglected for the correct prediction of small droplet formation. In the filtered Navier-Stokes equation for multiphase flow, subgrid surface tension force is a highly nonlinear term. Modeling this non-linear term can be difficult, especially given the fact that droplet formation during atomization is not a cascade process as the dynamics in single phase turbulence[47]. Labourasse et al[43] was one of the first authors to carry out subgrid analysis on two phase interfacial flow system. They studied the magnitude of different subgrid interfacial terms in a phase inversion flow. They showed that subgrid surface tension force plays a dominant role in their flow and has a larger magnitude than other subgrid forces. Chesnel et al[44] performed a subgrid analysis towards their DNS atomization results using CLSVOF method, and found that the Smagorinsky model

does not work well for modeling the subgrid interfacial terms, because the large gradient across interface is not related to turbulent motion. The scale similarity model works better, but an unknown constant needs to be estimated. Herrmann and Gorokhovski[47] proposed an alternative way that performs DNS to solve level set transport equation, and perform LES for the Navier-Stokes equations, such that the modeling of subgrid interfacial terms can be avoided. However, the approach can still be time-consuming due to the need to fully resolve the liquid-gas interface.

In combustion research area, people have encountered similar issues to close the highly non-linear reaction term. A number of subgrid models are tried and fail to effectively model the reaction term. An approach called probability density function (PDF) method arises due to such need[48, 49, 50, 51]. PDF method solves the evolution equation of a probability density function, and all the other statistical information, e.g. mean velocity and Reynolds stress, can all be calculated based on the PDF. The great property of PDF method is that the reaction term appears to be in closed form in the PDF transport equation and does not need any modeling[49]. Meanwhile, the PDF method is advantageous in handling variable density in the flow, which is frequently encountered in combustion process. PDF has achieved great success in combustion industry because of these properties. Originally designed for Reynolds-averaged Navier-Stokes (RANS), the PDF method is further extended to filtered density function method (FDF) in LES, where the subgrid closure is achieved by using probability density function[52, 53, 54, 55, 56]. The FDF transport equation is solved by using a Lagrangian Monte Carlo method, which brings an additional advantage of the method that the Lagrangian numerical method brings minimum diffusive error. The advantages in handling nonlinear terms, variable density flow and minimum numerical diffusion makes FDF approach a suitable and preferable way of subgrid modeling in LES of atomization and spray.

One of the most challenging problem in FDF approach for the simulation of multiphase turbulent flows, is the modeling of surface tension forces based on Lagrangian particles. The surface tension force involves second order derivatives of the transported scalar array, while traditional differential operations cannot be directly applied on to particles to calculate derivatives. Recently, a Lagrangian particle based method called the smoothed particle hydrodynamics (SPH) method, originally developed for astrophysical

problems, has been applied to various multiphase flow problems ([57, 58, 59, 60, 61]). The general concept of SPH is that the spatial domain is discretized by a number of particles representing the local fluid. Functions and derivatives are approximated by particle values within the influence radius. Fluid properties, such as density, mass, velocity, pressure, are solved for each particle in the domain. The advantage of the SPH method is that diffusive and dispersive errors associated with traditional Eulerian methods are not present. The drawback of the SPH method is that particle inconsistency error usually leads to decreased accuracy. Also, the computational cost is usually on the order of $Nlog(N)$ at best, making it more expensive than traditional Eulerian methods with similar resolution ([61]). One of the first SPH-based surface tension model utilized the continuum surface force (CSF) method, while determining the normal vector and curvature using particle values ([58]). [59] developed a hybrid SPH approach where one phase is described in Eulerian frame and the other phase is represented by Lagrangian particles. The SPH based surface tension force model is utilized to model surface tension at interfaces, and several test cases, such as oscillating droplet and Rayleigh-Taylor instability were presented. Their method requires uniform particle spacing in order to correctly calculate particle number density. However, the uniform particle density constraint is rarely satisfied in turbulent multiphase flows due to large interface deformation, flow entrainment, and the creation of new interfaces. [61] have applied corrected the SPH method on a liquid jet in laminar regime. Their approach reduces the numerical inconsistency at boundaries. However, computational cost is also increased as the corrected SPH algorithm requires solving a matrix for each particle in the two-dimensional flow, instead of the addition and multiplication operations in the original SPH method.

In this research, we will develop a combined FDF-LES method for the simulation of the multiphase turbulent flows. We will first perform the direct numerical simulations and look into the subgrid terms that are present for the multiphase flows. At the same time, we will look into the dynamics of the jet breakup and the droplet formation. Next, we will propose a particle based surface tension force model based on the smooth particle hydrodynamics. Finally, we will implement the Lagrangian FDF approach for the large eddy simulation of turbulent multiphase flows and combine it with the particle based surface tension force model to obain the closure of the system.

Chapter 2

A priori analysis of turbulent multiphase flows

Direct numerical simulation (DNS) is the most accurate approach in that it resolves every scale in the flow – including both the smallest turbulent scale and the interfacial scales. Despite the accuracy of result from DNS, it is computationally expensive which is hard to be employed in practical use. The more feasible way is large eddy simulation (LES). Large eddy simulation resolves the large scales in the flow, and use sub-grid scale (SGS) models to model the small and unresolved scales. Large eddy simulation is more accurate than RANS, and have reduced computational cost than DNS. In order to help understanding and establishing validated SGS models in LES, DNS is performed in this chapter. The droplet formation mechanisms in the turbulent multiphase flows are looked into by studying the results from DNS. After that, a priori analysis of the SGS surface tension term is carried out based on the DNS data. SGS surface tension term is a new term for multiphase interfacial flow, and does not show up in the traditional single phase flow LES governing equations. The analysis will help understanding the effect of the SGS surface tension term in the multiphase flows.

2.1 Direct numerical simulation

2.1.1 Formulations

Fluid transport

The governing equations characterizing the liquid jet issuing into the gas is composed by incompressible Navier-Stokes equations which solves velocity $u_i(\mathbf{x}, t)$ and pressure $p(\mathbf{x}, t)$. The gravitational force is neglected. The governing equations are given by

$$\frac{\partial u_i}{\partial x_i} = 0, \tag{2.1}$$

$$\frac{\partial \rho u_i}{\partial t} + \frac{\partial \rho u_i u_j}{\partial x_j} = -\frac{\partial p}{\partial x_i} + \frac{\partial \tau_{ij}}{\partial x_j} + \gamma\kappa\frac{\partial H}{\partial x_i}, \tag{2.2}$$

where p is the fluid pressure. τ_{ij} is the stress tensor. ρ is the fluid density. γ is the surface tension coefficient, equaling to the surface tension force per unit length of the interface. It is a property of the liquid and the temperature, and is a constant for the isothermal case considered here. κ is the curvature of the liquid-gas interface. H is the Heaviside function, defined as

$$H = \begin{cases} 1 & \text{if } \phi > 0 \\ 0 & \text{otherwise.} \end{cases} \tag{2.3}$$

Interface tracking

The major challenge in the simulation of multiphase turbulent flows, is the modeling of complicated interfacial dynamics including the interface deforming, interface pinching, droplets formation and droplet coalescence etc. These phenomena are dominated by the surface tension forces acting on the interfaces. It is then required that one has clear knowledge of the location and the shape of the phase interface in order to model the correct interface dynamics. The most popular two methods are level set (LS) method and volume of fluid (VOF) method. The concepts behind these two methods are different-level set method tracks the interface motion, also called a surface marker method, while volume of fluid tracks the interior and exterior bulk fluid, also called a volume marker method[15]. Figure2.1.1 shows level set and volume of fluid field for two droplets in a

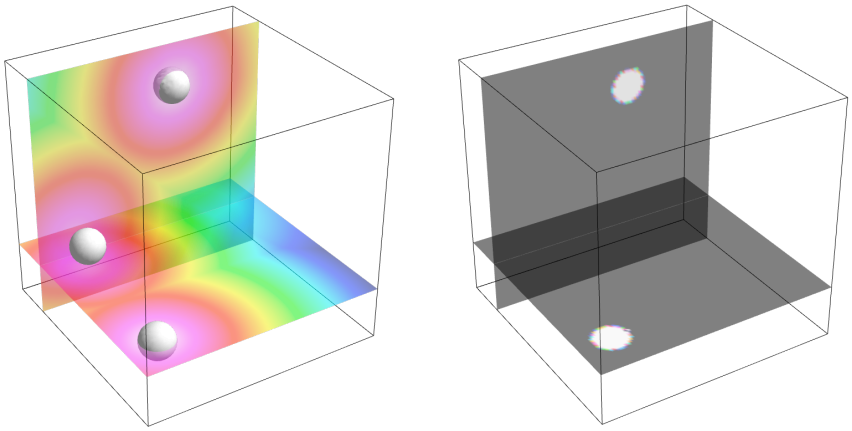

Figure 2.1: Level set and volume of fluid field for a rectangular domain with three droplets. Left: Colored contour shows the level set value at the two plane section. White surface represents the interface of droplets. Right: Color on the plane represents value of volume of fluid. White is volume of fluid of 1. Black is volume of fluid of 0.

box. Level set, ϕ, is defined as the closest signed distance to the interface. The sign of the level set is positive in the liquid ($\phi > 0$), negative in the gas ($\phi < 0$), and zero at the liquid-gas interface. The level set transport equation is given by

$$\frac{\partial \phi}{\partial t} + \frac{\partial u_j \phi}{\partial x_j} = 0. \tag{2.4}$$

The interface curvature is computed from level set via

$$\kappa = \frac{\partial^2 \phi}{\partial x_j \partial x_j} \Big/ \sqrt{\frac{\partial \phi}{\partial x_j}\frac{\partial \phi}{\partial x_j}}. \tag{2.5}$$

The volume of fluid is defined as the liquid volume percentage in a grid cell. If the cell is all liquid then $\psi = 1$. If the cell is all gas then $\psi = 0$. Values in between – $0 < F < 1$ – mean there is both liquid and gas exist in the cell. The volume of fluid transport equation is given by

$$\frac{\partial \psi}{\partial t} + \frac{\partial u_j \psi}{\partial x_j} = 0. \tag{2.6}$$

Level set is advantageous in that surface tension force can be convenient calculated from it. However, it suffers from loss of mass when its transport equation is solved, especially when the grid resolution is coarse. In contrast, volume of fluid does not have the mass conservation issue, but it induces diffusive and dispersive errors at interface because of the fact that it is a sharp step function. Thus, volume of fluid methods are not able to preserve the sharp interfaces, and cannot be used directly to calculate the surface tension forces. Combined methodologies such as coupled level set and volume of fluid (CLSVOF) can be used, but usually requires complex interface reconstruction and lost the simplicity and efficiency of the original level set. In this chapter, we use the level set to obtain the surface tension force source term. And both level set and volume of fluid are solved through transport equations.

Flow properties ρ, μ are both defined as a function of Heaviside function H through

$$\rho = \rho_g + (\rho_l - \rho_g)H, \tag{2.7}$$

$$\mu = \mu_g + (\mu_l - \mu_g)H, \tag{2.8}$$

where ρ_g and ρ_l are density of gas and liquid, respectively.

To avoid the numerical instability caused by the discontinuity of H, a smoothed form of Heaviside function is adopted, which is defined based on level set such that it can have a fixed width across the interface. It is given by

$$H_\epsilon = \begin{cases} 1 & \text{if } \phi > \epsilon \\ \frac{1}{2}[1 + \frac{\phi}{\epsilon} + \frac{1}{\pi} sin(\pi\phi/\epsilon)] & \text{if } |\phi| < \epsilon \\ 0 & \text{if } \phi < -\epsilon. \end{cases} \tag{2.9}$$

where ϵ is a small number on the order of grid spacing.

Several non–dimensional numbers are defined based on the no-ndimensionalized governing equations to provide a convenient a way of quantifying the effect of different forces. These are liquid Weber number, defined as

$$We_l = \frac{\rho_l U^2 L}{\gamma}, \tag{2.10}$$

gas Weber number, defined as

$$We_l = \frac{\rho_g U^2 L}{\gamma}, \tag{2.11}$$

Reynolds number based on liquid, defined as

$$Re_l = \frac{\rho_g U L}{\mu}, \tag{2.12}$$

and Ohnesorge number, defined as

$$Oh = \frac{\sqrt{We}}{Re}. \tag{2.13}$$

Weber number characterize the ratio between the inertial force and surface tension force and is a critical parameter for interfacial flows. Reynolds number represents the ratio of inertial force to viscous force. Ohnesorge number, defined from Weber number and Reynolds number, shows the ratio between viscous force and the product of inertial force and surface tension force. Flow with large Ohnesorge number means that the flow is viscous dominated.

Reinitialization

When the level set ϕ is solved from its transport equation, it will deviate from the definition of a level set function. This is because as an surface marker method, level set transport equation is only accurate for interface where ϕ equals to zero, but not true elsewhere. Such deviation is especially significant in an interface undergoing large deformation – which is what is always encountered in a turbulent flow – and will result in incorrect surface tension force and lead to numerical instability. Thus, level set value needs to be corrected to the value of the signed distance to the interfaces. This correction step is called reinitialization. Figure2.1.1 shows the equally spaced level set contour without and with reinitialization, and the spurious oscillation occurring in the non-reinitialized case is apparent. In reinitialized case, level set contours remain equally spaced and smooth .

There are several techniques of reinitialization, mainly divided into two categories. First category is rather straightforward by simply looping over all the grid points and find the distance to the nearest interface. The advantage of this method is its accuracy,

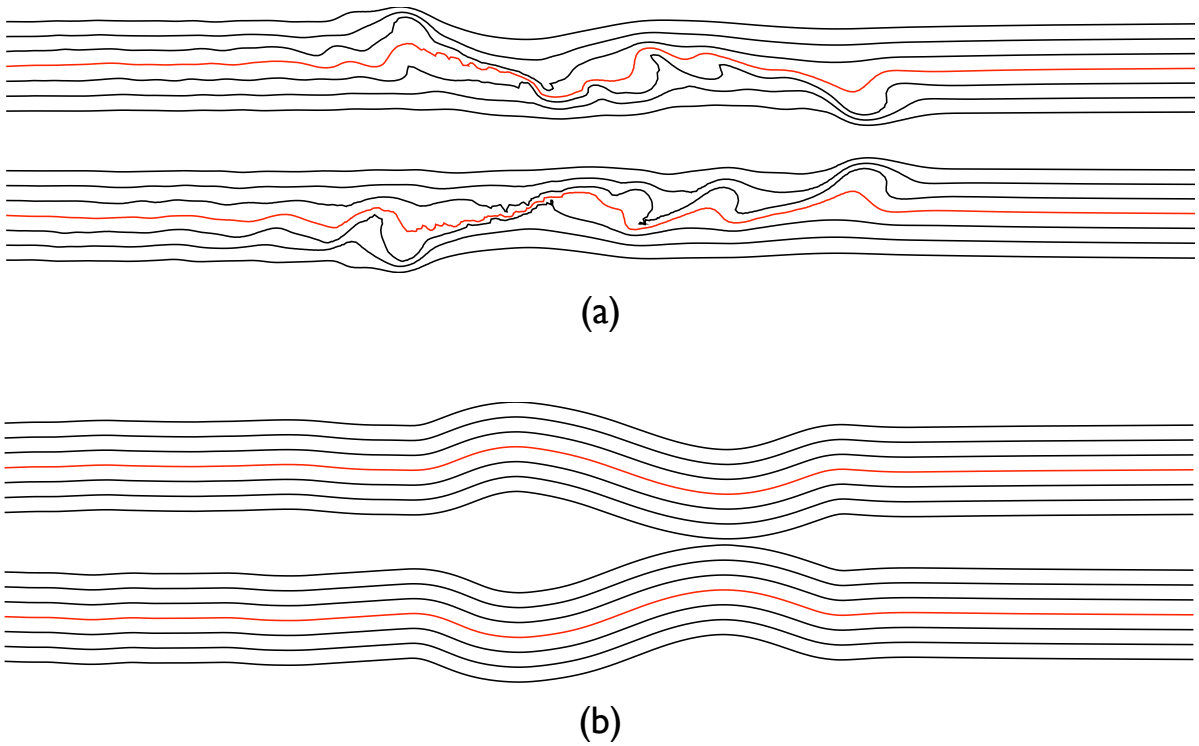

Figure 2.2: Simulation of a 2D jet with and without reinitializing level set. Red lines represent the phase interface where level set is zero, and black lines are non-zero level set contours with equally spaced values. (a). Without calling reinitialization (b) Calling reinitialization.

while the apparent disadvantage is the expensive computational cost. Some other less costly methods based on this concept are developed, such as narrow band method[22], which only perform such operation for grid contained in a narrow band near the interface.

The second category is PDE based, where instead of finding correct level set for each individual grid points by knowing the position of interface, one solves a partial differential equation to find the correct level set in a propagating manner [21, 62, 33]. The equation and its initial condition is

$$\frac{\partial \phi}{\partial \tau} = S\left(1 - \sqrt{\left(\frac{\partial \phi}{\partial x}\right)^2 + \left(\frac{\partial \phi}{\partial y}\right)^2 + \left(\frac{\partial \phi}{\partial z}\right)^2}\right), \tag{2.14}$$

$$\phi(\vec{x}, 0) = \phi_0(\vec{x}). \tag{2.15}$$

In the equation, S is the sign function, defined as

$$S = \frac{\phi_0}{\sqrt{\phi_0^2 + \sigma^2}}. \tag{2.16}$$

σ is a small number with magnitude comparable to the grid spacing, and it is used to ensure that the denominator of S is non-zero. If solving the above PDE to steady state, the regions with zero ϕ will remain zero, and ϕ will converge to the correct signed distance for other non-zero level set regions. The function S ensures that the propagating direction is always away from the interface. Thus, instead of solving the PDE to the steady state, one only needs several iterations to correct the level set values at the grid points near the interfaces. This method of reinitialization is shown to be effective and is adopted here.

Temporal approach

In a multiphase turbulent jet, complete breakup usually happens far downstream. In order to capture the spatially developing jet, the computational domain needs to be long enough in the streamwise direction to capture the droplets field. This will increase the computational cost significantly because of the large grid needed. Here, we propose using a temporal approach instead of the traditional spatial approach. In the temporal

approach, the reference domain is attached to the shear layer of the jet and moves downstream with the jet. The computational domain is a 3D box with fixed size. Periodic boundary condition is imposed in streamwise direction of the domain. Thus, the spatial development of the jet is captured at different instant of time as the jet within the computational domain evolves temporally.

2.1.2 Numerical simulations

Flow configuration

The flow under consideration consists of a three-dimensional round jet of diameter D. The interior fluid of the jet is assumed to be fluid 1 and the exterior fluid of the jet is assumed to be fluid 2. The density of the two fluids are assumed to be the same, while the viscosity ratio is $\mu_1/\mu_2 = 0.41$. The simulation is carried out in a temporal manner, with the reference frame attached to the shear layer of a spatially developing round jet. Initially, the interior fluid has a velocity of U_o, while the exterior fluid has a velocity of $-U_o$. The Reynolds number based on the jet diameter D, the velocity U_o and the viscosity μ_1, the density of the jet ρ_1 is $Re = \rho_1 U_o D/\mu_1 = 3000$. The surface tension cofficient is σ, and the Weber number based on the jet diameter is $We = \rho_1 U_o^2/\sigma = 1000$.

Numerical specifications

The computations are performed on a domain size of $4D \times 4D \times 4D$ in the x,y and z directions, respectively, as shown in Fig. 2.1.2. A uniformly-spaced grid is utilized and a resolution of $512 \times 512 \times 512$ is used. Random perturbations are added initially to the field to accelerate the breakup of the jet. The numerical method used to solve the Navier-Stokes equation is a predictor-corrector based finite-difference method that is second order accurate in time and fourth order accurate in space[63].

Results

Figure 2.1.2 shows the results from the temporal jet simulation. On the top image, it shows the jet simulated in a temporal manner at different instant of time. On the bottom image, a spatially developing liquid jet captured from the high speed imaging from experiments is shown. From the simulation, the jet in the simulation domain first

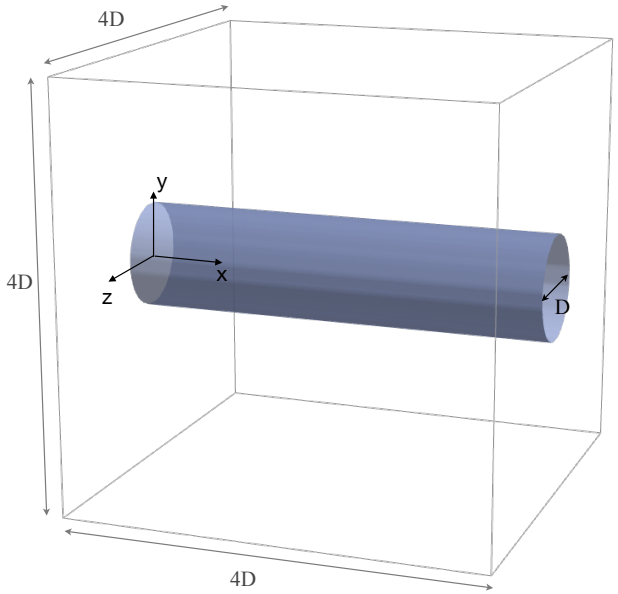

Figure 2.3: Computational domain of the temporal jet.

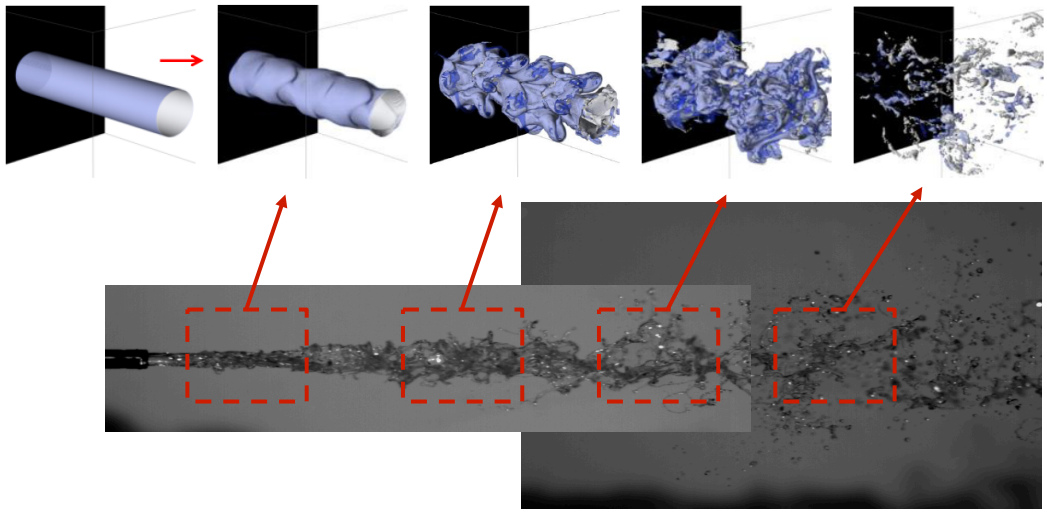

Figure 2.4: Top image: jet development is captured in a temporal manner in the simulation. Bottom image: a spatially developing jet captured from high speed imaging in experiments..

undergoes small perturbations at interfaces, then the perturbations grow and the jet expands in the outward direction. The jet completely breaks up into droplets in the last image. Comparing to the spatially developing jet at the bottom image, each of the breakup stage in the simulation are captured at different instant of time, and each stage corresponds to the flows at different streamwise direction of the spatially developing jet. Thus, the temopral approach is capable of capturing the development of the jet in a temporal manner and is able to reduce the computational cost significantly.

Figure 2.1.2 shows the instantaneous jet interface represented by zero level set iso-surface. In the flow, the bulk liquid column breaks down into liquid blobs, droplets and ligaments. Liquid ligaments can be observed forming on the side of the jet, e.g. on the top left of the figure, where the neck of the ligament is thinned and the tip tends to be pinched off. At the same time, finer droplets can be observed to be peeled off from the liquid interface at other locations of the jet. For turbulent flows such as sprays, flow field plays an important role in interfacial dynamics and the droplet formation process. To show the coupling between flow field and interfacial dynamics, vorticity contour and liquid interface are plotted on Fig. 2.1.2. In the figure, one can observe vortex rings forming periodically on the side of the jet. At the locations where these vortex rings are formed, droplets are peeled off from the interface, while at other locations of the jet where vorticity magnitude is lower, few or no droplet can be observed. High vorticity seem to increase the interfacial instabilities, leading to more breakup events and creating more droplets. Fig. 2.1.2 shows the coupling and interaction between droplets and vorticity field. Result is taken from an instant when the jet completely breaks up, and large amount of droplets are formed in the simulation domain. Droplets have sizes varying from small to large by orders of magnitude. The results show that there are fewer droplets formed near the center of the jet, while more droplets formed further away from the center.

To understand the dynamic process of the jet breakup and the droplet formation process, a more detailed analysis on the results is carried out. Two different breakup mechanisms are identified from the results. Figure 2.1.2 shows a time sequence showing the ligament pinch-off process. In (a), a ligament with with a bulb-like shape is formed at the side of the jet. Under the surface tension force, the ligament gets thinned in (b). In (c), the ligament breaks up and the droplet at the tip is pinched-off from the ligament.

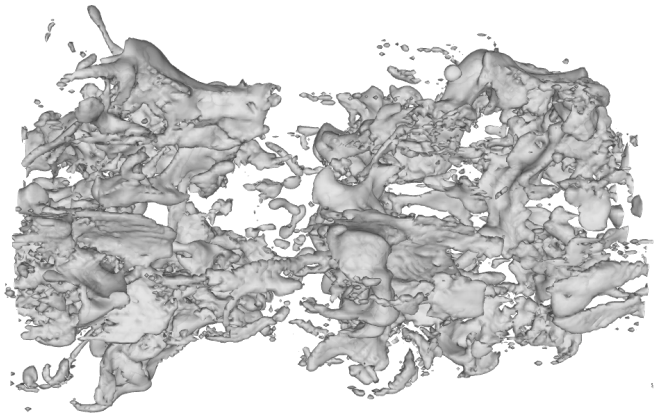

Figure 2.5: Liquid jet breakup from temporal simulation. Interface is represented by zero level set contour. Flow is from left to right.

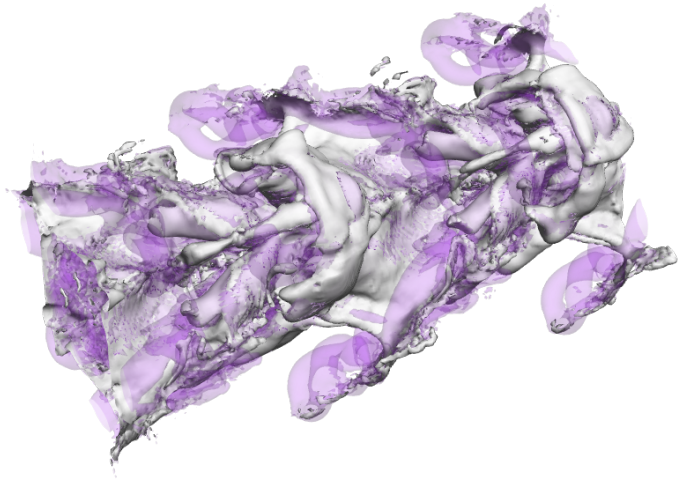

Figure 2.6: Interactions of vortex rings and droplet formation. Purple surface represents vorticity contour. White surface represents liquid interface.

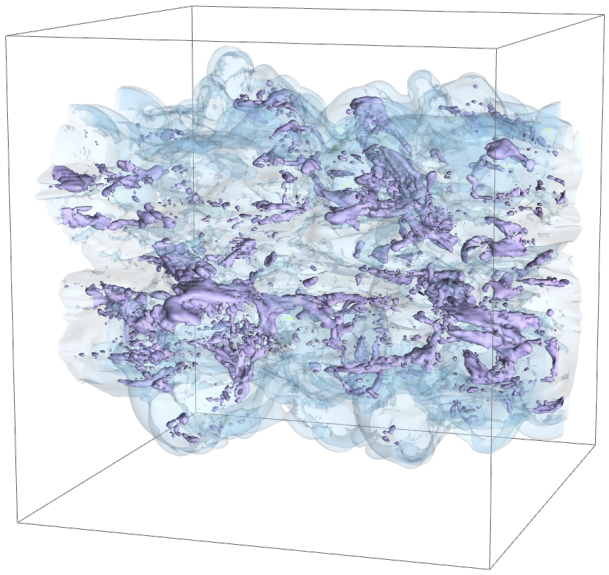

Figure 2.7: Droplet field after the jet breaks up. Blue surface represents vorticity contour. Purple surface represents liquid interface.

The droplet formed from the ligament pinch-off has a relatively large size, which is on the order of the the diameter of the initial ligament. Another breakup mechanism is the sheet breakup, as captured in Fig. 2.1.2. The figure shows a time sequence of sheet breakup. The blue surface shows the phase interface marked by zero level set isosurface. In (a), two holes show up on a thin sheet. Due to the large surface tension force at the edge of the hole, the holes quickly expands in area and forms several thin ligaments connecting the edge of the sheet, as captured in (b). The thin ligaments further breaks up as shown in (c), and the sheet disappears. Experiments have also identified those two breakup mechanisms. And it was found that the droplet sizes formed from the ligament pinch-off is usually much larger than the droplet formed from the sheet breakup.

2.2 A priori analysis of subgrid surface tension term

A priori analysis of subgrid terms in a 2D multiphase turbulent flow is carried out. In a multiphase interfacial flow, the traditional and familiar turbulent subgrid stress are

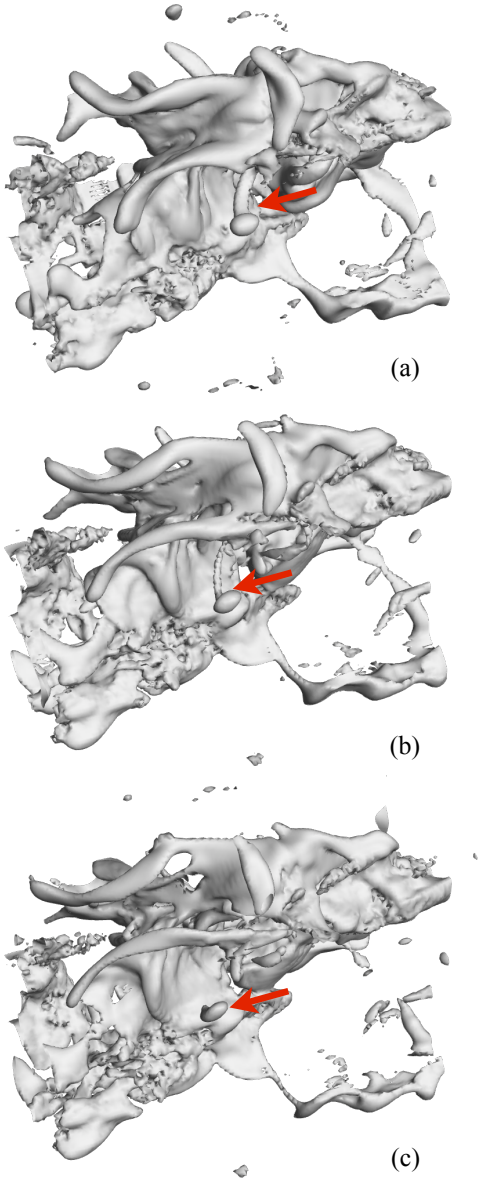

Figure 2.8: Time sequence shows ligament pinch-off. Interface is represented by zero level set isosurface.

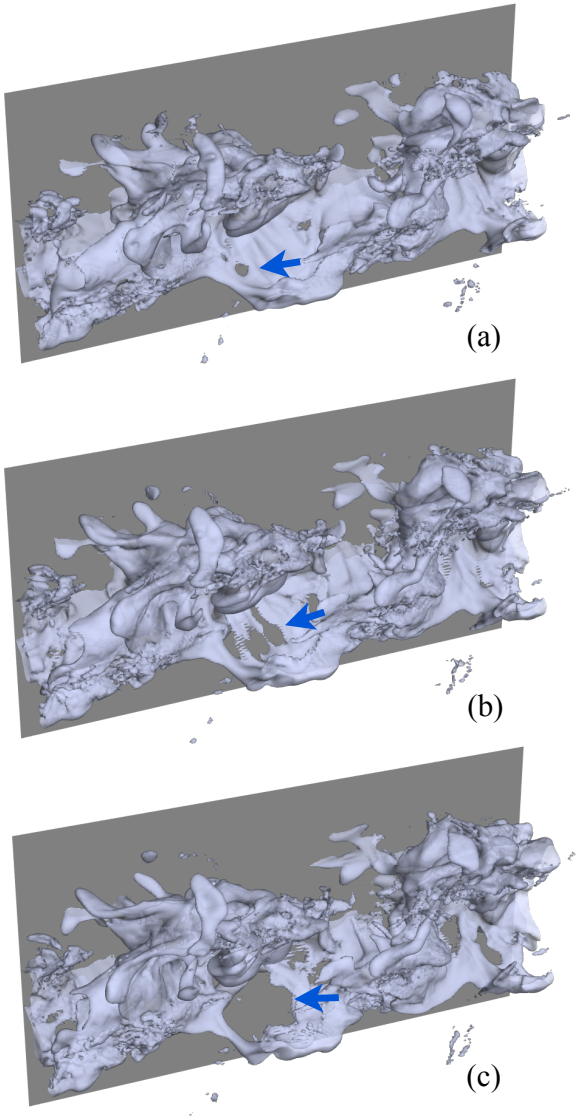

Figure 2.9: Time sequence shows sheet breakup. Interface is represented by zero level set isosurface.

present, as well as the not so much studied subgrid surface tension term. Recently, there have been a few articles in the literature investigating on the subgrid effect of the surface tension terms in turbulent multiphase flow [64][44] , but no validated SGS model has been set up yet. The goal of this section, is to perform a preliminary subgrid scale analysis on the DNS data from the 2D spatially developing planar jet, in order to help understand the effect of the new subgrid scale surface tension term.

2.2.1 Formulations

LES transport equations

The governing equations of the LES is obtained by filtering the Navier-Stokes equations and the scalar transport equations. Filtering operation on function $f(\mathbf{x}, t)$, in general can be represented by the convolution operation

$$\langle f(\mathbf{x}, t)\rangle = \int_{-\infty}^{+\infty}\int_{-\infty}^{+\infty} f(\xi, t')G(\mathbf{x}-\xi, t-t')dt'd^3\xi, \tag{2.17}$$

where $\langle f(\mathbf{x}, t)\rangle$ is the filtered quantity, G is convolution kernel. Top-hat filter is one of the most frequently used filters, where G can be expressed as

$$G(\mathbf{x}-\xi) = \begin{cases} 1/\overline{\Delta} & \text{if } |\mathbf{x}-\xi| \leq \overline{\Delta}/2 \\ 0 & \text{otherwise.} \end{cases} \tag{2.18}$$

This defines a filter width $\overline{\Delta}$ and takes the averaged value within the filter width as the filtered value. Filtering operations are able to separate the small scale subgrid information from the large scale information. Following the filtering operation and results in Chesnel et al[44], the filtered level set transport equation can be written as

$$\frac{\partial\langle\psi\rangle}{\partial t} + \frac{\partial\langle u_j\rangle\langle\psi\rangle}{\partial x_j} = \frac{\partial\Psi_j}{\partial x_j}, \tag{2.19}$$

where Ψ is the subgrid level set flux, given by

$$\Psi_j = \langle\psi u_j\rangle - \langle\psi\rangle\langle u_j\rangle. \tag{2.20}$$

Filtered Navier-Stokes equations can be written as

$$\frac{\partial \langle u_j \rangle}{\partial x_j} = 0, \tag{2.21}$$

$$\frac{\partial \langle \rho \rangle \langle u_i \rangle}{\partial t} + \frac{\partial \langle \rho \rangle \langle u_i \rangle \langle u_j \rangle}{\partial x_j} = -\frac{\partial \langle p \rangle}{\partial x_i} + \langle \mu \rangle \frac{\partial^2 \langle u_i \rangle}{\partial x_j \partial x_j} - \gamma \kappa^F \frac{\partial \psi}{\partial x_i} - \frac{\partial \tau_{ij}}{\partial x_j} + M_i - \frac{\partial \tau_i^{\rho u}}{\partial t} - \frac{\partial \tau_{ij}^{\rho uu}}{\partial x_j} + \tau_{ij}^{\mu u}, \tag{2.22}$$

where τ_{ij} is the SGS Reynolds stress given by

$$\tau_{ij} = \langle u_i u_j \rangle - \langle u_i \rangle \langle u_j \rangle. \tag{2.23}$$

Resolved curvature κ^F is calculated from the resolved level set. Thus, it will smear out the small scale structures of the interface geometry, producing a much flatter surface. This could have significant effects on the dynamics of droplet forming at small scales. Thus, subgrid surface tension force M_i is introduced to account for the small scale surface tension force, given by

$$M_i = -\gamma \left(\left\langle \frac{\partial \psi}{\partial x_i} \frac{\partial^2 \phi}{\partial x_j \partial x_j} \Big/ \sqrt{\frac{\partial \phi}{\partial x_j} \frac{\partial \phi}{\partial x_j}} \right\rangle - \frac{\partial \langle \psi \rangle}{\partial x_i} \frac{\partial^2 \langle \phi \rangle}{\partial x_j \partial x_j} \Big/ \sqrt{\frac{\partial \langle \phi \rangle}{\partial x_j} \frac{\partial \langle \phi \rangle}{\partial x_j}} \right). \tag{2.24}$$

Subgrid terms $\tau_i^{\rho u}$,$\tau_{ij}^{\rho uu}$,$\tau_{ij}^{\mu u}$ come from time derivative term, convective term and diffusive term, respectively:

$$\tau_i^{\rho u} = \langle \rho u_i \rangle - \langle \rho \rangle \langle u_i \rangle, \tag{2.25}$$

$$\tau_{ij}^{\rho uu} = \langle \rho u_i u_j \rangle - \langle \rho \rangle \langle u_i \rangle \langle u_j \rangle, \tag{2.26}$$

$$\tau_{ij}^{\mu u} = \langle \mu \frac{\partial^2 u_i}{\partial x_j \partial x_j} \rangle - \langle \mu \rangle \frac{\partial^2 \langle u_i \rangle}{\partial x_j \partial x_j}. \tag{2.27}$$

SGS temporal term $\tau_i^{\rho u}$ reflects the effect of the density discontinuity across the interfaces on time derivative term. This term increases with increasing density ratio, and will become zero when the density ratio of two phases is one. Similarly, $\tau_{ij}^{\rho uu}$ comes

from the effect of density discontinuity on convective terms, and $\tau_{ij}^{\mu u}$ comes from the effect of viscosity discontinuity across interface on diffusive term. These three terms are only non-zero near interface and will have a significant impact on interfacial dynamics in the cases where density ratio and viscosity ratio are large. Thus, the new subgrid terms introduced for multiphase interfacial flows comparing to the single phase flow simulations are M_i,Φ_j, $\tau_i^{\rho u}$,$\tau_{ij}^{\rho uu}$ and $\tau_{ij}^{\mu u}$.

2.2.2 Analysis of SGS surface tension terms

Flow configuration

The flow under consideration consists of a two-dimensional planar jet of diameter D, with a velocity of U_o issuing into a co-flowing stream with velocity U_∞. The jet to co-flow velocity ratio is $U_o/U_\infty = 1 : 0.4$. The interior fluid of the jet is assumed to be fluid 1 (liquid) and the exterior fluid of the jet is assumed to be fluid 2 (gas). The density ratio is $\rho_1/\rho_2 = 2 : 1$. The viscosity ratio is $\mu_1/\mu_2 = 0.4 : 1$. The Reynolds number based on the jet diameter D, the velocity U_o, the viscosity μ_1 and the density of the jet ρ_1 is $Re = \rho_1 U_o D/\mu_1 = 3500$. The surface tension cofficient is σ, and the Weber number based on the jet diameter is $We = \rho_1 U_o^2/\sigma = 50$.

Numerical specifications

The computations are performed on a domain size of $20D \times 16D$. A uniformly-spaced grid is utilized and a resolution of 1600×1200 is used. The numerical method used to solve the Navier-Stokes equation is a predictor-corrector based finite-difference method that is second order accurate in time and fourth order accurate in space[63].

Results

Figure 2.2.2(a) shows the jet interface marked by the volume of fluid, and Fig. 2.2.2(b) shows the jet interface marked by the level set. One can see that the interfacial structures shown by the two methods agree well because of the relatively high resolution employed here. Several interesting phenomena are captured in this simulation. The jet comes out from outlet and oscillations starts to grow along the interface. Later, long and thin ligaments are formed from these spikes, which are clearly shown in the magnified

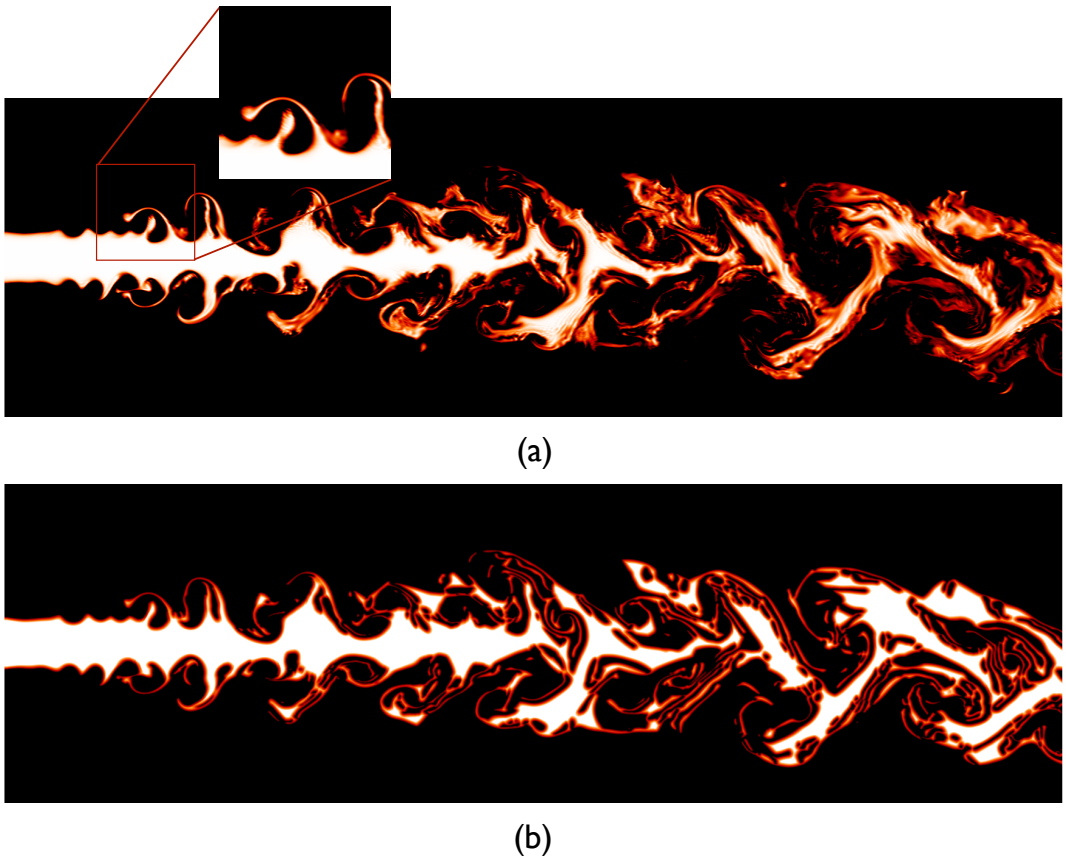

Figure 2.10: Top: 2D planar jet marked by the volume of fluid. Bottom: 2D planar jet marked by level set.

picture in Figure 2.2.2(a). The size of these ligaments grows as going downstream, and they start to get pinched off from the liquid column. Later, flow becomes turbulent and the bulk liquid column column breakup at around $x = 10D$. Further downstream towards the end of domain, periodic large scale coherent interfacial structures can be observed, and they are weakly connected to each other. Lots of small droplets and ligaments coexist with the coherent structures due to the turbulent small scale effect and interfacial pinch-off mechanism.

Figure 2.2.2 shows the non-dimensionalized surface tension force calculated using CSF method in the two-phase jet. One can see that the region where surface tension force acting on is now a 2D region instead of 1D, and having a thickness around the

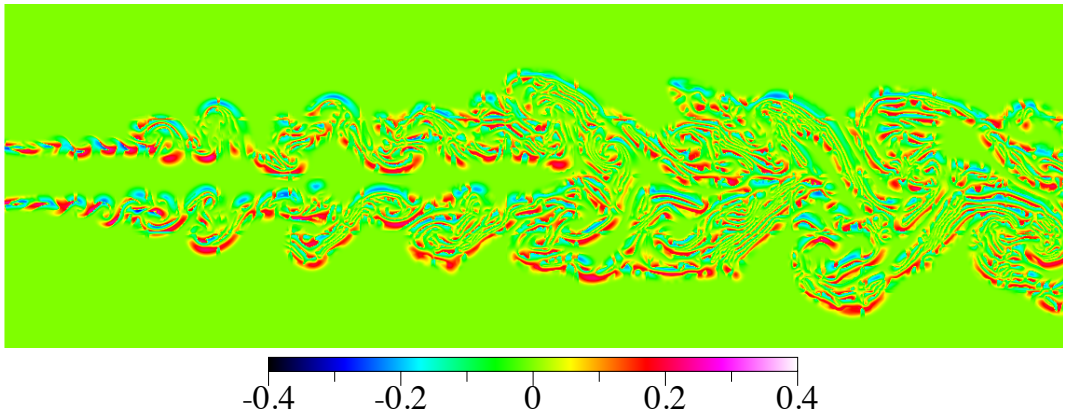

Figure 2.11: Surface tension force from DNS of a 2D planar jet. Positive value means the surface tension force pointing upwards, while negative value means the surface tension force pointing downwards.

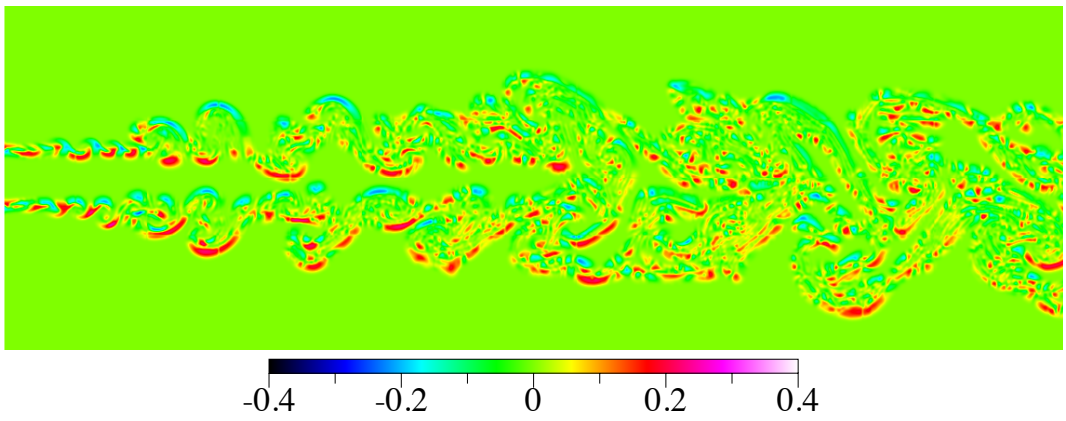

Figure 2.12: Filtered surface tension force calculated from DNS data. A top hat filter with width $\overline{\Delta} = 3\Delta x$ is used.

phase interface, with decaying magnitude away from interface. A preliminary SGS analysis is also performed. The goal is to show the effects of the aforementioned small-scale interactions on jet break-down. Surface tension term is filtered using a top-hat filter with filter width $\overline{\Delta} = 3\Delta x$. The SGS surface tension term is calculated, which equals the difference between the filtered surface tension term and the surface tension term calculated with filtered level set. Figure 2.2.2 shows the filtered surface tension term, and one can see that the small scale details are smeared out due to averaging. A close up view of the exact surface tension force is shown in Fig. 2.2.2(a) while the SGS component is shown in Fig. 2.2.2(b). The data show that the magnitude of the SGS component is the same as that of the total force, suggesting that the small-scale fluctuations may be significant in this case. One can see that the SGS term has both positive and negative components close to the interface and is acting in two ways. This keeps the liquid column from breaking up in some places and accelerates the break up at other places. The SGS surface tension term shown in Fig. 2.2.2(b) contains all the small scale information that are smeared out in the filtering operation. While the fine structures in Fig. 2.2.2(a) cannot be explicitly captured in a coarser mesh used in LES, by correctly modeling the sub-grid surface tension term shown in Fig. 2.2.2(b), one is able to reproduce the small scale structures and make correction on surface tension term shown in Fig. 2.2.2(a). In turn the small scale surface dynamics such as forming of small droplets will be captured correctly.

2.3 Conclusions

In this chapter, the direct numerical simulation of a multiphase turbulent jet is carried out. A temporal approach is adopted, and is shown to be effective in capturing the spatial development of the jet in a temporal way. Interactions between vorticity and jet breakup is looked into, and it was found that high vorticity leads to more breakup events. It was also found that fewer droplets are formed at the center of the jet, while more droplets are formed away from the center. The dynamics process of breakup is looked into, and two different jet breakup mechanisms are identified. The first one is ligament pinch-off. The second one is the sheet breakup. Similar breakup mechanisms are identified in the experiments, demonstrating the capability of the numerical tools

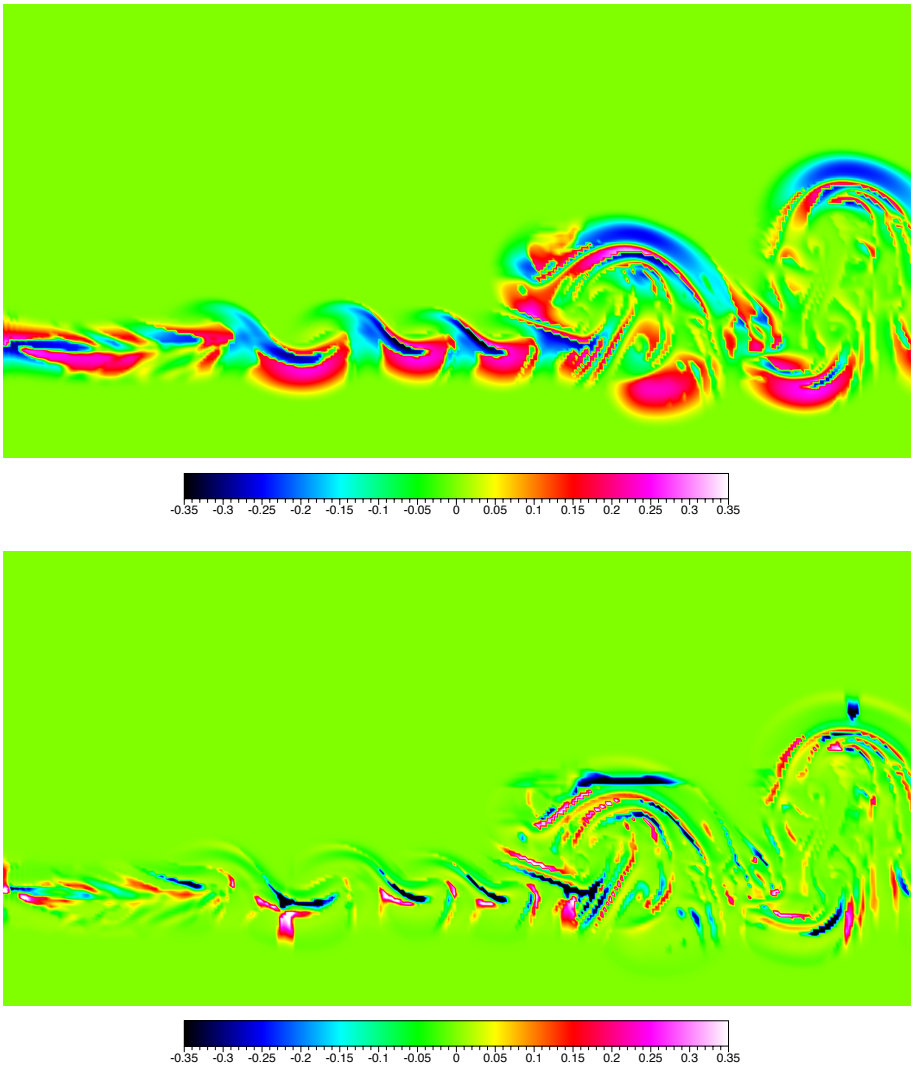

Figure 2.13: Close up view of surface tension force near the upstream of the jet. Left figure shows exact surface tension force, while right figure shows the SGS surface tension force. One can observe that SGS surface tension force have the same order of magnitude as the exact surface tension force, with both positive and negative components.

to correct capture the interfacial dynamics.

The subgrid analysis of the multiphase flow system is carried out. The filtering operations are first performed on the governing equations, and the results contain the new terms that do not show up in the single phase LES governing equations, including the term characterizing the viscosity and density difference between liquid and gas, as well as the SGS surface tension force. The SGS surface tension force turns out to be a highly non-linear term of the scalar. The filtering operations are performed on the DNS data of a 2D jet to obtain the filtered and SGS surface tension forces. It is found out that the magnitude of the SGS surface tension force is on the same order with the exact surface tension force. The SGS surface tension contains both positive and negative components, which act to stablize the jet at some places and de-stablize the jet at some places. The study suggests that the SGS surface tension might be difficult to model, while it can have a significant influence on small scale interfacial structures because of the local high Weber number for small scales.

Chapter 3

A Lagrangian volume-of-fluid methodology

We present a Lagrangian VOF (LVOF) approach for simulating the evolution of the multiphase flows. Particles carrying the local VOF value are randomly seeded in both liquid and gas. The advantage of this Lagrangian VOF approach is that it can eliminate the diffusive and dispersive errors present in the Eulerian VOF method, resulting in improved resolution of the interfaces. We utilize a modified surface tension model based on original models in SPH methods. In our approach, multiple particles are seeded in each cell for increased accuracy. Furthermore, We have clustered particles near the interface in order to achieve higher accuracy in the region where the surface force is present. A weighted SPH formula for calculating the color function is adopted to accommodate the variable particle number density, and a new kernel function is chosen that has better performance with variable particle seeding. The methodology is validated by carrying out test cases of an oscillating elliptical droplet in still fluid.

3.1 Formulation

3.1.1 SPH formulation for the surface tension

In the SPH method, a function $f(\mathbf{x})$ can be approximated by the convolution operation of kernel function, W, and the function itself, written as ([65])

$$g(\mathbf{x}) = \int f(\mathbf{x}')W(\mathbf{x} - \mathbf{x}', h)d\mathbf{x}'. \tag{3.1}$$

where $g(\mathbf{x})$ represents the kernel approximation of the function $f(\mathbf{x})$. The SPH method utilizes a kernel function (or weight function) W, to approximate a function and its derivatives. The kernel function W is an approximation to the Dirac delta function, but has a finite smoothing length h and satisfies

$$\lim_{h\to\infty} W(x, h) = \delta(x). \tag{3.2}$$

Additional properties of W can be found in [65]. The derivative $\frac{\partial f(\mathbf{x})}{\partial \mathbf{x}}$ may then be approximated by $h(\mathbf{x})$, which is calculated using the derivative of the kernel function,

$$\frac{\partial f(\mathbf{x})}{\partial \mathbf{x}} \doteq h(\mathbf{x}) = -\int f(\mathbf{x}')\frac{\partial W(\mathbf{x} - \mathbf{x}', h)}{\partial \mathbf{x}'}d\mathbf{x}'. \tag{3.3}$$

Use of the kernel function allows the derivative of a function to be expressed as the product of the function and the derivative of the kernel function. As the spatial domain is discretized by a set of particles, the smoother approximation of function f_i for particle i is given by

$$g_i = \sum_j W(|\mathbf{x}_j - \mathbf{x}_i|)f_j V_j, \tag{3.4}$$

where $\mathbf{x}_i$ is the location vector of particle i, and V_j is the spatial volume occupied by particle j. Similarly, the discrete form of the derivative for particle i is given by

$$\frac{\partial f}{\partial \mathbf{x}}|_i \doteq h_i = \sum_j \frac{\partial W(|\mathbf{x}_j - \mathbf{x}_i|)}{\partial \mathbf{x}} g_j V_j \tag{3.5}$$

where g_j is used in the summation instead of the original function f_j for a smoother/better approximation of the derivative. The derivative and divergence of the kernel function

function can be obtained analytically for a given kernel function. Morris developed a SPH-based method that uses the continuum surface force (CSF) model to calculate surface tension forces ([58]). In the CSF model, the surface tension is modeled as a volume force, calculated by

$$\mathbf{F}^{sv} = \delta_s \sigma \kappa \hat{\mathbf{n}}, \tag{3.6}$$

where δ_s is a surface delta function, σ is the surface tension coefficient, and κ is the interface curvature. This surface delta function reaches the peak value at the interface, decays to zero quickly away from the interface and has a finite thickness. The normal vector is calculated using a smoothly varying color function which satisfies $c = 1$ inside the liquid and $c = 0$ inside the gas,

$$\mathbf{n} = \nabla c. \tag{3.7}$$

The interface curvature, κ, is calculated from the divergence of the unit normal vector,

$$\kappa = \nabla \cdot \hat{\mathbf{n}}. \tag{3.8}$$

where the unit normal vector is $\hat{\mathbf{n}} = \mathbf{n}/|\mathbf{n}|$. The derivatives appearing in Eq. (4.7) and Eq. (4.9) are obtained using Eq. (3.5).

3.1.2 Lagrangian VOF

We propose an approach that tracks phase information – the VOF – on all particles while all other flow variables are solved via a traditional CFD solver on an Eulerian grid. Multiple irregularly distributed particles can be seeded in each Eulerian cell, and increasing number of particles will increase the statistical accuracy and resolution. In comparison, SPH treats each particle as a moving cell and solve all flow variables for each particle. The particles carry local VOF value, and their location vectors $\mathbf{x}_i$ are solved through the transport equation

$$\frac{d\mathbf{x}_i}{dt} = \mathbf{u}_i^p, \tag{3.9}$$

where $\mathbf{u}_i^p$ denotes the velocity vector of particle i, which is obtained by a second order interpolation based on Eulerian velocity. A major issue with traditional SPH is that it induces inconsistency error when the particles are irregularly or non-uniformly distributed. Efforts have been made to improve the inconsistency error in the variable particle seeding case, such as corrective smoothed particle method (CSPM) or finite particle method (FPM) ([66, 67, 65]). In these approaches the particle approximation of the function is derived from Taylor expansion, and given by ([65])

$$g_i = \frac{\sum_{j=1}^{N_p} W(|\mathbf{x}_j - \mathbf{x}_i|) f_j V_j}{\sum_{j=1}^{N_p} W(|\mathbf{x}_j - \mathbf{x}_i|) V_j}. \tag{3.10}$$

where N_p is the number of particles that are interacting with particle i. This definition leads to a consistent particle approximation of the function. However, in CSPM and FPM, in order to obtain a particle approximation of the derivative of the function, a 3×3 matrix or a 4×4 matrix must be solved for each particle in the domain for a three-dimensional problem, which increases the compute-time by roughly 300 to 400 percent and is not practical for large scale, three-dimensional simulations of turbulent flows ([66]).

In the LVOF, we retain the physical accuracy by adopting Eq. (3.10) as the definition for particle approximation of the function itself, while still using the original SPH formulation, Eq. (4.43), for the particle approximations of the derivatives. Multiple particles are seeded in each cell in both the gas and liquid phases, carrying the local VOF value, ψ_i. The particle approximation to the color function, c, is computed based on this VOF and is given by

$$c_i = \frac{\sum_{j=1}^{N_p} W(|\mathbf{x}_j - \mathbf{x}_i|) \psi_j V_j}{\sum_{j=1}^{N_p} W(|\mathbf{x}_j - \mathbf{x}_i|) V_j}, \tag{3.11}$$

where ψ_i is the VOF on particle i. The surface tension for particle i, $\mathbf{F}_i$, is calculated on the interface particles via

$$\mathbf{F}_i = \delta_s \sigma \kappa_i \hat{\mathbf{n}}_i, \tag{3.12}$$

where, as before, the unit normal vector is given by $\hat{\mathbf{n}}_i = \mathbf{n}_i / |\mathbf{n}_i|$, and the particle normal

vector $\mathbf{n}_i$ is calculated through the gradients of the color function,

$$\mathbf{n_i} = (\nabla c)_i = \sum_{\substack{j=1 \\ i \neq j}}^{N_p} \nabla W(|\mathbf{x}_j - \mathbf{x}_i|) c_j V_j. \tag{3.13}$$

In the summation, the particle i is excluded to avoid the situation in which the gradient of kernel function doesn't exist. The interface curvature, κ_i, is calculated using the divergence of the unit normal vector

$$\kappa_i = \nabla \cdot \hat{\mathbf{n}}_i = \sum_{\substack{j=1 \\ i \neq j}}^{N_p} \nabla W(|\mathbf{x}_j - \mathbf{x}_i|) \cdot \hat{\mathbf{n}}_j V_j. \tag{3.14}$$

Additional improvement in accuracy can be achieved by replacing the function value inside summation with the differences of the function between nearby particles ([58, 65]), which can reduce the particle inconsistency error in the derivative calculation. The improved equations are written as

$$\mathbf{n_i} = (\nabla c)_i = \sum_{\substack{j=1 \\ i \neq j}}^{N_p} \nabla W(|\mathbf{x}_j - \mathbf{x}_i|)(c_j - c_i) V_j, \tag{3.15}$$

$$\kappa_i = \nabla \cdot \hat{\mathbf{n}}_i = \sum_{\substack{j=1 \\ i \neq j}}^{N_p} \nabla W(|\mathbf{x}_j - \mathbf{x}_i|) \cdot (\hat{\mathbf{n}}_j - \hat{\mathbf{n}}_i) V_j, \tag{3.16}$$

and the delta function, δ_s, for particle i is given by $\delta_s = \lambda |\mathbf{n_i}|$, where the calibration factor λ is constant. An additional filtering step on the unit normal vector proposed by [58] is adopted. The normal vectors are effectively "clipped" or set to a threshold value using

$$\tilde{\mathbf{n}}_i = \begin{cases} \mathbf{n}_i / |\mathbf{n}_i|, & \text{if} \quad |\mathbf{n}_i| > 0.01/h, \\ 0, & \text{otherwise.} \end{cases} \tag{3.17}$$

The clipping is needed because near the edge of the interface, the magnitude of normal vector will be small and error-prone. Thus, the unit normal vector calculated based on it will be oscillatory and not reliable for these particles. The surface tension term

appearing in the Eulerian momentum equation is obtained by averaging the particle values inside the cell,

$$\mathbf{F}^s = \frac{\sum_{i=1}^{N_{pc}} \mathbf{F}_i V_i}{\sum_{i=1}^{N_{pc}} V_i} = \frac{\sum_{i=1}^{N_{pc}} \delta_s \sigma \kappa_i \tilde{\mathbf{n}}_i V_i}{\sum_{i=1}^{N_{pc}} V_i}, \tag{3.18}$$

where N_{pc} is the number of particles in the cell.

The result is an "SPH-like" formulation that utilizes the particle data only in the interfacial regions. The particles whose color function lie in the range $0 < c_i < 1$ are marked as interface particles, and surface tension is calculated only for these particles.

3.2 Performance evaluation

We assess the performance of the formulation via three means. First, we examine the flow-field generated for the inlet of a round jet via SPH and via our formulation with both uniform and variable particle densities. We also perform the rotation of a Zalesak disk, and simulate the oscillation of an initially elliptical droplet.

3.2.1 Initial field near a circular orifice

The flow of liquid through a circular orifice, and the subsequent generation of a spray, is of significance in a variety of engineering problems ([1]). The color function, normal vector and curvature at the inlet of a a round jet are evaluated using both conventional unweighted SPH approach and LVOF approach. The radius of the jet is $r_o = 1$. The fluid within the jet ($r \leq 1$) is liquid with a VOF value of $\psi = 1$ while the fluid outside the jet is gas with a VOF value of $\psi = 0$.

Numerical parameters

A uniform rectangular grid is used to discretize the field. The grid consists of 40 points in the x and y directions across the diameter of the jet. The grid spacing is $\Delta x = \Delta y = 0.05$. Particle are seeded in both liquid and gas within a circle with radius of $R = 2$. The choice of the kernel function has a significant influence on the performance of the SPH model of surface tension. A typical function is the spike shaped

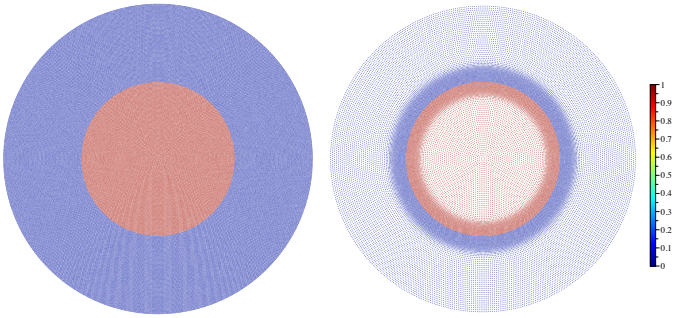

Figure 3.1: Distribution of Lagrangian particles, colored by the VOF, near circular orifice: (a) uniform particle distribution ($N_{pc} = 16$); (b) variable particle distribution ($N_{pc} = 16$ near the interface and $N_{pc} = 4$ elsewhere).

kernel proposed by [61] given by

$$W_1(r) = A\left(\frac{3}{r_e}\right)^d \begin{cases} (1 - r/r_e)^3, & r < r_e, \\ 0, & \text{otherwise}, \end{cases} \tag{3.19}$$

where d is the number of spatial dimensions, A is the normalization factor, defined as

$$A = \begin{cases} \frac{10}{9\pi}, & d = 2, \\ \frac{5}{9\pi}, & d = 3, \end{cases} \tag{3.20}$$

and r_e is influence radius. Within the influence radius r_e, particles can interact with each other, and the influence of interactions decreases as the distance between two particles increases. The influence radius r_e is defined based on the grid spacing as $r_e = n_g \Delta x$, where Δx is the grid spacing. In this work we set the influence radius to $r_e = 2\Delta x$.

Both a uniform seeding case and a variable particle density seeding case are tested in order to evaluate the performance of the original SPH formulation and the LVOF. In the uniform seeding case, approximately $N_{pc} = 16$ particles are seeded per Eulerian grid cell. In the variable particle density seeding case, approximately $N_{pc} = 16$ particles are seeded per Eulerian cell in the interface region – $r = 1 \pm r_e$ – and $N_{pc} = 4$ particles per cell are seeded elsewhere. Transition between the two zones is made smooth by utilizing a hyperbolic tangent profile. The different seeding conditions are shown in Fig. 3.1.

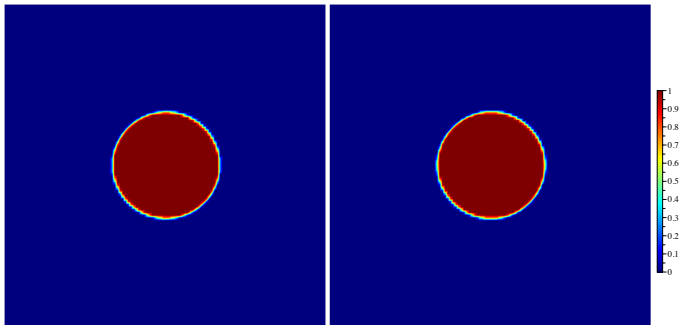

Figure 3.2: Mean VOF on eulerian grid: (a) uniform particle distribution ($N_{pc} = 16$); (b) variable particle distribution ($N_{pc} = 16$ near the interface and $N_{pc} = 4$ elsewhere).

Table 3.1: Parameters for initialization near circular orifice.

Case	Formulation	Number density
1	LVOF	$N_{pc} = 16$
2	LVOF	$N_{pc} = 4 + 12 \times \tanh(8 \times (r - 1))$
3	SPH	$N_{pc} = 4 + 12 \times \tanh(8 \times (r - 1))$

This is the Lagrangian equivalent of grid clustering, employed in traditional Eulerian solvers ([14]). The mean VOF, shown in Fig. 3.2, are the same in both cases. We use both these seedings to analyze the performance potential of the LVOF approach. The parameters for the different analyses are shown in Table 3.1.

The surface delta function δ_s and curvature are also calculated based on the color function using both formula Eq. 3.4 and Eq. 3.10. For this test case, the curvature is computed for all particles in the domain.

Results

The color function, c_i, may be thought of as a "smoothed" version of the VOF. Inside each phase it has a uniform value - $c_i = 1$ inside the liquid, and $c_i = 0$ inside the gas. While the VOF has a sharp jump from $\psi = 1$ to $\psi = 0$ from liquid to gas, the color function varies continuously and smoothly from from liquid to gas over a finite thickness at interfaces, usually on the order of grid spacing. Such variation makes it

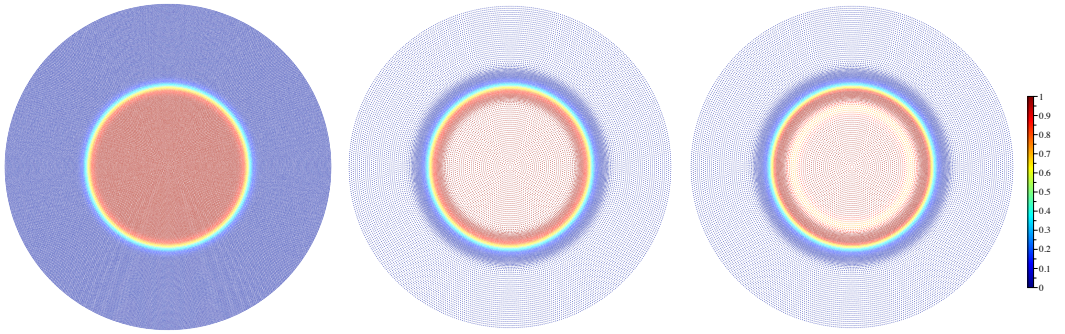

Figure 3.3: Particle color function near orifice.

possible to calculate the gradients needed to obtain the interface normal vectors. The color function for the three cases are shown in Fig. 3.3. In case 1 – the uniform particle number seeding – the color function is $c_i = 1$ in the liquid and $c_i = 0$ in the gas. The results for case 2 – the variable particle seeding and LVOF – are similar those in case 1. However, in case 3 – the variable particle seeding and SPH – the variable particle number density leads to a variation in the value of color function within the liquid region, which is shown as a yellow ring in Fig. 3.3(c) inside the liquid region, corresponding to a value below 1. A more quantitative view of the color function is shown in Fig. 3.4. The plots show that the color function varies smoothly from a value of $c = 1$ to $c = 0$ with increasing radius for both case 1 and case 2. However, in case 3 there are significant variations in the transition region. Such variations in the color function will be identified as phase transitions that do not really exist. I.e. they will lead to unphysical interfaces. Furthermore, they may lead to significant oscillations in the normal vector and curvature. Thus, using the LVOF formula eliminates the "artificial gradient" in the color function present inside the liquid.

The interface curvature represents the amount by which the multiphase interface deviates from a flat surface. Large curvature values represent a larger deviation from the flat shape and leads to a larger surface tension acting to return the interface to its equilibrium position. The particle curvature values κ_i are shown in Fig. 3.5. These are calculated based on the color function c_i, and the consequences of the varying color function are more readily apparent. The result for case 1 is shown in Fig. 3.5(a).

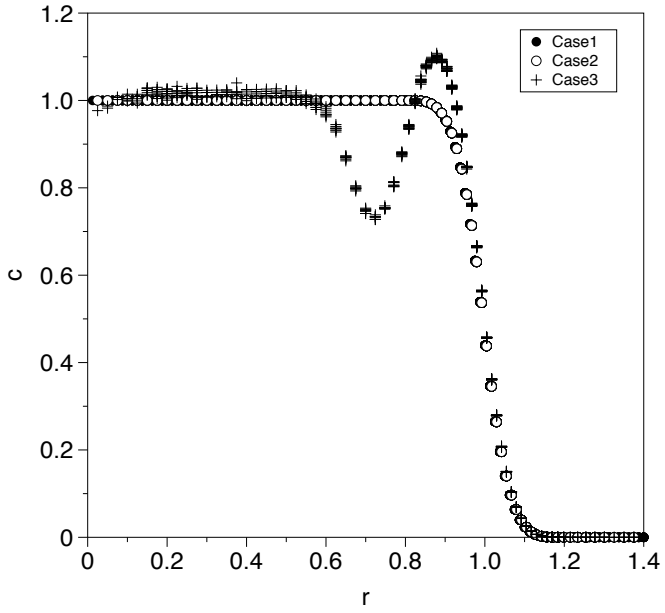

Figure 3.4: Color function c as a function of radius.

The figure shows that the curvature is only non-zero in the interfacial region, where the interfacial region is defined as $r = r_o \pm r_e$. Using the LVOF formula, case 2, the curvature calculation for variable particle number density case is close to that with uniform particle number density. In these two cases, the curvature has a uniform, non-zero value only within a thin band near the interface. In case 3, there appears to be large variations of curvature inside the liquid region. This is caused by the artificial gradient in color function using the unweighted SPH formula.

The magnitude of the normal vector and curvature are shown as function of radius in Fig. 3.6. The surface delta function, proportional to the magnitude of normal vector $|\mathbf{n}|$, defines profile and thickness of the surface tension across interface. It is a finite approximation of the delta function, which reach a peak value at interface and decays monotonically to zero away from the interface region. Such choice of surface delta function allows the surface tension to be localized to the interfacial regions. The normal vectors are shown in Fig. 3.6(a). The plot reveals that in cases 1 and 2, the normal vector increases monotonically inside the liquid as radius increases, and reach peak value at $r = 1.0$. While in case 3, the magnitude of normal vector has large oscillations inside

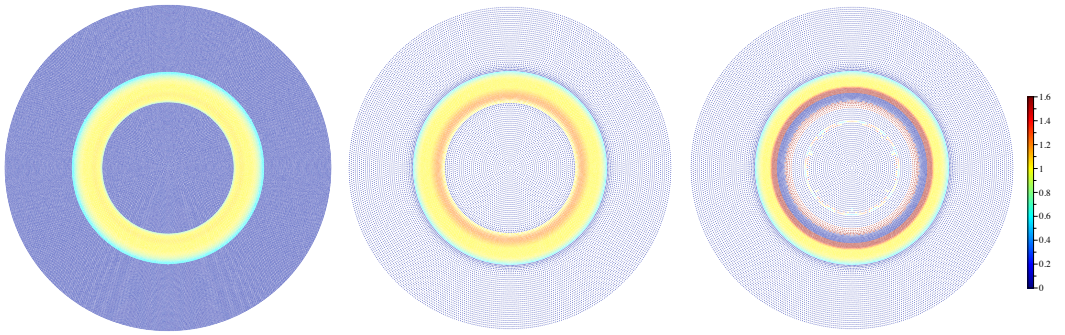

Figure 3.5: Particle curvature field near orifice.

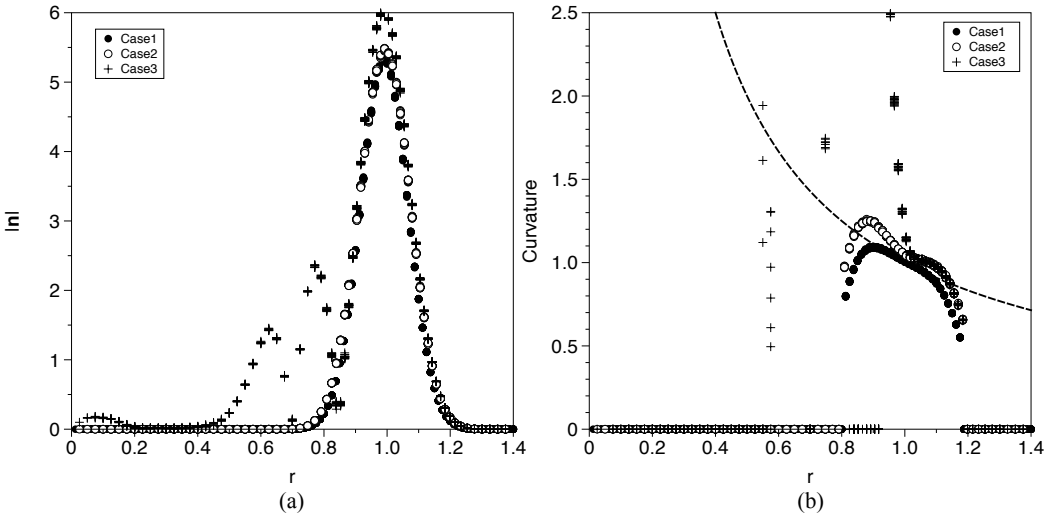

Figure 3.6: Scatter plots of (a) magnitude of normal vector, $|\mathbf{n}_i|$, and (b) curvature, κ_i. The dashed line is the analytical value.

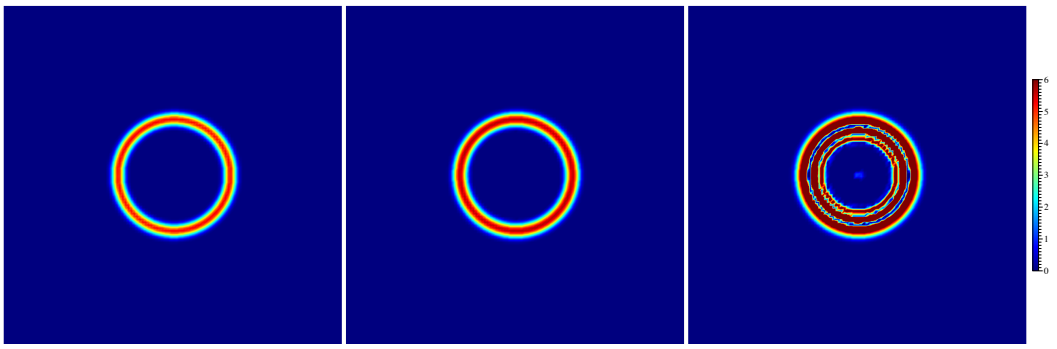

Figure 3.7: Contours of the Eulerian mean magnitude of surface tension, $|\mathbf{F}^s|$.

liquid. This will lead to a non-physical oscillating surface tension force that is non-zero inside the single phase region. The incorrect calculation of normal vector will also cause incorrect variations of the curvature, as shown in Fig. 3.6(b). The results show that cases 1 and 2 agree well with the theoretical value. In comparison, the curvature obtained in case 3 shows significant deviations in the liquid region ($r < 1$). Such large errors will lead to a non-physically large surface tension force that acts to move interfaces incorrectly.

Contours of the magnitude of the non-dimensional surface tension force, $|F_s|$, are shown in Fig. 3.7. Very good agreement is observed between case 1 and case 2. However, in case 3, the results reveal that an artificial surface tension is present inside the liquid region. These results show that the LVOF approach based on weighted particle VOF is more suitable to handle the variable number density particle distribution which can be utilized in complex multiphase turbulent flow applications. The LVOF approach can avoid the creation of artificial interfaces, oscillations and artificial gradients in the variable particle number density situations.

3.2.2 Rotation of Zalesak disk

The rotation of Zalesak's disk ([68]) is tested to demonstrate the capability of Lagrangian volume of fluid method to preserve sharp structures. In the test cases, the size of the simulation domain is 100×100. Grid spacing is $\Delta x = \Delta y = 1$. The center of the disk is

placed at $(x, y) = (50, 75)$, and the radius of the disk is $r_d = 15$. This disk has a notch with width of $L_a = 5$ and length of $L_b = 25$. A VOF value of $\psi = 1$ is assigned inside the disk and a value of $\psi = 0$ is assigned outside the the disk. The velocity field is given by

$$u = \frac{\pi}{314}(50 - y), \tag{3.21}$$

and

$$v = \frac{\pi}{314}(x - 50). \tag{3.22}$$

With the field being given, the disk follows rigid body rotation and completes one cycle, returning to its original position at time $t = 628$. The purpose is simply to illustrate the advection properties of the scheme. The velocity of the LVOF particles is obtained by evaluating the above velocity at the particle locations. Given that this is an "exact" evaluation, its value is not simply to show that the interface is preserved but rather to illustrate the effects of particle number density on resolving the interface. Figure 3.8 shows a full rotation cycle of the disk in the eight particles per grid cell ($N_{pc} = 8$). As expected, the end of the cycle, the disk returns to its original location with the shape as the initial configuration, and all sharp corners are preserved.

The effect of particle number density can be observed in Fig. 3.9. Three simulations are performed, each with a different particle number density: (a) $N_{pc} = 2$; (b) $N_{pc} = 4$; and (c) $N_{pc} = 8$. The LVOF particles are shown in panels *a, b* and *c,* while the Eulerian-mean VOF, ψ, are shown in panels *d, e* and *f.* The mean VOF is obtained by averaging all LVOF values in the grid cell and is given by

$$\psi = \frac{\sum_{i=1}^{N_{pc}} \psi_i V_i}{\sum_{i=1}^{N_{pc}} V_i} \tag{3.23}$$

The results show that the structure/shape is preserved in all cases. In the $N_{pc} = 2$ case, the mean VOF has more oscillations than the $N_{pc} = 8$ case. This suggests that higher particle concentrations are needed to avoid spurious oscillations. In the simulation of turbulent flows, Lagrangian based methods typically employ a minimum of 25 to 40 particles per grid cell, and oftentimes many more ([69, 70]).

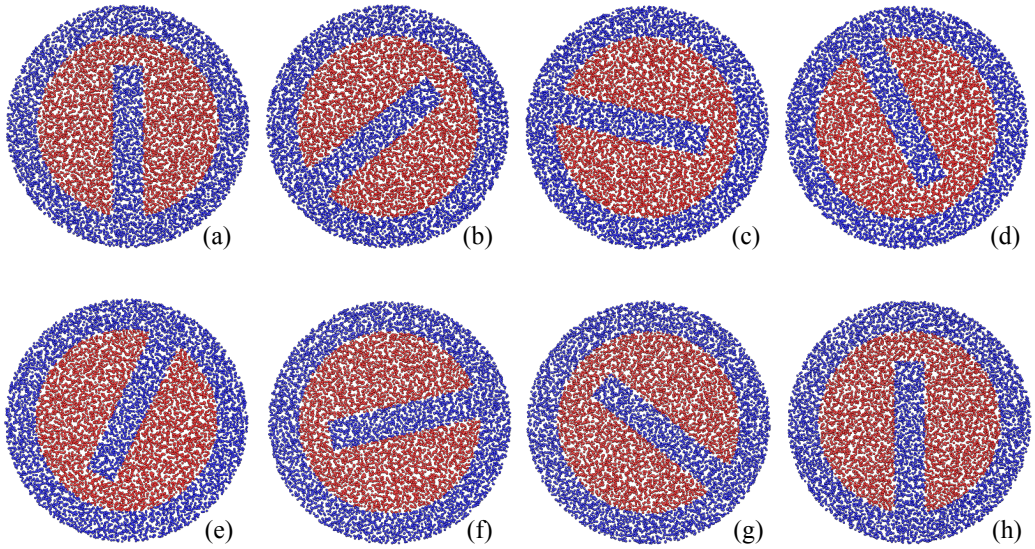

Figure 3.8: A full rotation cycle of Zalesak's Disk. LVOF particles are shown, where red represents $\psi_i = 1$ and blue represents $\psi_i = 0$.

3.2.3 Oscillation of an elliptical droplet

The oscillation of a two-dimensional elliptical droplet is simulated using the LVOF approach under different particle number density cases. The flow is assumed to be incompressible, Newtonian, two phase flow. An elliptical droplet with major axis $e_a = 2$ and an aspect ratio of $3 : 2$ is placed in a quiescent fluid. The droplet will oscillate under the restoring effect of surface tension which is ultimately damped by viscous forces. The governing equations are the incompressible Navier-Stokes equations composed of conservation of mass equation given by

$$\frac{\partial u_j}{\partial x_j} = 0, \tag{3.24}$$

where u_j is the velocity in the j-direction, and the conservation of momentum equation

$$\frac{\partial \rho u_i}{\partial t} + \frac{\partial \rho u_i u_j}{\partial x_j} = -\frac{\partial p}{\partial x_i} + \mu \frac{\partial^2 u_i}{\partial x_j \partial x_j} - F_i^s. \tag{3.25}$$

where p is the pressure and F_i^s is the force due to surface tension in the i-direction. The surface tension force is obtained from the LVOF via Eq. (3.18). Similarly, the Eulerian

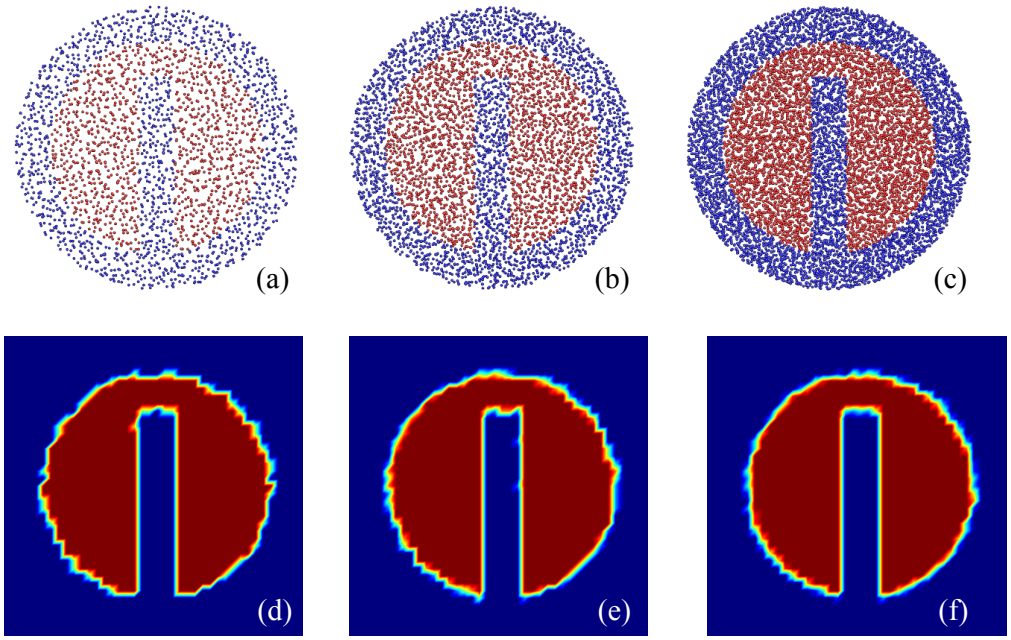

Figure 3.9: Volume of fluid after 1 rotation of the disk. Top row shows LVOF, and bottom row shows Eulerian mean VOF: (a) and (d) are $N_{pc} = 2$; (b) and (e) are $N_{pc} = 4$; and (c) and (f) $N_{pc} = 8$.

VOF, ψ, is obtained from the LVOF via Eq. (3.23). The fluid density is a function of the VOF

$$\rho = \psi\rho_i + (1-\psi)\rho_e, \tag{3.26}$$

where ρ_i and ρ_e are the density of the interior fluid and the exterior fluid, as is the viscosity μ

$$\mu = \psi\mu_i + (1-\psi)\mu_e, \tag{3.27}$$

where μ_i and μ_e are the viscosity of the interior fluid and the exterior fluid. In this simulation, the interior and exterior fluid are assumed to have the same density and viscosity. The equations are non-dimensionalized using the characteristic length scale of the droplet, $L = \sqrt{2/3}e_a$, and the characteristic velocity given by

$$U_o = \sqrt{\frac{\sigma}{\rho_d L}} \tag{3.28}$$

The characteristic time scale is defined as the capillary time scale $t_o = L/U_o$. With these, the Reynolds number Re is given by

$$Re = \frac{\rho_d U_o L}{\mu_d} \tag{3.29}$$

and Weber number We is calculated by

$$We = \frac{\rho_d U_o^2 L}{\sigma} = 1. \tag{3.30}$$

In this simulation, the Reynolds number is chosen to be $Re = 10$. The non-dimensional period of the oscillation, t_p, for an inviscid flow is calculated from

$$t_p = 2\pi\sqrt{\frac{1+\rho_e/\rho_i}{n^3-n}} = 2\pi\sqrt{\frac{2}{n^3-n}}, \tag{3.31}$$

where the parameter n characterizes the initial shape of the droplet ([11]). For the elliptical configuration, $n = 2$ and the non-dimensional period is calculated to be $t_p = 3.63$.

Numerical parameters

The computational domain size is of size $6e_a \times 6e_a$ and the droplet is placed at the center. A uniformly-spaced, rectangular grid comprised of 240×240 points is used. The non-dimensionalized Navier-Stokes equations are solved using a predictor-corrector finite-difference based scheme that is second order accurate in time and fourth order accurate in space ([63]). Particles are seeded randomly in both the exterior and interior fluids based on the Eulerian grid, with each cell having N_{pc} particles. Four different particle seedings are utilized: $N_{pc} = 6$, $N_{pc} = 8$, $N_{pc} = 12$ and one variable seeding case where $N_{pc} = 12$ at the interface and $N_{pc} = 2$ elsewhere. A calibration factor of $\lambda = 0.3$ is used ([61]). We have found that using the polynomial based spike function kernel, W_1 specified in Eq. 3.19, induces an influence radius that is too large for the results to be stable. This is because the kernel function decays quickly for nearby particles, and slowly for particles farther away. The higher contribution of the nearby particles amplifies the effect of randomness in the location of particles, thus decreasing the statistical accuracy. One way to reduce the effect of randomness is to increase number of particles or increasing influence radius such that more particles are sampled. We utilize another spike shaped kernel function W_2 given by

$$W_2(r) = A \begin{cases} e^{-c\frac{r}{r_e}} - e^{-c}, & r < r_e, \\ 0, & \text{otherwise} \end{cases} \tag{3.32}$$

where A is a normalization factor, defined as

$$A = \begin{cases} (2\pi r_e^2[\frac{1}{c^2} - (\frac{1}{c} + \frac{1}{c^2} + \frac{1}{2})e^{-c}])^{-1} & d = 2, \\ (4\pi r_e^3[\frac{2}{c^3} - (\frac{1}{c} + \frac{2}{c^2} + \frac{2}{c^3} + \frac{1}{3})e^{-c}])^{-1} & d = 3. \end{cases} \tag{3.33}$$

The constant c may be used to adjust the shape of the spike function. As c increases, particles close to center will have more weight while particles farther away will be weighted less. As c decreases, increasing weight will be put onto particles that are farther away. Here, we choose $c = 0.01$. A comparison between kernel function W_1 and W_2 is shown in Fig. 3.10. A value of $n_g = 2.0$ is used for influence radius r_e. The kernel function W_2 allows higher contribution of the farther away particles in the weight function comparing to the previous fast decay kernel function. Thus, a smaller influence

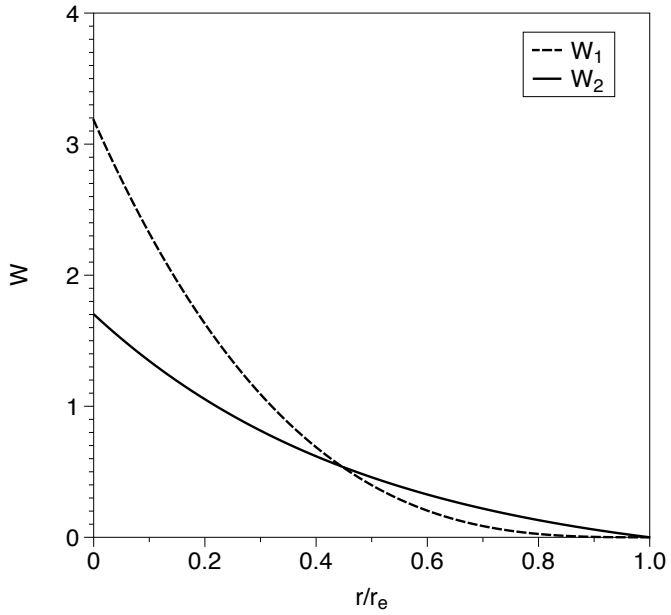

Figure 3.10: Comparison of kernel functions W_1 and W_2 as a function of radius.

radius can be used, which leads to a sharper interface.

Results

Instantaneous distributions of the LVOF particles at four different times are shown in Fig. 3.11. The results are for the uniformly particle distribution simulation – panels *a* through *d* – and clustered particles – panels *e* through *h*. The red particles represent the interior fluid and the blue color represents the exterior fluid. Time $t^\star = 0$ represents the initial time where the surface tension at the two tips in the major axis is larger than that in the minor axis due to larger curvature. This leads to contraction of the droplet along the major axis and expansion along the minor axis. At time $t^\star = 2.14$, the initially elliptical droplet deforms into a circular droplet and continues to deform due to inertia, until the major axis and minor axis are switched, as shown in Fig. 3.11(c) and Fig. 3.11(d). The droplet continues to oscillate in this way until the motion is damped by viscosity, at which point the droplet remains in the equilibrium circular shape.

Instantaneous contours of the magnitude of surface tension force, $|F_i^s|$ are shown in Fig. 3.12. Results are shown for two cases. Figure 3.12(a) shows the result for a particle

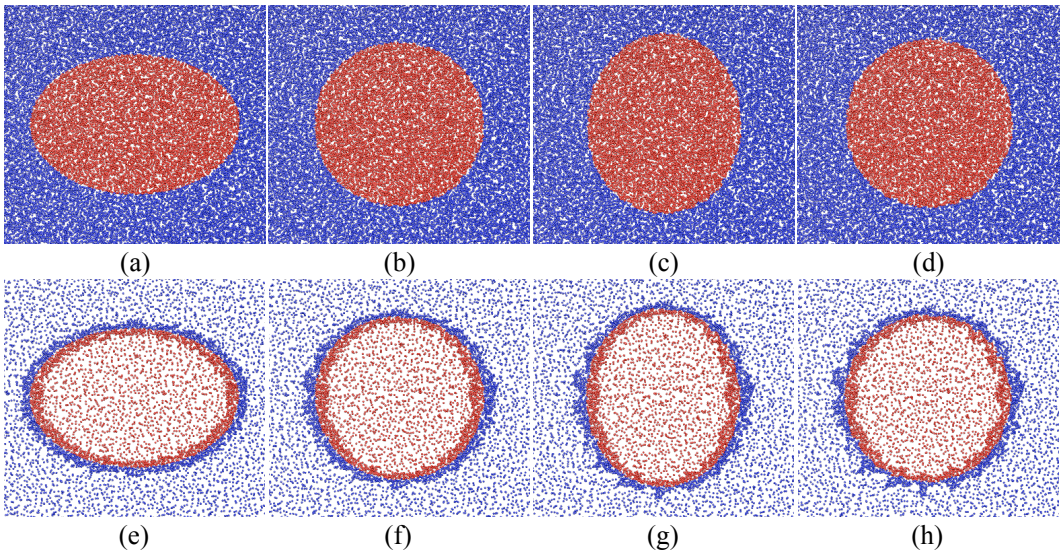

Figure 3.11: Particle VOF fields at four different times: $t^\star = 0$; $t^\star = 1.12$; $t^\star = 2.14$; and $t^\star = 3.18$. The upper images, a - d, are of the uniform particle seeding ($N_{pc} = 12$) and lower images, e - h, are of the variable particle seeding.

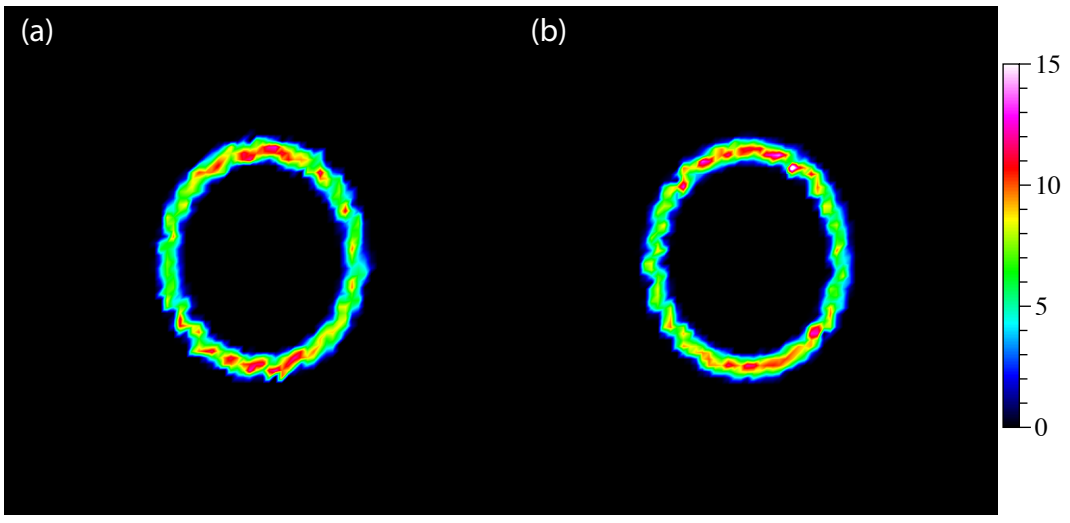

Figure 3.12: Instantaneous contours of the magnitude of the mean surface tension force, $|F_i^s|$: (a) variable particle seeding ($N_{pc} = 12$ near the interface and $N_{pc} = 2$ elsewhere); (b) uniform particle seeding ($N_{pc} = 8$).

seeding of $N_{pc} = 12$ in the interfacial region and $N_{pc} = 2$ elsewhere, and Fig. 3.12(b) shows the result for a constant or uniform particle seeding of $N_{pc} = 8$. The contours show that by increasing the resolution in the interface and decreasing it elsewhere, the total number of particles being involved goes down – 32380 Lagrangian particles vs. 54096 Lagrangian particles – while fidelity to the underlying physics is maintained.

A comparison between the theoretical period with the period obtained from the simulation is shown in Fig. 3.13. The period can be determined by considering the integrated kinetic energy as a function of time. The kinetic energy is maximum when the shape is circular, at which point the surface energy is minimum, and is minimum when major and minor axis are switched and droplet becomes elliptical, at which point the surface energy is maximum. The theoretical period of oscillation is $t_p^\star = 3.63$. Fig. 3.13 shows a period of roughly $t^\star = 4$, which is close to the theoretical value. Such deviation is reasonable considering the viscous effect in the simulation. Cases with different particle number densities are also shown. Results show that the kinetic energy converges with increasing particle density, N_{pc}. The results from non-uniform particle number density agrees well with the uniform particle number density cases, showing that the LVOF approach is capable of capturing interfacial dynamics accurately when the clustering of particles is employed. Additionally, results using both kernel function W_1 and W_2 are also shown with the same particle number density. Using the polynomial kernel function W_1, the kinetic energy diverges after tiem $t^\star = 2$, while using the same particle number density and kernel function W_2 the result is stable. This suggests that the kernel function W_2, which allows for higher contribution of farther away, is less sensitive to the randomness in the LVOF field, and that function W_1 is more sensitive to particle randomness which leads to oscillatory surface tension forces and droplet instability.

3.3 Summary and conclusions

We have developed a Lagrangian volume of fluid (LVOF) approach for the simulation of multiphase flows. The LVOF approach transports the volume of fluid using variable particles per cell and is combined with a traditional Navier-Stokes solver to obtain the fluid and momentum fields. A weighted smoothed particle hydrodynamics (SPH) type

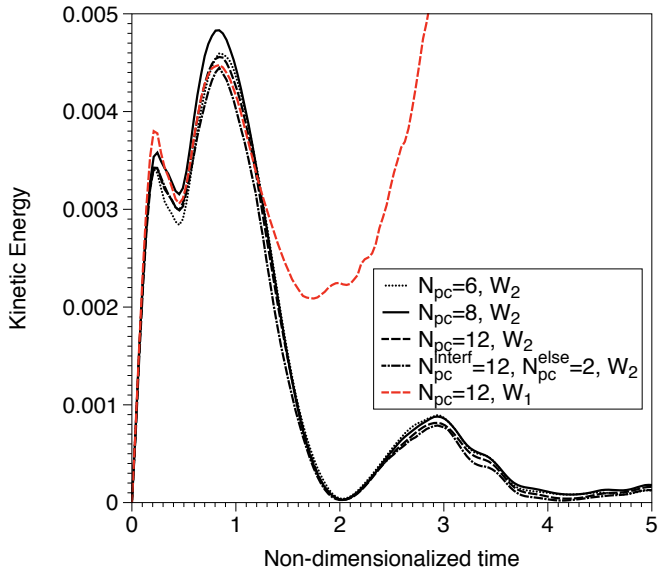

Figure 3.13: Droplet kinetic energy as a function of time.

formula for the color function is adopted to better describe the interfacial properties while reducing the computational cost using variable particle density. This is attractive in that variable particle density facilitates improved resolution when simulating turbulent flows.

The mathematical consistency has been demonstrated via comparison of interfacial quantities such as color function, normal vector and curvature using a uniform particle number density as well as variable particle number density. The traditional unweighted SPH creates large oscillations in all three interfacial quantities due to gradients of the particle number density near the interface. By contrast, the LVOF approach agrees well with the theoretically predicted values for interfacial quantities. Secondly, the classic problem of a rotating Zalesak disk is tested for various particle densities. The results show the expected result that the sharp corners are preserved after a full cycle, demonstrating that there is no diffusive or dispersive error in Lagrangian VOF approach. More importantly however, is the that the mean VOF is fairly independent of the number of particles in this simple test. In simulating an initially elliptical droplet, we demonstrate the coupled LVOF - Eulerian Navier-Stokes solver and it's ability to obtain a physically consistent result. We also demonstrate the superiority of a kernel function

that results in superior statistical accuracy when calculating the surface tension term.

Chapter 4

Probability density function approach for modeling of turbulent flows

Probability density function (PDF) characterize the scalar fluctuation, by solving the transport equation of the PDF. Source term based on scalar can all be calculated based on PDF. The advantage of PDF method is that the non-linear source term appears to be in closed form and does not need any subgrid modeling. Meanwhile, the PDF method is advantageous in handling variable density flow. Originally developed for Reynolds-averaged Navier-Stokes (RANS), the PDF method is further extended to filtered density function method (FDF) for LES.

The PDF transport equations are solved using a Lagrangian Monte Carlo method. The Lagrangian method is capable of avoiding any spurious numerical errors present in traditional Eulerian method and is diffusion free. The Lagrangian volume of fluid can remain sharp, preserving the information of the interface geometry. In contrast, the Eulerian VOF method induces large diffusion error. What's more, the well-known Gibbs phenomena will cause overshooting and undershooting at the jump location of VOF value in the Eulerian approaches, leading to non physical VOF values. In this chapter, the PDF approach is combined with LVOF approach to obtain the subgrid surface tension force, and is coupled with traditional LES to close the equation. This

approach does not require any subgrid scale modeling for the surface tension force, which is a highly non-linear term and difficult to model in LES. What's more, the approach is capable of providing a more accurate description for interfacial flow undergoing large deformation and topological changes compared to traditional Eulerian methods.

4.1 Formulation

4.1.1 Fluid transport

The flows under consideration are assumed to be incompressible, Newtonian, two phase flows. The phase is tracked by solving volume of fluid transport equation. The volume of fluid, ψ, satisfies $\psi = 0$ inside the gas and $\psi = 1$ inside the liquid. The primary transport variables are velocity $u_i(\mathbf{x}, t)$, pressure $p(\mathbf{x}, t)$ and volume of fluid ψ. The governing equations are the incompressible Navier-Stokes equations, given by

$$\frac{\partial u_j}{\partial x_j} = 0, \tag{4.1}$$

$$\frac{\partial \rho u_i}{\partial t} + \frac{\partial \rho u_i u_j}{\partial x_j} = -\frac{\partial p}{\partial x_i} + \frac{\partial \tau_{ij}}{\partial x_j} - F_i^s, \tag{4.2}$$

where τ_{ij} is the stress tensor. The fluid density ρ is written as a function of the VOF,

$$\rho = \psi\rho_l + (1 - \psi)\rho_g, \tag{4.3}$$

where ρ_l and ρ_g are the density of liquid and the density of gas. Similarly, the viscosity μ is written as

$$\mu = \psi\mu_l + (1 - \psi)\mu_g, \tag{4.4}$$

where μ_l and μ_g are the viscosity of liquid and the viscosity of gas. The term F_i^s is the component of the surface tension forces in the x_i direction. Using the continuum surface force model, the surface tension can be written as

$$F_i{}^s = \delta_s \sigma \kappa \hat{n}_i, \tag{4.5}$$

where σ is the surface tension coefficient, $\hat{n}_i$ is the unit normal vector, given by

$$\hat{n}_i = \frac{n_i}{\sqrt{n_j n_j}} \tag{4.6}$$

where the normal vector n_i is calculated by the gradient of the color function c,

$$n_i = \frac{\partial c}{\partial x_i} \tag{4.7}$$

The color function can be a smoothed version of the VOF, such that the gradient based on it can be calculated across the interfaces[71]. Inside the liquid, the color function is $c = 1$; while inside the gas, the color function is $c = 0$. Across the interface thickness, which should always have a fixed finite length, the color function varies smoothly from $c = 1$ to $c = 0$. The surface delta function δ_s is an approximation to the delta function with finite thickness that is non-zero at interfaces and decays to zero quickly away from interfaces. A choice of the surface delta function is

$$\delta_s = \sqrt{\frac{\partial c}{\partial x_i}\frac{\partial c}{\partial x_i}}. \tag{4.8}$$

The interface curvature, κ, is calculated from the divergence of the unit normal vector,

$$\kappa = \frac{\partial \hat{n}_i}{\partial x_i}. \tag{4.9}$$

Thus, the surface tension term can be expressed in terms of the color function, given by

$$F_i{}^s = \sigma \frac{\partial c}{\partial x_i}\frac{\partial}{\partial x_l}\left(\frac{\dfrac{\partial c}{\partial x_l}}{\sqrt{\dfrac{\partial c}{\partial x_j}\dfrac{\partial c}{\partial x_j}}}\right) \tag{4.10}$$

4.1.2 LES governing equations

The governing equations of the LES is obtained by filtering the level set transport equation and the incompressible Navier-Stokes equations. The filtering operation removes the small scale fluctuation, leaving only the large scale information. The filtering

operation on the function $f(\mathbf{x},t)$ can be represented by the convolution operation

$$\langle f(\mathbf{x},t)\rangle = \int_{-\infty}^{+\infty} f(\mathbf{x}',t)G(\mathbf{x}-\mathbf{x}')d\mathbf{x}', \tag{4.11}$$

where $\langle f(\mathbf{x},t)\rangle$ is the filtered quantity, G is the convolution kernel. The top-hat filter is one of the most frequently used filters, where G can be expressed as

$$G(\mathbf{x}-\mathbf{x}') = \begin{cases} 1/\overline{\Delta} & \text{if } |\mathbf{x}-\mathbf{x}'| \leq \overline{\Delta}/2 \\ 0 & \text{otherwise.} \end{cases} \tag{4.12}$$

This defines a filter width $\overline{\Delta}$ and take the averaged value within the filter width as the filtered value. The filtering operations are able to separate the small scale subgrid information from the large scale information.

Applying the filtering operation to the governing equations yields the LES governing equation, written as

$$\frac{\partial\langle u_j\rangle}{\partial x_j} = 0, \tag{4.13}$$

$$\frac{\partial\langle\rho\rangle\langle u_i\rangle}{\partial t} + \frac{\partial\langle\rho\rangle\langle u_i\rangle\langle u_j\rangle}{\partial x_j} = -\frac{\partial\langle p\rangle}{\partial x_i} + \langle\mu\rangle\frac{\partial^2\langle u_i\rangle}{\partial x_j\partial x_j} - \langle F^s\rangle - \frac{\partial\tau_{ij}}{\partial x_j} - \frac{\partial\tau_i^{\rho u}}{\partial t} - \frac{\partial\tau_{ij}^{\rho uu}}{\partial x_j} + \tau_{ij}^{\mu u}, \tag{4.14}$$

$$\frac{\partial\langle\psi\rangle}{\partial t} + \frac{\partial\langle u_j\rangle\langle\psi\rangle}{\partial x_j} = \frac{\partial\Psi_j}{\partial x_j}, \tag{4.15}$$

where $\langle F^s\rangle$ is the filtered surface tension term. Subgrid term τ_{ij} is the Reynolds stress given by

$$\tau_{ij} = \langle u_i u_j\rangle - \langle u_i\rangle\langle u_j\rangle. \tag{4.16}$$

The terms $\tau_i^{\rho u}$,$\tau_{ij}^{\rho uu}$,$\tau_{ij}^{\mu u}$ come from the temporal term, the convective term and the diffusive term, respectively:

$$\tau_i^{\rho u} = \langle\rho u_i\rangle - \langle\rho\rangle\langle u_i\rangle, \tag{4.17}$$

$$\tau_{ij}^{\rho uu} = \langle \rho u_i u_j \rangle - \langle \rho \rangle \langle u_i \rangle \langle u_j \rangle, \tag{4.18}$$

$$\tau_{ij}^{\mu u} = \langle \mu \frac{\partial^2 u_i}{\partial x_j \partial x_j} \rangle - \langle \mu \rangle \frac{\partial^2 \langle u_i \rangle}{\partial x_j \partial x_j}. \tag{4.19}$$

The SGS temporal term $\tau_i^{\rho u}$ reflects the effect of the density discontinuity across the interfaces on the time derivative term. This term increases with the increasing density ratio, and will become zero when the density ratio of two phases is one. Similarly, $\tau_{ij}^{\rho uu}$ comes from the effect of the density discontinuity on the convective terms, and $\tau_{ij}^{\mu u}$ comes from the effect of the viscosity discontinuity across the interfaces on the diffusive term. These three terms are only non-zero near the interfaces and will have a significant impact on the interfacial dynamics in the cases where the density ratio and the viscosity ratio are large. Ψ is the subgrid volume of fluid flux, given by

$$\Psi_j = \langle \psi u_j \rangle - \langle \psi \rangle \langle u_j \rangle. \tag{4.20}$$

4.1.3 Closure strategy

The subgrid terms $\tau_i^{\rho u}$,$\tau_{ij}^{\rho uu}$ reflects the density differences across the phase interfaces, while $\tau_{ij}^{\mu u}$ reflects the viscosity differences across the phase interfaces. For high Reynolds flow like sprays, the effect of viscosity differences can be small because the viscous forces are neglegible compared to the inertia forces. This would result in a much larger values of $\tau_i^{\rho u}$,$\tau_{ij}^{\rho uu}$ than $\tau_{ij}^{\mu u}$. For this work, we assume that the fluids in two phases have the same density and viscosity. In this case, the subgrid terms $\tau_i^{\rho u}$,$\tau_{ij}^{\rho uu}$, $\tau_{ij}^{\mu u}$ will be zero. The closure strategy of the filtered surface tension force term $\langle F^s \rangle$ will be discussed in the following sections. The Reynolds stress, τ_{ij}, is modeled via the eddy viscosity models, where the subgrid stress is given by

$$\tau_{ij} - (\delta_{ij})\tau_{kk} = -2\nu_l \langle S_{ij} \rangle_L \tag{4.21}$$

where the $\langle S_{ij} \rangle_L$ is the filtered strain rate tensor. The subgrid viscosity is $2\nu_l$. Two models are utilized in this work to model the subgrid viscosity. One is the Smagorinsky

model, given by

$$\nu_l = C_s \Delta_G^2 \sqrt{\langle S_{ij} \rangle_L \langle S_{ij} \rangle_L} \tag{4.22}$$

where C_s is a constant that ranges from $Cs = 0.01$ to $Cs = 0.1$. The filter size is Δ_G. The second model is the MKEV model, written as

$$\nu_l = C_k \Delta_G \sqrt{|\langle u_i^\star \rangle_L \langle u_i^\star \rangle_L - \langle \langle u_i^\star \rangle_L \rangle_{L'} \langle \langle u_i^\star \rangle_L \rangle_{L'}|} \tag{4.23}$$

where $u^\star = u_i - U_i$, and U_i is a characteristic velocity. The subscript L' represents a larger filter size than the L. Constant C_k ranges from $Ck = 0.01$ to $Ck = 0.1$.

4.1.4 Filtered density function

The filtered density function $P_L(\zeta; \mathbf{x}, \mathbf{t})$ is utilized to represent the scalar fluctuation of VOF function $\psi(\mathbf{x}, \mathbf{t})$ in a probablistic manner. The filtered density function $P_L(\zeta; \mathbf{x}, \mathbf{t})$ is defined as

$$P_L(\zeta; \mathbf{x}, t) = \int_{-\infty}^{+\infty} \varrho[\zeta, \psi(x', t)] G(\mathbf{x}' - \mathbf{x}) d\mathbf{x}' \tag{4.24}$$

where ϱ is the fine grained density, defined as

$$\varrho[\zeta, \psi(\mathbf{x}, t)] = \delta[\zeta - \psi(\mathbf{x}, t)]. \tag{4.25}$$

Equation (4.24) implies that the filtered density function is a filtered fine grained density.

For further development, it is useful to define the conditional filtered value of function $Q(\mathbf{x}, \mathbf{t})$, written as

$$\langle Q(\mathbf{x}, \mathbf{t}) | \psi \rangle_L \equiv \frac{\int_{-\infty}^{+\infty} Q(\mathbf{x}', t) \varrho[\psi, \psi(x', t)] G(\mathbf{x}' - \mathbf{x}) d\mathbf{x}'}{P_L(\zeta; \mathbf{x}, \mathbf{t})} \tag{4.26}$$

where $\langle \alpha | \beta \rangle |$ denotes the filtered value of α conditioned on β. The conditional filtered value satisfies

1.

$$\text{For } Q(\mathbf{x}, t) = c, \langle Q(\mathbf{x}, t) | \zeta \rangle_L = c \tag{4.27}$$

2.

$$\text{For } Q(\mathbf{x}, t) \equiv \hat{Q}(\psi(\mathbf{x}, t)), \langle Q(\mathbf{x}, t) | \zeta \rangle_L = \hat{Q}(\zeta) \tag{4.28}$$

3.

$$\langle Q(\mathbf{x},t)\rangle_L = \int_{-\infty}^{+\infty} \langle Q(\mathbf{x},t)|\zeta\rangle_L P_L(\zeta;\mathbf{x},t)d\zeta \tag{4.29}$$

where c is a constant, and $Q(\mathbf{x},t) \equiv \hat{Q}(\psi(\mathbf{x},t))$ denotes the case where the function $Q(\mathbf{x},t)$ can be completely described by the VOF, such as interface curvature and surface tension forces.

The FDF transport equation is obtained by taking derivative of Eq. (4.24), which gives

$$\frac{\partial P_L(\zeta;\mathbf{x},t)}{\partial t} = \int_{-\infty}^{+\infty} \frac{\partial \psi(\mathbf{x},t)}{\partial t}\frac{\partial \varrho[\zeta,\psi(\mathbf{x}',t)]}{\partial \zeta} \times G(\mathbf{x}'-\mathbf{x})d\mathbf{x}' \tag{4.30}$$

$$= -\frac{\partial}{\partial \zeta}\int_{-\infty}^{+\infty} \frac{\partial \psi(\mathbf{x},t)}{\partial t} \times \varrho[\zeta,\psi(\mathbf{x}',t)]G(\mathbf{x}'-\mathbf{x})d\mathbf{x}' \tag{4.31}$$

$$= -\frac{\partial}{\partial \zeta}[\langle \frac{\partial \psi}{\partial t}|\zeta\rangle_L P_L(\zeta;\mathbf{x},t)] \tag{4.32}$$

From Eq. (2.6), the temporal term can be expressed by the convective term, and the equation becomes

$$\frac{\partial P_L(\zeta;\mathbf{x},t)}{\partial t} = \frac{\partial}{\partial \zeta}[\langle \frac{\partial u_i \psi}{\partial x_i}|\zeta\rangle_L P_L(\zeta;\mathbf{x},t)] \tag{4.33}$$

$$= -\frac{\partial \langle u_i|\zeta\rangle_L P_L(\zeta;\mathbf{x},t))}{\partial x_i}. \tag{4.34}$$

Adopting the decomposition

$$\langle u_i|\zeta\rangle_L P_L(\zeta;\mathbf{x},t) = \langle u_i\rangle_L P_L(\zeta;\mathbf{x},t) + [\langle u_i|\psi\rangle_L - \langle u_i\rangle_L]P_L(\zeta;\mathbf{x},t) \tag{4.35}$$

and replaced the conditional filtered value of velocity with the filtered value of velocity, one can get

$$\frac{\partial P_L(\zeta;\mathbf{x},t)}{\partial t} + \frac{\partial \langle u_i\rangle_L P_L(\zeta;\mathbf{x},t)}{\partial x_i} = -\frac{\partial [\langle u_i|\psi\rangle_L - \langle u_i\rangle_L]P_L(\zeta;\mathbf{x},t)}{\partial x_i} \tag{4.36}$$

where the right hand side of the equation represents the subgrid convective flux and can

be modeled using the gradient-diffusion model, written as

$$[\langle u_i|\psi\rangle_L - \langle u_i\rangle_L]P_L(\zeta;\mathbf{x},t) = -\Gamma_l \frac{\partial P_L(\zeta;\mathbf{x},t)}{\partial x_j} \tag{4.37}$$

where Γ_l is the SGS diffusion coefficient, and can be calculated by

$$\Gamma_l = \nu_l / Sc_t \tag{4.38}$$

where Sc_t is the SGS Schmidt number and is assumed to be a constant.

4.1.5 Numerical method for PDF equation

The numerical solution of the system is obtained by first solving the flow field properties via the LES through numerically solving the Navier-Stokes equation. After that, the FDF transport equation of the VOF is solved using a Lagrangian Monte-Carlo method. The Lagrangian Monte-Carlo method utilizes an equivalent system of randomly distributed particles, and consider the motion of the pariticles govered by the Fokker Planck equation, written as

$$dX_i(t) = D_i(\mathbf{x}(t),t)dt + E^{\frac{1}{2}}(\mathbf{x}(t),t)dW_i(t) \tag{4.39}$$

where dX_i denotes the displacement in i direction within a time interval dt. $D_i(\mathbf{x}(t),t)$ is the drift vector, and $E(\mathbf{x}(t),t)$ is the diffusion coefficient and W_i represents the Wiener-Lévy process. The drift vector and diffusion coefficient satisfy

$$D_i \equiv \langle u_i\rangle_L + \frac{\partial \Gamma_l}{\partial x_i} \tag{4.40}$$

$$E \equiv 2\Gamma_l \tag{4.41}$$

The Fokker Planck equation represents an equivalent system of the transport of FDF. When solved numerically, the FDF is represented by a scalar $\phi(\mathbf{x},t)$ that is assigned to each particles. The location of particles is obtained through the numerical integration of Eq. 4.39.

$$X_i(t_{n+1}) = X_i(t_n) + D_i(t_n)\Delta t + (E(t_n)\Delta t)^{\frac{1}{2}}\xi_i(t_n) \tag{4.42}$$

where ξ_i is a random variable with standard Gaussian distribution. This scheme preserves the Markovian character of the diffusion process.

4.1.6 Lagrangian VOF

We propose a Lagrangian particle based approach that can close the filtered surface tension term $\langle \mathbf{F}^s \rangle$. This approach is based on the smoothed particle hydrodynamics (SPH) and is modified such that it is more suitable for the complex, multiphase turbulent flows. The SPH method utilizes a kernel function, or weight function, W, to approximate a function and its derivatives. The kernel function W is an approximation to delta function, but has a finite smoothing length h and satisfies

$$\lim_{h\to\infty} W(x,h) = \delta(x) \tag{4.43}$$

where $\delta(x)$ is the standard delta function. Multiple particles are seeded in each cell in both the gas and liquid phases, carrying the local FDF value, ϕ_i, which equals to the VOF value ψ_i. The particle approximation to the color function, c, is computed based on this FDF or VOF and is given by an weighted formula of Eq. 4.43

$$c_i = \frac{\sum_{j=1}^{N_p} W(|\mathbf{x}_j - \mathbf{x}_i|)\psi_j V_j}{\sum_{j=1}^{N_p} W(|\mathbf{x}_j - \mathbf{x}_i|)V_j}, \tag{4.44}$$

where N_p is the number of particles within the influence range, and ψ_i is the VOF on particle i. The surface tension for particle i, $\mathbf{F}_i$, is calculated on the interface particles via

$$\mathbf{F}_i = \delta_s \sigma \kappa_i \hat{\mathbf{n}}_i, \tag{4.45}$$

where the unit normal vector is given by $\hat{\mathbf{n}}_i = \mathbf{n}_i/|\mathbf{n}_i|$, and the particle normal vector $\mathbf{n}_i$ is calculated through the gradients of the color function,

$$\mathbf{n_i} = (\nabla c)_i = \sum_{\substack{j=1 \\ i\neq j}}^{N_p} \nabla W(|\mathbf{x}_j - \mathbf{x}_i|) c_j V_j. \tag{4.46}$$

In the summation, the particle i is excluded to avoid the situation in which the gradient of kernel function doesn't exist. The interface curvature, κ_i, is calculated using the divergence of the unit normal vector

$$\kappa_i = \nabla \cdot \hat{\mathbf{n}}_i = \sum_{\substack{j=1 \\ i \neq j}}^{N_p} \nabla W(|\mathbf{x}_j - \mathbf{x}_i|) \cdot \hat{\mathbf{n}}_j V_j. \tag{4.47}$$

Additional improvement in accuracy can be achieved by by replacing the function value inside the summation with the difference of the function between the nearby particles, which can reduce the particle inconsistency error in the derivative calculation. The improved equations are written as

$$\mathbf{n_i} = (\nabla c)_i = \sum_{\substack{j=1 \\ i \neq j}}^{N_p} \nabla W(|\mathbf{x}_j - \mathbf{x}_i|)(c_j - c_i) V_j, \tag{4.48}$$

$$\kappa_i = \nabla \cdot \hat{\mathbf{n}}_i = \sum_{\substack{j=1 \\ i \neq j}}^{N_p} \nabla W(|\mathbf{x}_j - \mathbf{x}_i|) \cdot (\hat{\mathbf{n}}_j - \hat{\mathbf{n}}_i) V_j, \tag{4.49}$$

and the delta function, δ_s, for particle i is given by $\delta_s = \lambda |\mathbf{n_i}|$, where λ is a constant. An additional filtering step on the unit normal vector proposed by [58] is adopted. The normal vectors are effectively "clipped" or set to a threshold value using

$$\tilde{\mathbf{n}}_i = \begin{cases} \mathbf{n}_i / |\mathbf{n}_i|, & \text{if} \quad |\mathbf{n}_i| > 0.01/h, \\ 0, & \text{otherwise.} \end{cases} \tag{4.50}$$

The clipping is needed because near the edge of the interfaces, the magnitude of normal vector will be small and error-prone. Thus, the unit normal vector calculated based on it will be oscillatory and not reliable for these particles.

The filtered surface tension term appearing in the Eulerian momentum equation is obtained by averaging the particle values inside the cell,

$$\langle \mathbf{F}^s \rangle = \frac{\sum_{i=1}^{N_{pc}} \mathbf{F}_i V_i}{\sum_{i=1}^{N_{pc}} V_i} = \frac{\sum_{i=1}^{N_{pc}} \delta_s \sigma \kappa_i \tilde{\mathbf{n}}_i V_i}{\sum_{i=1}^{N_{pc}} V_i}, \tag{4.51}$$

where N_{pc} is the number of particles in the cell. The result is an "SPH-like" formulation that utilizes the particle data only in the interfacial regions. The particles whose color functions lie in the range $0 < c_i < 1$ are marked as the interface particles, and the surface tension is calculated using only these particles.

4.2 Performance evaluation

4.2.1 SGS models for single phase flow

In order to find an optimal subgrid model for the Reynolds stress τ_{ij}, simulations for single phase turbulent flows are carried out, where the Reynolds stress is modeled by both the Smagorinsky model and the MKEV model. Resolution of both $64 \times 64 \times 64$ and $128 \times 128 \times 128$ are used and the average field and the instantaneous field are compared. Flow velocity in x direction is averaged in x-z plane at different instants in time for a temporally evolving jet, and changes of flow velocity versus y direction are plotted for each LES cases at different instants in time and are compared with DNS results.

Flow configuration

The flow under consideration consists of a three-dimensional single phase round jet of diameter D. The simulation is carried out in a temporal manner, with the reference frame attached to the shear layer of the spatially developing round jet. The density and viscosity of the interior and the exterior fluid are assumed to be the same. The surface tension is assumed to be zero. Initially, the interior fluid has a velocity of U_o, while the exterior fluid has a velocity of $-U_o$. The Reynolds number based on the jet diameter D, the velocity U_o and the viscosity μ, the density of the jet ρ_l is $Re_D = \rho_l U_o D/\mu = 3000$.

Numerical parameters

The computations are performed on a domain size of $4D \times 4D \times 4D$ in the x,y and z directions, respectively. A uniformly-spaced grid is utilized and two different resolutions are evaluated - $128 \times 128 \times 128$ and $64 \times 64 \times 64$. For the purposes of evaluation we also perform the DNS of the same flows utilizing a resolution of $512 \times 512 \times 512$. Random perturbations are added initially to the field to accelerate the breakup of the jet. The

Table 4.1: Parameters for single phase flow simulations

Case	Grid resolution	SGS model
1	$64 \times 64 \times 64$	Smagorinsky, Cs=0.01
2	$128 \times 128 \times 128$	Smagorinsky, Cs=0.01
3	$64 \times 64 \times 64$	MKEV, Ck=0.01
4	$128 \times 128 \times 128$	MKEV, Ck=0.01

numerical method used to solve the Navier-Stokes equation is a predictor-corrector based finite-difference method that is second order accurate in time and fourth order accurate in space[63]. Both the Smagorinsky model with $Cs = 0.01$ and the MKEV model with $Ck = 0.01$ are used to model the SGS Reynolds stress. Different simulation cases are listed in Table 4.1.

Results

Figure 4.1 shows the comparision between the results from the DNS and from the LES using the Smagorinsky model for the Reynolds stress term. The grid resolution is $64 \times 64 \times 64$. From the results of the DNS, it shows that initially at $t = 0$, the velocity is maximum at center where $y = 0$. As flow evolves, at $t = 3$, the velocity profile starts to expand outward in the y direction, and a local low value of the velocity shows up at the center near $y = 0$. As the flow evolves, the velocity decreases at center at $t = 6$, and develops into a bimodal shape where the peak value is reached near $y = \pm 0.6$. At $t = 9$, the velocity profile further spreads out, and center velocity further decreases, while the peak location moves further away from the center. With the Smagorinsky model, at $t = 3$, instead of having a local low value near $y = 0$, the velocity is still maximum at the center. At $t = 6$, the velocity at the center is lower than that of DNS, and the peak value at $y = \pm 0.6$ is higher than that of DNS. The velocity profile is less spread out than the DNS case. And similar thing happens at $t = 9$, where the bimodal peak is higher than the DNS case and the range of the profile is narrower than the DNS case. A similar trend can be observed in Fig. 4.2, where a higher resolution of $128 \times 128 \times 128$ is used with the Smagorinsky model for the Reynolds stress term. In comparison with the previous case with a lower resolution of $128 \times 128 \times 128$, the

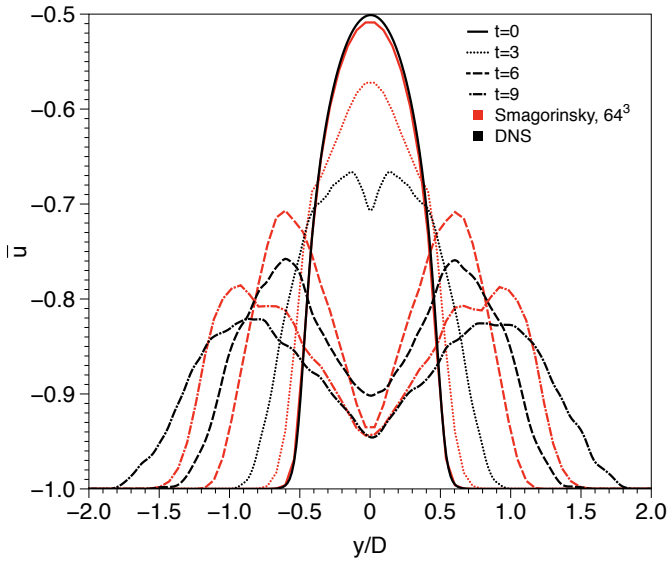

Figure 4.1: Averaged U velocity versus y. Using Smagorinsky model with Cs=0.01. Grid resolution is 64^3.

agreement of the velocity profile using the higher resolution is much better, suggesting that with higher resolution, more fluid are entrained due to the effect of the small scale turbulent mixing than using the lower resolution. However, at $t = 3$ the velocity is still maximum at the center instead of having a local minimum, and the velocity profile predicted from the LES is still narrower than that using the DNS. From these results, it is suggested that the Smagorinsky model tends to delay the transition from laminar to turbulent at the initial stage of the flow, and tends to underpredict the effect of turbulent mixing, especially at lower resolution, resulting in a lower entrainment effect from turbulent mixing.

Figure 4.3 shows the comparision between the results from the DNS and from the LES using the MKEV model for the Reynolds stress term. The grid resolution is $64 \times 64 \times 64$. At $t = 3$, it has a similar trend as using the Smagorinsky model, where instead of having a local low value at the center, the center velocity still has the highest value. As the flow evolves, at $t = 6$ and $t = 9$, the velocity profile agrees well with that from the DNS. Figure 4.4 shows results using the MKEV model and a higher resolution of $128 \times 128 \times 128$. At $t = 3$, a local low value in the velocity profile at the center $y = 0$ shows up in the LES result, and the agreement with the DNS at $t = 6$ and

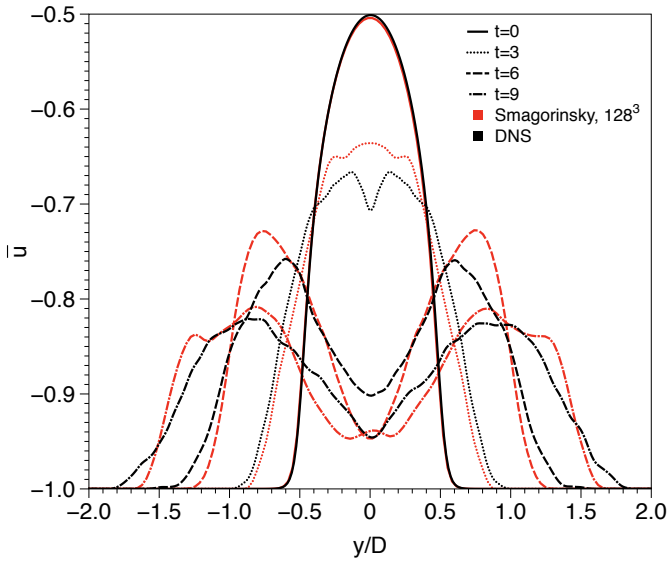

Figure 4.2: Averaged U velocity versus y. Using Smagorinsky model with Cs=0.01. Grid resolution is 128^3.

$t = 9$ is well. The results suggest that the MKEV model works better comparing to the Smagorinsky model at the initial transition stage from laminar to turbulent, where the Smagorinsky model tends to delay the transition. The MKEV model also works better than the Smagorinsky model after the flow becomes turbulent for the current situations, where the Smagorinsky model underpredict the turbulent mixing effect and consequently underpredict the flow entrainment, while MKEV model predicts a higher entrainment effect than the Smagorinsky model and agrees well with the DNS.

The instantaneous vorticity fields are shown in Fig. 4.5, where (a) shows the results from the DNS, (b) shows the results from the Smagorinsky model with a resolution of $128 \times 128 \times 128$, and (c) shows results from MKEV model with a resolution of $128 \times 128 \times 128$. The green surfaces shows the vorticity isosurface, and the color contour in the 2D plane shows the vorticity magnitudes. From the comparision, it shows that using the MKEV model, the instantaneous vorticity surfaces contain more small scale structures than using the Smagorinsky model. With the more small scale flow structures, it also implies higher turbulent effect and thus the higher mixing resulted from the small scales. Thus the MKEV model tends to predict higher turbulent mixing than the Smagorinsky model, which results in higher entrainment effect and better agreement

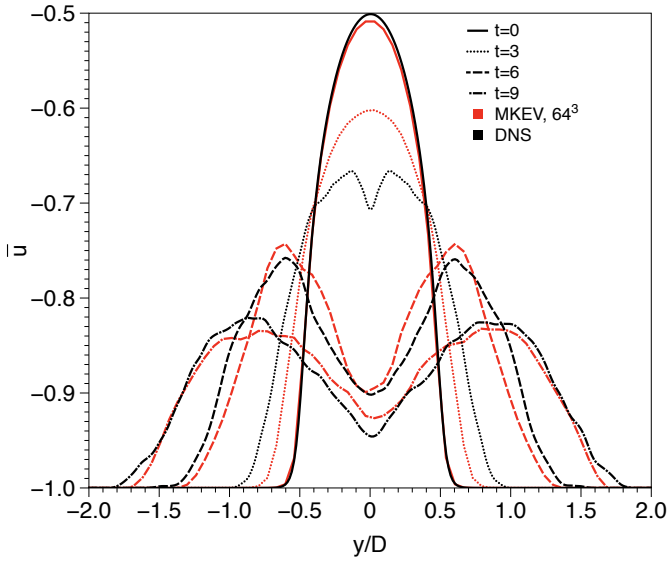

Figure 4.3: Averaged U velocity versus y. Using MKEV model with Ck=0.01. Grid resolution is 64^3

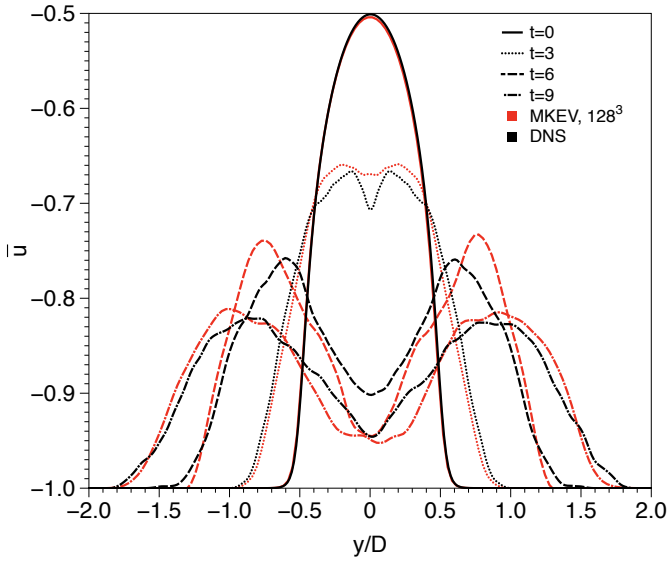

Figure 4.4: Averaged U velocity versus y. Using MKEV model with Ck=0.01. Grid resolution is 64^3

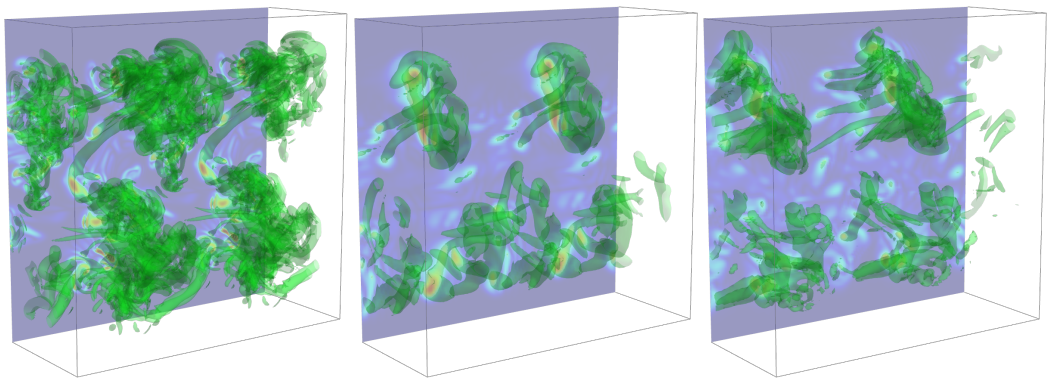

Figure 4.5: Comparision of vorticity isosurface between (a) DNS (b) LES with Smagorinsky model (c) LES with MKEV model. The green surfaces show vorticity isosurfaces, and the color contour in the color contour in the 2D plane shows the vorticity magnitudes.

with the DNS.

4.2.2 Lagrangian mixing models

In the Fokker Planck equation Eq. 4.39, the second term on the right hand side $E^{\frac{1}{2}}(\mathbf{x}(t),t)dW_i(t)$ represents the diffusion process of the Lagrangian particles. In the traditional PDF approaches, this diffusion term is modeled through a Gaussian mixing process, in which Lagrangian particles are moved randomly to other places following a Gaussin distribution. For multiphase interfacial flows, however, such model could cause problems because it mixes the Lagrangian particles from the liquid into the gas and the Lagrangian particles from the gas into the liquid randomly, while physically the two fluids are immiscible. Furthermore, the surface tension forces will restrain the random exchange of particles between different fluids. In order to look into the effect of the diffusion term, simulations with and without the mixing of particles are both carried out for a two phase flow without the present of surface tension force.

Table 4.2: Parameters for simulations with and without Lagrangian mixing term

Case	Particle number density	Lagrangian mixing
1	$Npc \approx 10$	With mixing
2	$Npc \approx 10$	Without mixing
3	$Npc \approx 26$	With mixing
4	$Npc \approx 26$	Without mixing

Flow configuration

The flow under consideration consists of a temporal three-dimensional (3D) round jet of diameter D. The interior fluid of the jet is assumed to be have a VOF value of $\psi = 1$, and the exterior fluid of the jet is assumed to have a VOF value of $\psi = 0$. The density and viscosity of the interior and the exterior fluid are assumed to be the same. The surface tension is assumed to be zero. Initially, the interior fluid has a velocity of U_o, while the exterior fluid has a velocity of $-U_o$. The Reynolds number based on the jet diameter D, the velocity U_o and the viscosity μ, the density of the jet ρ_l is $Re_D = \rho_l U_o D/\mu = 3000$.

Numerical parameters

The computations are performed on a domain size of $4D \times 4D \times 4D$ in the x,y and z directions, respectively. A uniformly-spaced grid is utilized and the grid resolution is $128 \times 128 \times 128$. Random perturbations are added initially to the field to accelerate the breakup of the jet. The numerical method used to solve the Navier-Stokes equation is a predictor-corrector based finite-difference method that is second order accurate in time and fourth order accurate in space[63]. THe MKEV model with $Ck = 0.01$ is used to model the SGS Reynolds stresses.

The Lagrangian particles initially are seeded uniformly in a cylindrical coordinate within a cylinder of radius of $r = 2$. Two particle seeding densities are tested, one with $Npc \approx 10$ and the other with $Npc \approx 26$. Both seeding densities are simulated with the diffusion term and without the diffusion term in the Fokker Planck equation. Simulation conditions for different simulation cases are listed in Table 4.2.

Results

Figure 4.6 shows the mean volume of fluid at x-z plane at three different instants of time as the temporal jet develops. A particle number density of $Npc \approx 10$ is used. The top row shows the result from the simulation with the mixing of particles, and the bottom row shows the result from the simulation without the mixing of particles. At $t = 2$, the mean volume fluid in the jet column has values below one in the top row, while without the mixing, at the bottom row the mean volume of fluid remains uniformly one inside the jet. This suggests that with the mixing added, the particles from the gas have mixed into the center liquid column, resulting in a mean volume of fluid less than one. The particles from the liquid region have also mixed into the gas, resulting in the regions with low non-zero volume of fluid around the jet. As the jet further breaks up at $t = 4$ and $t = 6$, the region containing the liquid is wider in the case with mixing than the case without mixing. The value of volume of fluid from case with mixing is very low in most regions, suggesting that these region contains very few liquid particles resulting from the random mixing effect from the diffusion term. Figure 4.7 shows the mean volume of fluid at y-z plane at the corresponding time and conditions in previous figure. The top row shows the case with the mixing and the bottom row shows the case without the mixing. The figure further demonstrates that the diffusion term creates a large amount of random mixing and create large regions with low mean volume of fluid value in gas regions.

Figure 4.8 and Fig. 4.9 shows the mean volume of fluid at the x-z plane and the y-z plane respectively, at a higher particle number density where $Npc \approx 26$. Similar difference between the mixing and no mixing results are observed as in the lower particle number density case. Comparing the differences between the case with $Npc \approx 10$ and the case with $Npc \approx 26$, it shows that the higher particle number density case creates a much smoother and less oscillatary mean VOF field for the case with the mixing, while the change of the particle number density has less influence on the results for the case without the mixing. This is because with the random displacement of particles, the higher number of particles will lead to higher statistical accuracy. However, even at the higher particle number density case, the mixing term still leads to a mean VOF below one in the liquid region and non-zero mean VOF in gas region, which is not physically true for two immiscible fluids. It is also interesting to note that increasing the particle

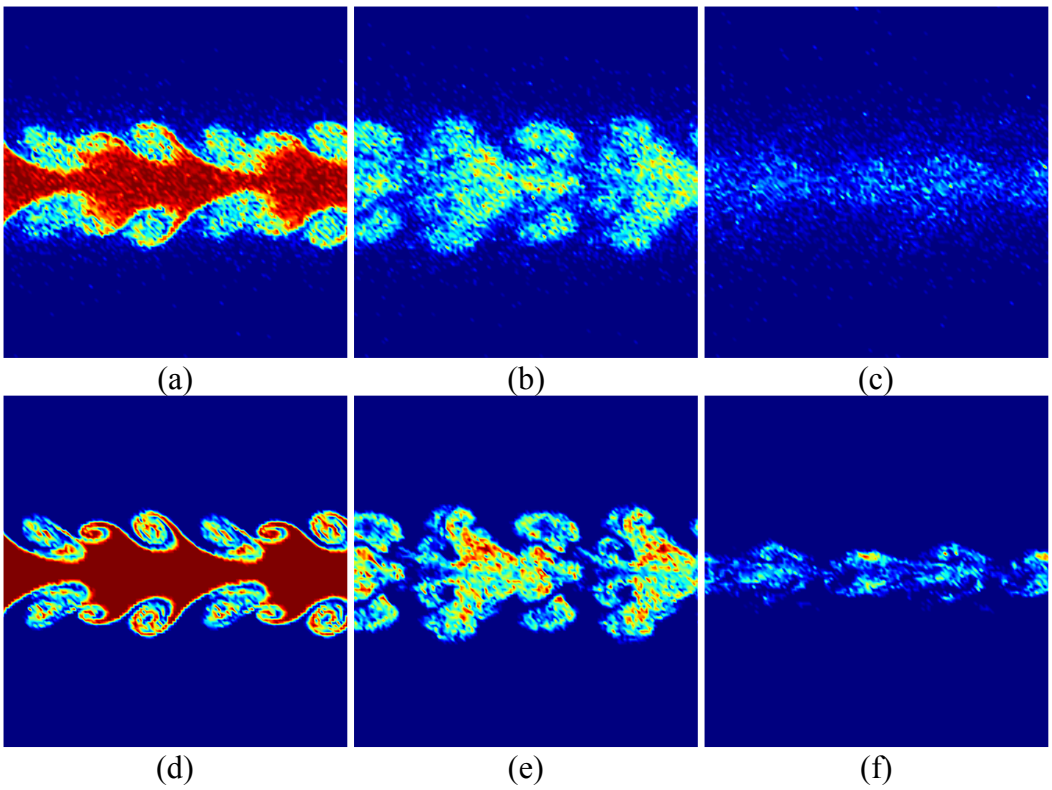

Figure 4.6: Mean volume of fluid on x-z plane. Red indicates VOF of 1. Blue indicates VOF of 0. Top row is with Lagrangian mixing term, (a) t=2, (b) t=4, (c) t=6. Bottom row is without Lagrangian mixing term, (a) t=2, (b) t=4, (c) t=6. Particle number density is $Npc \approx 10$.

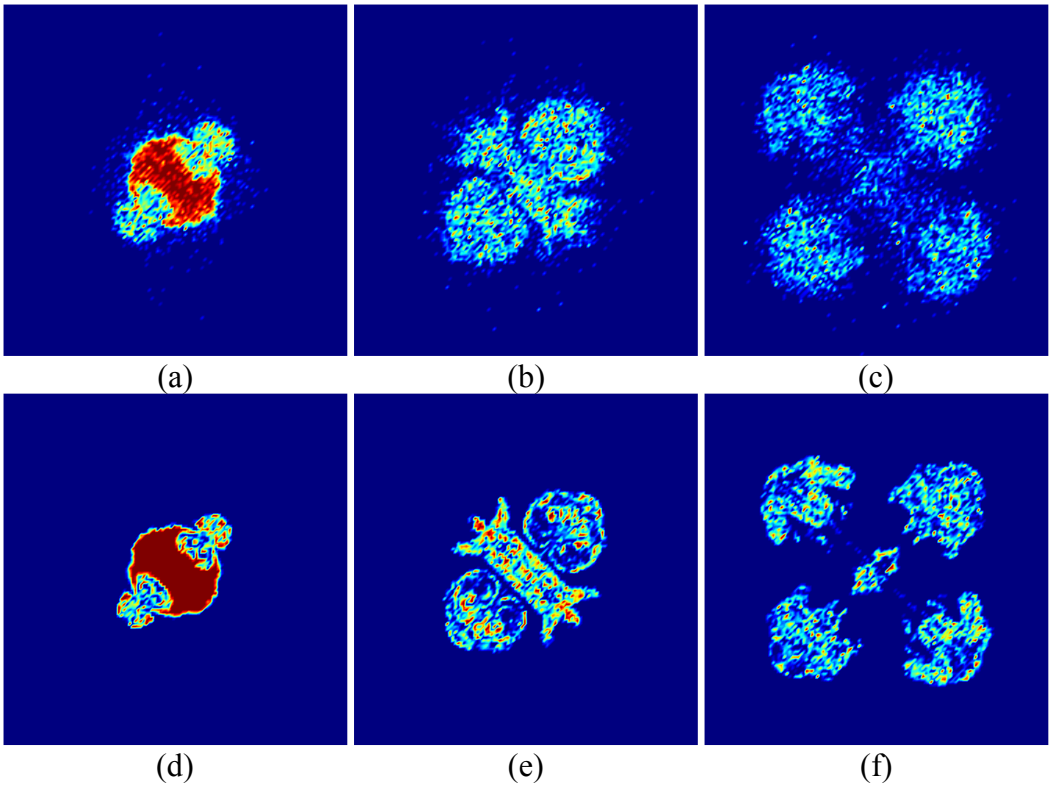

Figure 4.7: Mean volume of fluid on y-z plane. Red indicates VOF of 1. Blue indicates VOF of 0. Top row is with Lagrangian mixing term, (a) t=2, (b) t=4, (c) t=6. Bottom row is without Lagrangian mixing term, (a) t=2, (b) t=4, (c) t=6. Particle number density is $Npc \approx 10$.

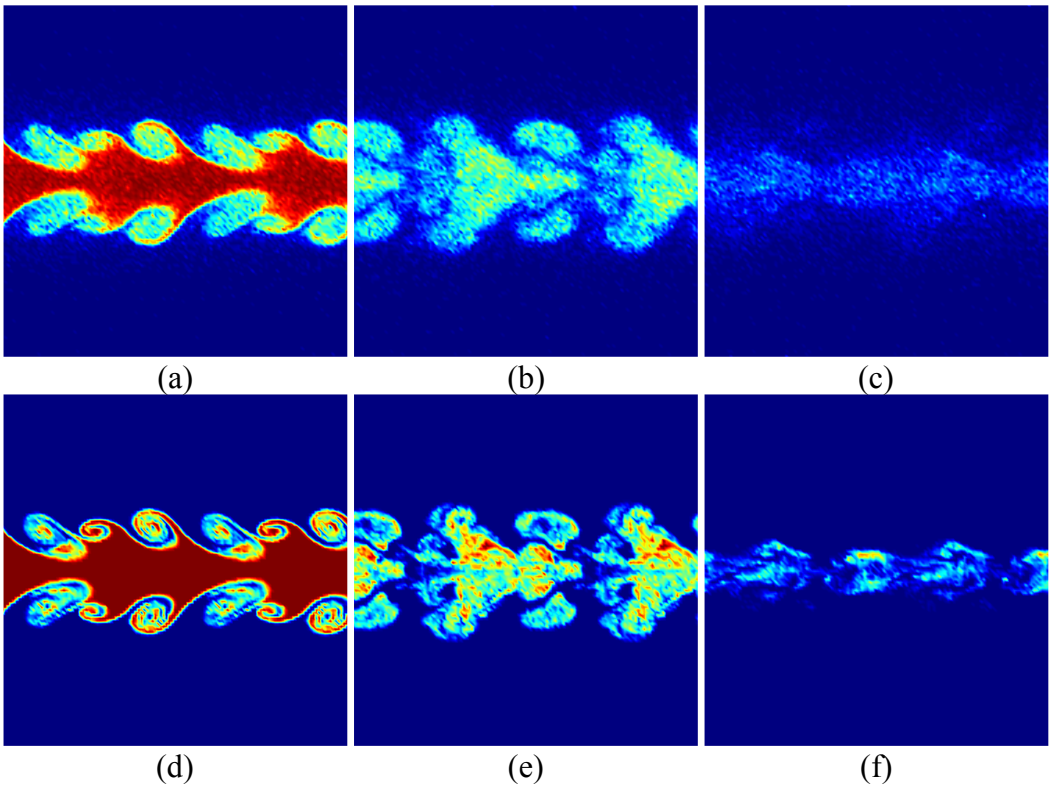

Figure 4.8: Mean volume of fluid on x-z plane. Red indicates VOF of 1. Blue indicates VOF of 0. Top row is with Lagrangian mixing term, (a) t=2, (b) t=4, (c) t=6. Bottom row is without Lagrangian mixing term, (a) t=2, (b) t=4, (c) t=6. Particle number density is $Npc \approx 26$.

number density from $Npc \approx 10$ to $Npc \approx 26$ causes more changes in the results with mixing than in the results without mixing. This suggests that results with the mixing are more particle number density dependent, and very high particle number density might be needed to achieve the convergence of the results.

4.2.3 Simulation of multiphase interfacial flows

In the previous sections, we have looked into the single phase SGS model for the Reynolds stress, and tested the cases with and without the Lagrangian mixing added in the Fokker Planck equation for a flow without surface tension force. In this section,

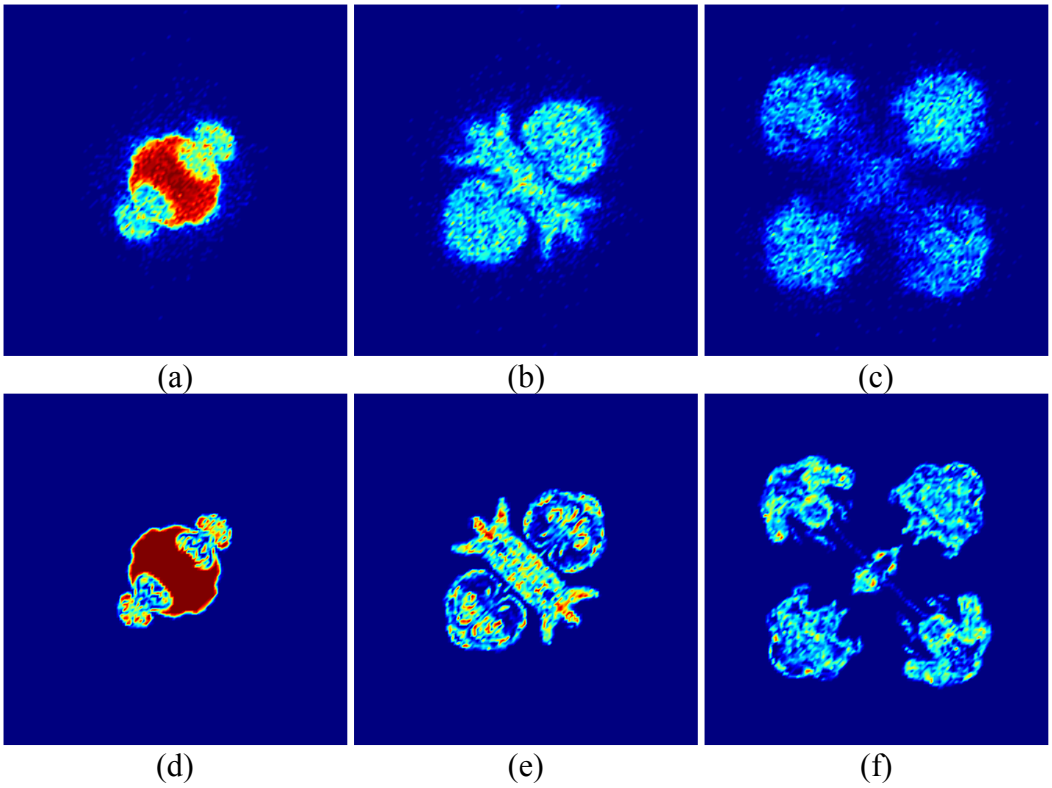

Figure 4.9: Mean volume of fluid on y-z plane. Red indicates VOF of 1. Blue indicates VOF of 0. Top row is with Lagrangian mixing term, (a) t=2, (b) t=4, (c) t=6. Bottom row is without Lagrangian mixing term, (a) t=2, (b) t=4, (c) t=6. Particle number density is $Npc \approx 26$.

the simulation of a multiphase interfacial flow is by large eddy simulation. The PDF approach is used to solve the transport of the volume of fluid. The surface tension source term is calculated based on PDF, it thus appears in closed form and does not need any subgrid modeling. The LVOF approach is used to calculate the surface tension source term based on Lagrangian VOF particles using the continuum surface force (CSF) model. In this section, the MKEV model with $Ck = 0.01$ is adopted to model the Reynolds stress, and no Lagrangian mixing is added. Simulations are carried out under different Weber numbers. The idea is to see if the particle based surface tension force in the LES approach is able to predict the trend of flow correctly. Both averaged flow field and the instantaneous flow field are looked into. A preliminary comparison between the LES and the DNS is also carried out.

Flow configuration

The flow under consideration consists of a three-dimensional (3D) round jet of diameter D. The interior fluid of the jet is assumed to be liquid with a VOF value of $\psi = 1$, and the exterior fluid of the jet is assumed to be gas with a VOF value of $\psi = 0$. The density and viscosity of the interior and the exterior fluid are assumed to be the same. The simulation is carried out in a temporal manner, with the reference frame attached to the shear layer of a spatially developing round jet. Initially, the interior fluid has a velocity of U_o, while the exterior fluid has a velocity of $-U_o$. The Reynolds number based on the jet diameter D, the velocity U_o and the viscosity μ, the density of the jet ρ_l is $Re_D = \rho_l U_o D/\mu = 3000$. The surface tension cofficient is σ, and the Weber number based on the jet diameter is $We_D = \rho_l U_o^2/\sigma$.

Numerical specifications

The computations are performed on a domain size of $4D \times 4D \times 4D$ in the x,y and z directions, respectively. A uniformly-spaced grid is utilized and a resolution of $128 \times 128 \times 128$ is used. Random perturbations are added initially to the field to accelerate the breakup of the jet. The numerical method used to solve the Navier-Stokes equation is a predictor-corrector based finite-difference method that is second order accurate in time and fourth order accurate in space[63].

Table 4.3: Parameters for multiphase flow simulation under different Weber numbers

Case	Particle number density	Weber number
1	$Npc \approx 10$	$We = 10$
2	$Npc \approx 10$	$We = 100$
3	$Npc \approx 10$	$We = 1000$
4	$Npc \approx 10$	$We = 10^6$

The fluid phase is obtained via the solution of the FDF-LVOF approach. The particles are seeded uniformly in a cylindrical coordinate with in a cylinder of $r = 2$. Particle number density is $Npc \approx 10$. Parameters for simulation is listed in Table 4.3. An exponential weight function is adopted:

$$W_2(r) = A \begin{cases} e^{-c\frac{r}{r_e}} - e^{-c}, & r < r_e, \\ 0, & \text{otherwise}, \end{cases} \tag{4.52}$$

Where A is the normalization factor, defined as

$$A = (4\pi r_e^3[\frac{2}{c^3} - (\frac{1}{c} + \frac{2}{c^2} + \frac{2}{c^3} + \frac{1}{3})e^{-c}])^{-1} \tag{4.53}$$

for 3D problem. The constant c may be used to adjust the shape of the spike function, as c increases, the particles close to the center will have more weight while the particles farther away will be weighted less. Here, we choose $c = 0.01$. And r_e is the influence radius. Within the influence radius r_e, particles can interact with each other, and the influence decreases as the distance between two particles increases. The influence radius r_e is defined based on the grid spacing as $r_e = n_g \Delta x$, where Δx is the grid spacing. In this work we set the influence radius to $r_e = 2\Delta x$.

Results

The LVOF approach is used to calculate the surface tension force at the interfaces. The color function, normal vector and curvature are all calculated based on particle values. Figure 4.10 demonstrates the normal vector calculated for the 3D phase interfaces. The green surface represents the phase interface. Figure on the right shows the zoomed-in

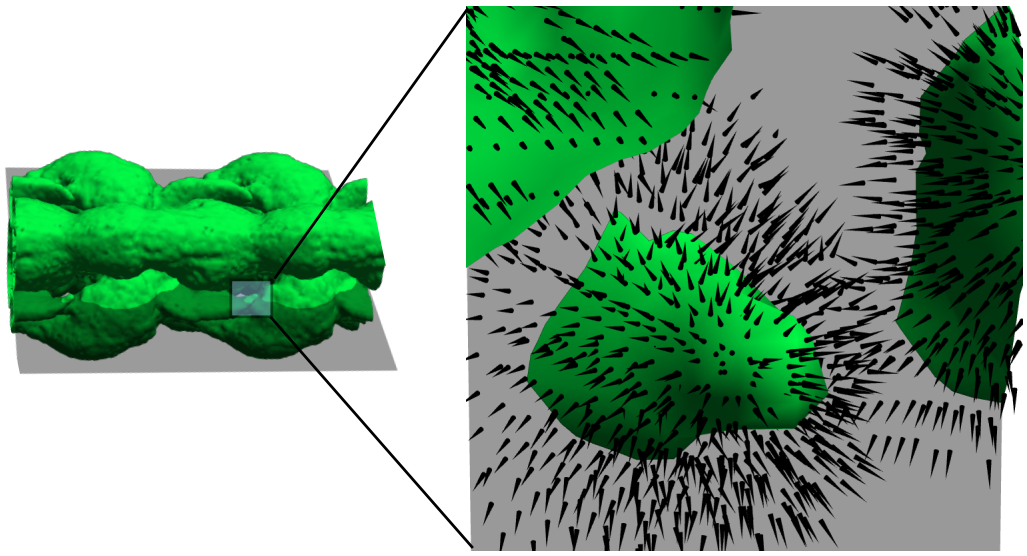

Figure 4.10: Close up view of 3D normal vector of jet at jet interface. Green surface represents jet interface, Black cones shows normal vector, where the tip of the cone is pointing in the direction of the normal vector.

interface, where the black cones shows the normal vector calculated using the LVOF approach, and the tip of the cone is pointing in the direction of normal vector. From the figure it shows that the normal vector is pointing in the outward direction of the interface. For a small interfacial structures shown, the accuracy of the normal vector is good for the given particle number density.

Figure 4.11 shows the profile of the averaged u velocity under four different Weber numbers. As the Weber number increases from $We = 10$ to $We = 10^6$, the inertial forces become more dominant than the surface tension forces. In Figure 4.11 (a), Weber number is $We = 10$. as the flow evolves in time, the velocity profile expands in the y direction by a little. However, the peak velocity still occurs at $y = 0$. In Figure 4.11 (a) where the Weber number is $We = 100$, the velocity profile expands wider in the y direction as the time evolves and develops into a bimodal distribution, and the peak happens at $y = \pm 0.7$ at $t = 6$. At Weber number of $We = 1000$, the bimodal distribution develops earlier at $t = 4$, and at $t = 6$ the peak velocity happens at around $y = \pm 0.8$. At an even higher Weber number of $We = 10^6$, the peak velocity happens at around $y = \pm 0.9$. A comparision of averaged velocity profile at $t = 6$ is shown in

Fig. 4.12. From the comparision, it shows that when the Weber number is small, a single-peak distribution is developed and less fluid outside of the jet is entrained. As Weber number increases from $We = 100$ to $We = 1000$, more fluid outside of the jet is entrained and the location of the peak velocity moves outwards. At $We = 10^6$, the distribution does not differ much from the $We = 1000$, suggesting that the effect of the surface tension is small and does not affect much on the averaged flow field. The results suggest that as the influence of the surface tension forces become larger, i.e. the Weber number becomes smaller, the breakup of the jet and expansion in the outward direction is supressed. This is because in a general way, surface tension forces act on the interface of the jet and push the jet in the inward direction, thus it will act to stablize the jet.

Figure 4.13 shows the instantaneous interfaces of the jet represented by the mean color function of $c = 0.4$ at Weber number of $We = 100$. At $t = 0$, the jet has a smooth cylindrical shape. At $t = 2$, disturbances start to show up at interfaces and cause deformations. At $t = 4$, the jet expands and further breaks up into smaller interfacial structures at $t = 6$. Figure 4.14 shows the instataneous jet interface at Weber number of $We = 1000$. The jet undergoes deformations at $t = 2$, expands at $t = 4$ and further breaks up at $t = 6$. From the comparison between Fig. 4.13 and Fig. 4.13, it shows that at the higher Weber number of $We = 1000$, there appears to be more small scale interfacial structures and droplets. This is especially evidential at $t = 6$. The fact that the smaller interfacial structures or droplets are formed as the flow rate (or Weber number) increases can be explained in an analogy to the concept of the smaller scales in turbulent flows with increasing Reynolds numbers. In the turbulent flows, the smallest scale is the size of the smallest eddy. The larger eddies are unstable and will break into smaller eddies. These small eddies might further break into smaller ones. At a certain size, the eddy becomes stable due to the balance between viscous and inertial forces. This smallest size is determined by the Reynolds number, since Reynolds number characterizes the ratio of the inertial force and the viscous force. In interfacial flow dominated by Weber number, the larger interfacial structures are unstable and will breakup into droplets or secondary structures. Until a small enough surface is generated such that the surface tension force overcomes the inertial force, the unstable interface continues to break up to generate smaller and smaller droplets. The larger the Weber number, the smaller the droplet size.

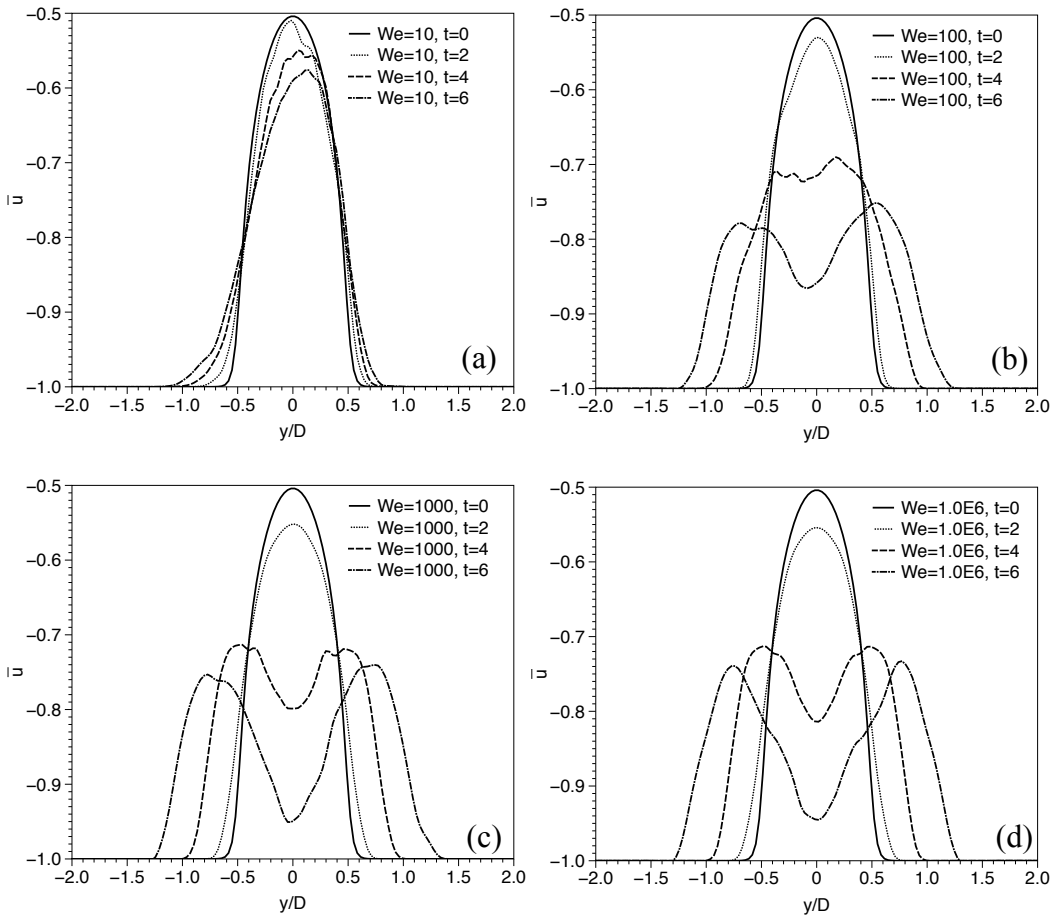

Figure 4.11: Averaged u velocity profile at different Weber numbers. (a) $We = 10$, (b) $We = 100$, (c) $We = 1000$, (d) $We = 10^6$.

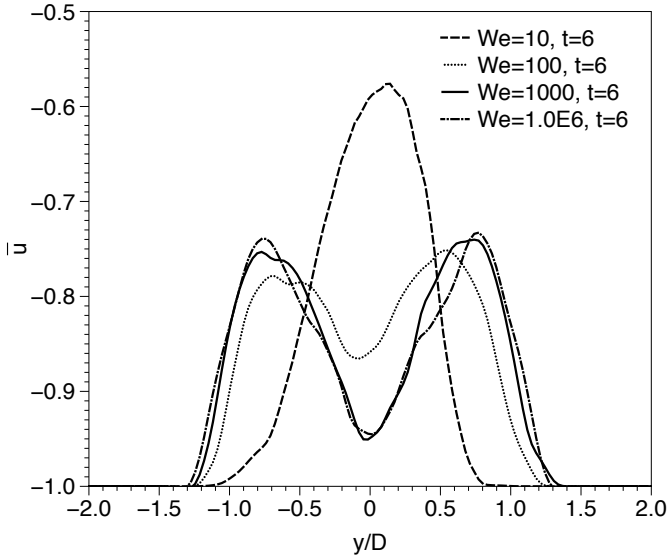

Figure 4.12: Comparison of averaged u velocity profile at different Weber numbers at $t = 6$.

A preliminary comparision between LES and DNS at $We = 1000$ is shown in Fig. 4.15. At $t = 2$, the agreement between DNS and LES is good and the velocity profile expands in y direction. At $t = 4$, both LES and DNS predict a bimodal distribution. While in DNS, the peak velocity occurs at $y = \pm 0.5$. In LES, the peak velocity occurs at around $y = \pm 0.4$. The peak velocity in LES is slightly larger than that in DNS. At $t = 6$, the peak velocity are similar in both LES and DNS. The peak velocity occurs at around $y = \pm 0.8$ in DNS, while it occurs at around $y = \pm 0.6$ in LES. This suggest in LES the surface tension force has a more suppressing effect on the breakup of the jet, which results in a narrower velocity profile and less entrainment of the exterior fluids. Future study will be focused on more detailed and qualitative comparision between DNS and LES.

4.3 Conclusions

In this chapter, we proposed a filtered density function (FDF) methodology combined with volume of fluid for simulation of multiphase turbulent flows. The probability density function approach is used to solve the volume of fluid transport, while the large

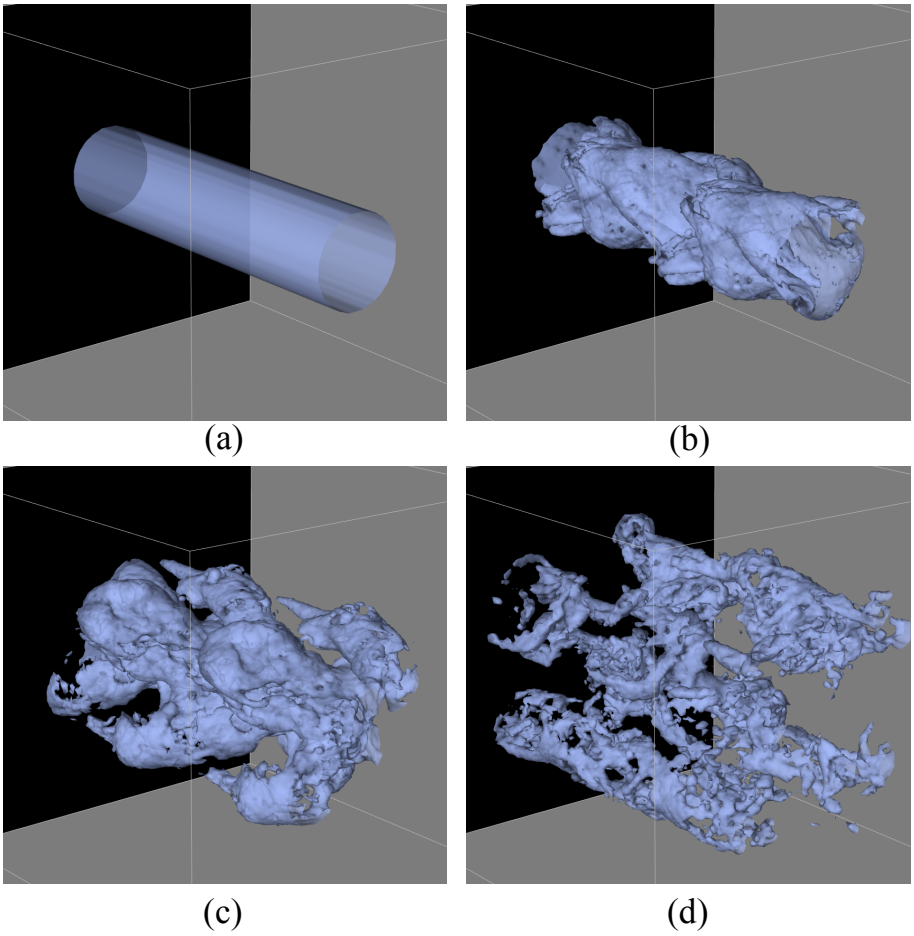

Figure 4.13: Time sequence shows the jet interfaces at Weber number of $We = 100$. (a) $t = 0$, (b) $t = 2$, (c) $t = 4$, (d) $t = 6$.

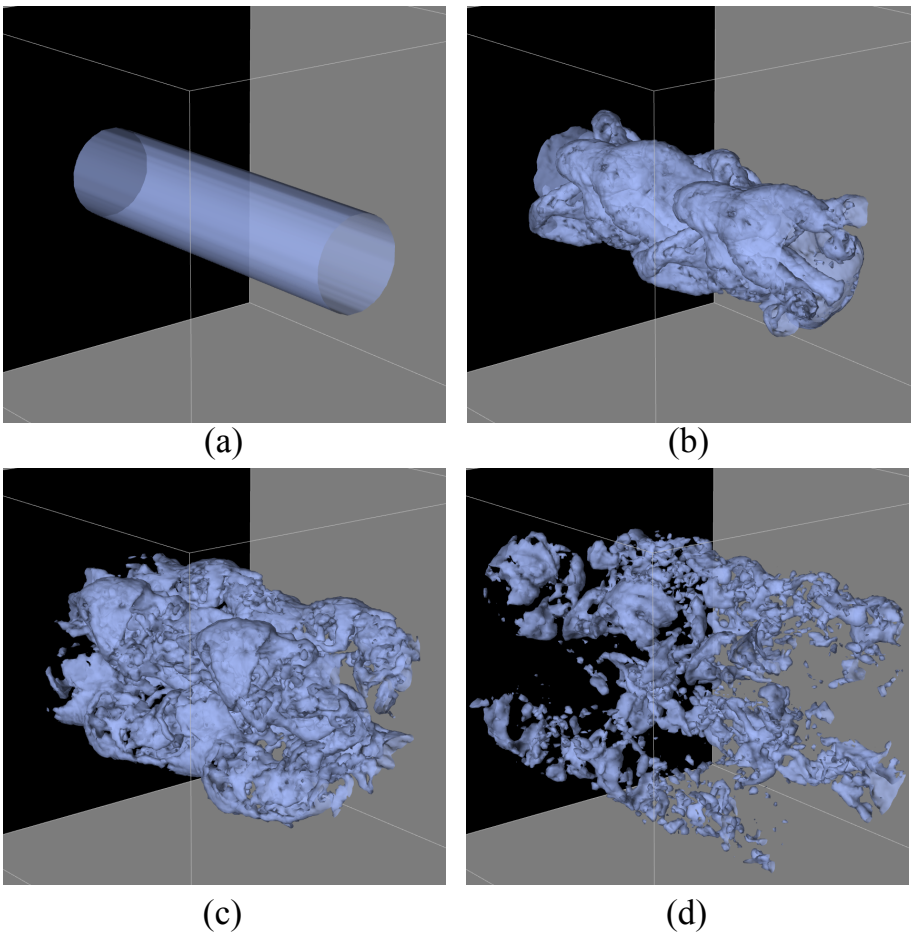

Figure 4.14: Time sequence shows the jet interfaces at Weber number of $We = 1000$. (a) $t = 0$, (b) $t = 2$, (c) $t = 4$, (d) $t = 6$.

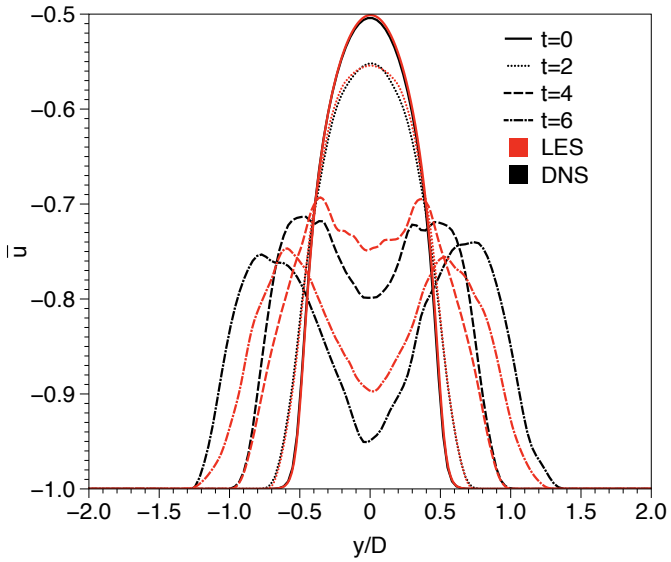

Figure 4.15: Comparison of averaged u velocity profile between DNS and LES at $t = 6$.

eddy simulation is used to solve for the flow field through the Navier-Stokes equation. Surface tension source term in the momentum equation is calculated based on the PDF, thus it appears in closed form and does not need any modeling. The PDF equation is solved through a Lagrangian Monte Carlo method, and the surface tension force is calculated based on Lagrangian particles. A Lagrangin volume of fluid (LVOF) approach is adopted, which is capable of calculating gradient based on particle values, without the need to take differential operations.

In order to choose the proper SGS model for the Reynolds stress, we first carry out the single phase LES with different SGS models. Smagorinsky model and MKEV model are tested, and it was found that the MKEV model has better performance than the Smagorinsky model in current case, in that Smagorinsky model tends to underpredict the turbulent mixing and the flow entrainment. Next, we test the effect of the diffusion term in the Lagrangian governing equations for the particle motion. It was found out that the current model for the diffusion term leads to the artificial mixing of the gas Lagrangian particles into the liquid region and the liquid Lagrangian particles into the gas region, which is not physical since the two fluids are immisicble. Next, the simulation is performed for the multiphase turbulent flows. The idea is to see if our proposed LES

approach can correctly predict the trend of the flow field with changing Weber number with the Lagrangian surface tension model. It is found out that with increasing Weber number, which corresponds to a smaller surface tension force compared to the inertial force, the mean velocity profile expands wider outwards. This shows that the surface tension force acts to suppress the breakup and spreading of the jet in a general way. The instantaneous flow field is also looked into, and it is found that more small scale structures and droplets are formed with higher Weber numbers, which agrees well with theory. A preliminary comparison between LES and DNS is also carried out, and the mean velocity profile is compared between the two.

Chapter 5

Conclusion and Discussion

In this research, we proposed a probability density function based methodology for the large eddy simulation of the multiphase turbulent flows. In order to achieve the goal, we have divided the research into the three stages. First, the direct numerical simulations for the multiphase turbulent flows are carried out. The physical mechanisms of the jet breakup and droplet formation are looked into, and the subgrid analysis is carried out on the governing equations and the DNS data. A temporal approach is shown to be capable of saving the computational cost by at least ten times. The interactions between the vorticity and jet breakup process are looked into, and two different breakup mechanisms – ligament pinch-off and sheet breakup – are identified. Similar breakup phenomena are observed in experiments, demonstrating the capability of the numerical tools to correct capture the interfacial dynamics. The subgrid analysis are carried out based on the DNS data. It was found out that the resulting SGS surface tension force is a highly non-linear term of the scalar. What's more, the SGS surface tension contains both positive and negative components, acting to both accelerate the breakup and supress the breakup. Results suggest that the SGS surface tension term can be difficult to model, while it can have a significant influence on small scale interfacial structures because of the local high Weber number for small scales.

Next, we looked into the possibility of establishing the probability density function approach for the simulation of the multiphase turbulent flows. The PDF transport equation is solved through the Lagrangian Monte Carlo method. The difficult step is to find a way to calculate the surface tension forces based on Lagrangian particles, because

the differential operations cannot be applied directly to particles to obtain the derivatives that show up in the surface tension term. We established a Lagrangion volume of fluid (LVOF) approach. In this approach, a weighted smoothed particle hydrodynamics (SPH) type formula is adopted, and the differential operations on particles are transferred into the derivative of kernel functions, which can be calculated analytically. We demonstrated the mathematical consistency by carrying out the test cases and simulated the oscillation of an elliptical droplet, and the agreement with the theory is well.

Finally, we proposed the probability density function approach for the simulation of the multiphase turbulent flows. We proposed combining the filtered density function (FDF) methodology combined with the volume of fluid for simulation to track the evolution of the phases. The probability density function approach is used to solve the volume of fluid transport, while the large eddy simulation is used to solve for the flow field through the Navier-Stokes equation. Surface tension source term in the momentum equation is calculated based on the PDF using the LVOF approach, which appears in closed form and does not need any modeling. We carried out single phase LES study to choose the proper SGS models for the Reynolds stresses, and we evaluated the effect of the diffusion term in the particle transport equation. After that, the simulations are carried out for the multiphase turbulent flows. Results show that larger Weber numbers tend to create more small scale interfacial structures and accelerate the breakup of the jet, which agrees well with theory. A preliminary comparison between LES and DNS is also carried out.

Our study shows that the filtered density function based approach can be a promising method, in that it models the flow with reduced computational cost than DNS, yet accurately in a model-free manor. There are still many challenges and future work will be focused on the following aspects.

- In the LVOF method, because of the need to search nearby particles, the number of operations is on the order of N^2 where N is the number of particles, and it is $N \log(N)$ at best if linked cell algorithms are employed ([72]). Thus, the computational cost to calculate the surface tension force is high. Alternate ways to speed up the neighboring search of particles are needed for efficient computing and implementation of the method.

- The employed Lagrangian mixing model for the diffusion term does not work well because it mixes the Lagrangian particles between two phases, while two fluids are immiscible and the surface tension force will prohibit such kind of mixing. Different mixing models are needed in order to correctly predict the diffusion effect in the particle transport process.

- Particle number density might have influences on the results. Increasing particle number density will increase the statistical accuracy, while it can increase the computational cost significantly. When particle number density is low, the decreased accuracy will make the calculation of surface tension force error-prone. A thorough particle number density study is needed in order to make sure that the resulting interfacial dynamics and droplet field converge with the particle number density.

- In our research, we have not looked into the SGS terms resulted from the density and viscosity differences between two phases. While SGS term resulted from viscosity gradient might be insignificant in a high Reynolds number flow like spray, the SGS term resulted from the density gradient might be significant for the inertial dominant flow. Future study is needed to look into the modeling of these terms.

- A thorough comparison between the LES and DNS results is needed for validation of the LES tools. Preliminary comparison shows that the breakup is supressed in LES compared to DNS. In this case, a 3D calibration factor might be needed such that the calculated surface tension force is correct. Further comparision of spray characteristics such as droplet size distribution are also needed.

References

[1] C. Dumouchel. On the Experimental Investigation on Primary Atomization of Liquid Streams. *Exp. Fluids*, 45(3):371–422, 2008.

[2] R.D. Reitz and R. Diwakar. Structure of high-pressure fuel sprays. Technical report, Fluid Mechanics Dept., GM Research Labs., Warren, MI, 1987.

[3] R.P. Mun, B.W. Young, and D.V. Boger. Atomisation of dilute polymer solutions in agricultural spray nozzles. *J. Non-Newton. Fluid*, 83(1-2):163–178, 1999.

[4] M.A. Patterson and R.D. Reitz. Modeling the effects of fuel spray characteristics on diesel engine combustion and emissions. *SAE transactions*, 107(3):27–43, 1998.

[5] R. Vehring. Pharmaceutical Particle Engineering via Spray Drying. *Pharmaceutical Research*, 25(5):999–1022, November 2007.

[6] H. Hiroyasu, T. Kadota, and M. Arai. Development and use of a spray combustion modeling to predict diesel engine efficiency and pollutant emissions: Part 1 combustion modeling. *Bulletin of JSME*, 26(214):569–575, 1983.

[7] H. Ganzelmeier, D. Rautmann, R. Spangenberg, M. Streloke, M. Herrmann, H.J. Wenzelburger, and Dr H.F. Walter. *Studies on the spray drift of plant protection products: results of a test program carried out throughout the Federal Republic of Germany*. Blackwell Wissenschafts-Verlag, 1995.

[8] B.J. de Gans, P.C. Duineveld, and U.S. Schubert. Inkjet printing of polymers: state of the art and future developments. *Advanced materials*, 16(3):203–213, 2004.

[9] S.P. Lin and D.J. Kang. Atomization of a liquid jet. *Phys. Fluids*, 30(7):2000–2006, 1987.

[10] M. Salyani and R.P. Cromwell. Spray drift from ground and aerial applications. *Transactions of the ASAE*, 35(4):1113–1120, 1992.

[11] Lord Rayleigh. On the capillary phenomena of jets. *Proceedings of the Royal Society of London*, 29(196-199):71–97, 1879.

[12] R.P. Grant and S. Middleman. Newtonian jet stability. *AIChE J.*, 12(4):669–678, 1966.

[13] S.P. Lin and R.D. Reitz. Drop and spray formation from a liquid jet. *Annu. Rev. Fluid Mech.*, 30(1):85–105, 1998.

[14] M. Gorokhovski and M. Herrmann. Modeling Primary Atomization. *Annu. Rev. Fluid Mech.*, 2008.

[15] R. Scardovelli and S. Zaleski. Direct numerical simulation of free-surface and interfacial flow. *Annu. Rev. Fluid Mech.*, 31(1):567–603, 1999.

[16] D. Enright, R. Fedkiw, J. Ferziger, and I. Mitchell. A Hybrid Particle Level Set Method for Improved Interface Capturing. *J. Comp. Phys.*, 183(1):83–116, 2002.

[17] S. E. Hieber and P. Koumoutsakos. A Lagrangian particle level set method. *J. Comp. Phys.*, 210(1):342–367, November 2005.

[18] S.O. Unverdi and G. Tryggvason. A front-tracking method for viscous, incompressible, multi-fluid flows. *J. Comput. Phys.*, 100(1):25–37, May 1992.

[19] G. Tryggvason, B. Bunner, A. Esmaeeli, D. Juric, N. Al-Rawahi, W. Tauber, J. Han, S. Nas, and Y.J. Jan. A front-tracking method for the computations of multiphase flow. *J. Comput. Phys.*, 169(2):708–759, May 2001.

[20] S. Osher and J.A. Sethian. Fronts Propagating with Curvature-Dependent Speed: Algorithms Based on Hamilton-Jacobi Formulations. *J. Comp. Phys.*, 79(1):12–49, 1988.

[21] M. Sussman, P. Smereka, and S. Osher. A Level Set Approach for Computing Solutions to Incompressible Two-phase Flow. *Phys. Fluids A*, 114(1):146–159, 1994.

[22] D. Adalsteinsson and J.A. Sethian. A fast level set method for propagating interfaces. *J. Comput. Phys.*, 118(2):269–227, 1994.

[23] J.A. Sethian. *Level set methods and fast marching methods: evolving interfaces in computational geometry, fluid mechanics, computer vision, and materials science*, volume 3. Cambridge university press, 1999.

[24] S. Osher and R. Fedkiw. *Level set methods and dynamic implicit surfaces*, volume 153. Springer, 2003.

[25] C.W. Hirt and B.D. Nichols. Volume of fluid (VOF) method for the dynamics of free boundaries. *J. Comp. Phys.*, 39(1):201–225, 1981.

[26] W.J. Rider and D.B. Kothe. Reconstructing volume tracking. *J. Comput. Phys.*, 141(2):112–152, 1998.

[27] J.E. Pilliod Jr. and E.G. Puckett. Second-order accurate volume-of-fluid algorithms for tracking material interfaces. *J. Comput. Phys.*, 199(2):465–502, September 2004.

[28] E. De Villiers, AD Gosman, and HG Weller. Large Eddy Simulation of Primary Diesel Spray Atomization. *SAE Technical Paper*, 01(0100), 2004.

[29] G.M. Bianchi, P. Pelloni, S. Toninel, R. Scardovelli, A. Leboissetier, and S. Zaleski. Improving the Knowledge of High-Speed Liquid Jets Atomization By Using Quasi-Direct 3D Simulation. *SAE Technical Paper*, 24(089), 2005.

[30] G.M. Bianchi, F. Minelli, R. Scardovelli, and S. Zaleski. 3D Large Scale Simulation of the High-Speed Liquid Jet Atomization. *SAE Technical Paper*, 01(0244), 2007.

[31] J. Shinjo and A. Umemura. Simulation of Liquid Jet Primary Breakup: Dynamics of Ligament and Droplet Formation. *Int. J. Multiphase Flow*, 36(7):513–532, 2010.

[32] M. Sussman and E.G. Puckett. A Coupled Level Set and Volume-of-Fluid Method for Computing 3D and Axisymmetric Incompressible Two-Phase Flows. *J. Comp. Phys.*, 162(2):301–337, 2000.

[33] G. Russo and P. Smereka. A remark on computing distance functions. *J. Comput. Phys.*, 163(1):51–67, September 2000.

[34] T. Menard, S. Tanguy, and A. Berlemont. Coupling Level Set/VOF/Ghost Fluid Methods: Validation and Application to 3D Simulation of the Primary Break-up of a Liquid Jet. *Int. J. Multiphase Flow*, 33(5):510–524, 2007.

[35] M. Herrmann. A Balanced Force Refined Level Set Grid Method for Two-Phase Flows on Unstructured Flow Solver Grids. *J. Comp. Phys.*, 227(4):2674–2706, 2008.

[36] M Herrmann. The influence of density ratio on the primary atomization of a turbulent liquid jet in crossflow. *Proceedings of the Combustion Institute*, 33(2):2079–2088, 2011.

[37] E. Olsson and G. Kreiss. A Conservative Level Set Method for Two Phase Flow. *J. Comp. Phys.*, 210(1):225–246, 2005.

[38] E. Olsson, G. Kreiss, and S. Zahedi. A Conservative Level Set Method for Two Phase Flow II. *J. Comp. Phys.*, 225(1):785–807, 2007.

[39] O. Desjardins, V. Moureau, and H. Pitsch. An Accurate Conservative Level Set/Ghost Fluid Method for Simulating Turbulent Atomization. *J. Comp. Phys.*, 227(18):8395–8416, 2008.

[40] Z. Wang, J. Yang, B. Koo, and F. Stern. A coupled level set and volume-of-fluid method for sharp interface simulation of plunging breaking waves. *Int. J. Multiphase Flow*, 35(3):227–246, March 2009.

[41] S. S. Deshpande and M. F. Trujillo. Distinguishing features of shallow angle plunging jets. *Phys. Fluids*, 25(8):082103, 2013.

[42] P. Sagaut. *Large-Eddy Simulations for Incompressible Flows: An Introduction.* Scientific Computation. Springer, Berlin, 2nd edition, 2001.

[43] E. Labourasse, D. Lacanette, A. Toutant, P. Lubin, S. Vincent, O. Lebaigue, J. Caltagirone, and P. Sagaut. Towards large eddy simulation of isothermal two-phase flows: Governing equations and a priori tests. *Int. J. Multiphase Flow*, 33(1):1–39, 2007.

[44] J. Chesnel, J. Reveillon, F.X. Demoulin, and T. Menard. Subgrid Analysis of Liquid Jet Atomization. *Atomization Spray*, 21(1):41–67, 2011.

[45] P. Sagaut. *Large Eddy Simulation for Incompressible Flows : an Introduction.* Berlin,Springer, 2005.

[46] V. Srinivasan, A.J. Salazar, and K. Saito. Numerical Investigation on the Disintegration of Round Turbulent Liquid Jets Using LES/VOF Techniques. *Atomization Spray*, 18(7):571–618, 2008.

[47] M. Herrmann and M. Gorokhovski. An Outline of an LES Subgrid Model for Liquid/Gas Phase Interface Dynamics. *Proceedings of the 2008 CTR Summer Program,Center for Turbulence Research, Stanford University,CA*, pages 171–181, 2008.

[48] E. O'Brien. The Probability Density Function (PDF) Approach to Reacting Turbulent Flows. *Turbulent Reacting Flows*, pages 185–218, 1980.

[49] S.B. Pope. PDF Methods for Turbulent Reactive Flows. *Prog. Energy Combust. Sci.*, 11(2):119–192, 1985.

[50] P. Givi. Model-free Simulations of Turbulent Reactive Flows. *Prog. Energy Combust. Sci.*, 15(1):1–107, 1989.

[51] S. B. Pope. *Turbulent Flows.* Cambridge University Press, Cambridge, UK, 2000.

[52] S.B. Pope. Computations of Turbulent Combustion: Progress and Challenges. *23rd Symposium on Combustion*, 23(1):591–612, 1991.

[53] F. Gao and E.E. O'Brien. A LargeEddy Simulation Scheme for Turbulent Reacting Flows. *Phys. Fluids A*, 5(6):1282–1284, 1993.

[54] S.C. Garrick. Large eddy simulations of a turbulent reacting mixing layer. In *AIAA, Aerospace Sciences Meeting and Exhibit, 33 rd, Reno, NV*, 1995.

[55] P.J. Colucci, F.A. Jaberi, P. Givi, and S.B. Pope. Filtered Density Function for Large Eddy Simulation of Turbulent Reacting Flows. *Phys. Fluids*, 10:499, 1998.

[56] P. Givi and M.R. Sheikhi. Filtered Density Function for Subgrid Scale Modeling of Turbulent Combustion. *AIAA Journal*, 44(1):16–23, 2009.

[57] J.J. Monaghan and A. Kocharyan. Sph simulation of multi-phase flow. *Computer Physics Communications*, 87(1):225–235, 1995.

[58] J. P. Morris. Simulating surface tension with smoothed particle hydrodynamics. *Int. J. Numer. Meth. Fl.*, 33(3):333–353, 2000.

[59] J. Liu, S. Koshizuka, and Y. Oka. A Hybrid Particle-mesh Method for Viscous, Incompressible, Multiphase Flows. *J. Comp. Phys.*, pages 65–93, 2005.

[60] N. Nishio, K. Yamana, Y. Yamaguchi, T. Inaba, K. Kuroda, T. Nakajima, K. Ohno, and H. Fujimura. Large-scale SPH simulations of droplet impact onto a liquid surface up to the consequent formation of Worthington jet. *Int. J. Numer. Meth. Fl.*, 63(12):1435–1447, 2010.

[61] F. V. Sirotkin and J. J. Yoh. A new particle method for simulating breakup of liquid jets. *J. Comp. Phys.*, 231(4):1650–1674, February 2012.

[62] D. Peng, B. Merriman, S. Osher, H. Zhao, and M. Kang. A PDE-based fast local level set method. *J. Comput. Phys.*, 155(2):410–438, 1999.

[63] C. A. Kennedy and M. H. Carpenter. Several new numerical methods for compressible shear-layer simulations. *Appl. Num. Math.*, 14:397–433, 1994.

[64] J. Larocque, S. Vincent, D. Lacanette, P. Lubin, and J-P. Caltagirone. Parametric study of les subgrid terms in a turbulent phase separation flow. *Int. J. Heat and Fluid Flow*, 31:535–544, 2010.

[65] M. B. Liu and G. R. Liu. Smoothed Particle Hydrodynamics (SPH): an Overview and Recent Developments. *Arch. Comput. Methods Engrg.*, 17(1):25–76, 2010.

[66] M. B. Liu, W. P. Xie, and G. R. Liu. Modeling incompressible flows using a finite particle method. *Appl. Math. Model.*, 29(12):1252–1270, 2005.

[67] J. K. Chen and J. E. Beraun. A Generalized Smoothed Particle Hydrodynamics Method for Nonlinear Dynamic Problems. *Comput. Methods in Appl. Mech. Eng.*, 190(1-2):225–239, 2000.

[68] S. T. Zalesak. Fully multidimensional flux-corrected transport algorithms for fluids. *J. Comp. Phys.*, 31(3):335–362, 1979.

[69] S. C. Garrick, F. A. Jaberi, and P. Givi. Large eddy simulation of scalar transport in a turbulent jet flow. In D. Knight and L. Sakell, editors, *Recent Advances in DNS and LES*, volume 54 of *Fluid Mechanics and its Applications*, pages 155–166. Kluwer Academic Publishers, The Netherlands, 1999.

[70] P. Givi. Filtered density function for subgrid scale modeling of turbulent combustion. *AIAA J.*, 44(1):16–23, January 2006.

[71] J.U. Brackbill, D.B. Kothe, and C. Zemach. A continuum method for modeling surface tension. *J. Comp. Phys.*, 100(2):335–354, 1992.

[72] C. E. Rhoades. A fast algorithm for calculating particle interactions in smooth particle hydrodynamic simulations. *Comput. Phys. Commun.*, 70(3):478–482, 1992.

Appendix A

Numerical schemes for reinitialization

When Level Set (LS) ϕ is solved from the convection equation, the value of LS will deviate from the definition of a LS function. For example, at some instant of time> 0, a point with ϕ equal to 2cm is actually 3cm away from the interface. Such deviation is caused by the physical foundation based on which LS equation was established, which is, a fluid element which is initially at the interface will remain on interface as time goes on. Thus, the LS equation is accurately true for the points on the interface, where the ϕ equals to zero, but not necessarily true for ϕ which equals to other value, because we cannot say a point which is x cm away from interface will remain x cm away from interface as time goes on.

Such deviation can affect solving momentum equation which has the interface curvature term in it, thus must be corrected. This makes the reinitialization steps necessary. There are several reinitialization techniques. A straightforward way is to find the location of interface where ϕ equal to zero, and then re-calculate the closest distance to the interface for all the grid points. Based on this concept, there are also some improved algorithms which do not loop over all grid points but only do this for grid points near the interfaces (see Sussman 2000 for example). A more popular way is to avoid explicitly finding the interface and instead solving a PDE, which solves the ϕ field until it converges to a steady state that meet our requirements. This note describes the second

PDE method, the details can be found in Peng 1999 and Sussman 1994.

A.1 Formulation

$$\frac{\partial \phi}{\partial \tau} = S(\phi)(1 - |\nabla \phi|) \tag{A.1}$$

$$\phi(\vec{x}, 0) = \phi_0(\vec{x}) \tag{A.2}$$

Where $S(\phi)$ is the sign function, and defined as

$$S_\epsilon = \frac{\phi_0}{\sqrt{\phi_0^2 + \epsilon^2}} \tag{A.3}$$

The initial condition is that initial ϕ equals to the uncorrected ϕ field. If solving the above PDE to steady state, can see that regions where ϕ=0 will remain 0. For other non zero regions, ϕ will converge to the actual distance which satisfies $|\nabla \phi| = 1$.

Later, people have made some improvements to the original equation. For example, people find it would be better if substitute ϕ_0 with ϕ in S expression. Also, Peng et al find a better way to approximate ϵ in S, which is:

$$\epsilon^2 = |\nabla_i \phi|^2 \Delta x_i^2 \tag{A.4}$$

It's reported that it only needs typically one or two iteration to meet convergence criterion.

A.2 2D discretization

There are two major ways to solve the reinitialization PDE. Godnov's scheme is introduced here, which is widely used in solving this kind of PDE. For 2D its basic form is described as:

$$a = (\phi_{i,j} - \phi_{i-1,j})/\Delta x \tag{A.5}$$

$$b = (\phi_{i+1,j} - \phi_{i,j})/\Delta x \tag{A.6}$$

$$c = (\phi_{i,j} - \phi_{i,j-1})/\Delta y \tag{A.7}$$

$$d = (\phi_{i,j+1} - \phi_{i,j})/\Delta y \tag{A.8}$$

and

$$\begin{aligned}\phi_{i,j}^{n+1} = \phi_{i,j}^{n} &- \Delta\tau S_{i,j}^{+}(\sqrt{max[(a^{+})^2,(b-)^2] + max[(c+)^2,(d-)^2]} - 1) \\ &- \Delta\tau S_{i,j}^{-}(\sqrt{max[(a^{-})^2,(b+)^2] + max[(c-)^2,(d+)^2]} - 1)\end{aligned} \tag{A.9}$$

(Notice there is a mistake in equation(40) in Peng's paper). The plus and minus sign means the postive or negative part. The above equation comes from Sussman 1994. As described in Peng's paper, for further improvements with regard to the above discretizations, the time intergration can use higher order scheme like TVD-type Runge-Kutta, and the one-sided difference for a,b,c,d can be replaced by ENO or WENO scheme.

A.3 3D discretization

The extension to 3D case of the discretization method is as follows:

$$\begin{aligned}\phi_{i,j,k}^{n+1} = \phi_{i,j,k}^{n} &- \Delta\tau S_{i,j,k}^{+}(\sqrt{max[(a^{+})^2,(b^{-})^2] + max[(c^{+})^2,(d^{-})^2] + max[(e^{+})^2,(f^{-})^2]} - 1) \\ &- \Delta\tau S_{i,j,k}^{-}(\sqrt{max[(a^{-})^2,(b^{+})^2] + max[(c^{-})^2,(d^{+})^2] + max[(e^{-})^2,(f^{+})^2]} - 1)\end{aligned} \tag{A.10}$$

$$a = (\phi_{i,j,k} - \phi_{i-1,j,k})/\Delta x \tag{A.11}$$

$$b = (\phi_{i+1,j,k} - \phi_{i,j,k})/\Delta x \tag{A.12}$$

$$c = (\phi_{i,j,k} - \phi_{i,j-1,k})/\Delta y \tag{A.13}$$

$$d = (\phi_{i,j+1,k} - \phi_{i,j,k})/\Delta y \tag{A.14}$$

$$e = (\phi_{i,j,k} - \phi_{i,j,k-1})/\Delta z \tag{A.15}$$

$$f = (\phi_{i,j,k+1} - \phi_{i,j,k})/\Delta z \tag{A.16}$$

$$S_{i,j,k} = \frac{\phi_{i,j,k}}{\sqrt{\phi_{i,j,k}^2 + \Delta x^2}} \tag{A.17}$$

The plus and minus signs mean the positive or negative part(see part 3). Here Δx is used as an expression of ϵ (for uniform grid) in $S_{i,j,k}$, according to Sussman 1994. Such a choice is simple and effective as long as the initial ϕ field is not deviated too far away from the correct value.